Title

Biological and Biologically Inspired Functional Nanostructures: Insights into Structural, Optical, Thermal, and Sensing Applications

Journal

Advanced Materials, 37(51)

ISSN

0935-9648

Authors

Sung, Chao Hsuan

Hao, Taige

Fang, Herry

et al.

Publication Date

2025-12-01

DOI

10.1002/adma.202509281

Peer reviewed

ADVANCED MATERIALS
www.advmat.de

Biological and Biologically Inspired Functional Nanostructures: Insights into Structural, Optical, Thermal, and Sensing Applications

*Chao Hsuan (Joseph) Sung, Taige Hao, Herry Fang, Andrew Tran Nguyen, Valentina Perricone, Haitao Yu, Wei Huang, Ezra Sarmiento, Adrian Francisco Duran Ornelas, Derek Lublin, Ric Wehling, Sanaz Farajollahi, Atsushi Arakaki, Dhriti Nepal, Nathan Patrick Lord, and David Kisailus**

Biological materials developed over millennia consist of simple biogenic materials, yet exhibit exceptional functional properties. Leveraging design features from these structures with engineered nanomaterial components can lead to bio-inspired structures that demonstrate superior performance over traditional engineering materials. We describe nanoscale based architectures in biological systems, their role in enhancement of structural, optical, thermal and sensing properties, and their subsequent translation to bio-inspired structures. In structurally robust biological materials, we highlight nanoscale design features that enhance strength and stiffness, while retaining toughness. In optically active biological materials, we show how periodic nanostructures manipulate electromagnetic waves resulting in structural coloration as well as antireflective and camouflaging properties. Thermally regulating biological materials utilize nanopores and other nanostructural features to statically or dynamically control temperature. In addition, biological materials that are used in sensing utilize various nanostructures that enhance sensitivity by decreasing activation thresholds for signal transduction. We discuss challenges and opportunities including understanding control mechanisms in the formation of biological materials and leveraging advancements in self-assembly with new additive manufacturing techniques. The continued evaluation of organisms, including those that exhibit multifunctionality, provides not only new design features and pathways, but significant prospects for innovation in this ever-emerging field.

1. Introduction

As we enter the second quarter of the 21st century, the ever-increasing global population has led to increasing societal and environmental issues, placing pressure across all industries (e.g., agriculture, mining, manufacturing, construction, transportation, healthcare, information technology).[1–6] These issues necessitate the development of high-performance advanced nanoscale materials, offering an exciting opportunity for the scientific and engineering communities.

The global nanomaterials market accounted for USD 10.34 billion in 2020 and is projected to grow to USD 38.17 billion by 2029.[7] Currently, the healthcare sector captures the largest market share of nanotechnology requiring materials for nano diagnostics, nano-surgical robots, cell repair applications, nano-biosensors, imaging, and targeted drug delivery.[8–10] At the same time, a significant fraction of the market is related to the need for nanomaterials in applications related to

C. H. (Joseph) Sung, H. Fang, V. Perricone, H. Yu, E. Sarmiento, A. F. D. Ornelas, D. Kisailus
Department of Materials Science and Engineering
University of California
Irvine, Irvine, CA 92697, USA
E-mail: david.k@uci.edu

The ORCID identification number(s) for the author(s) of this article can be found under https://doi.org/10.1002/adma.202509281

DOI: 10.1002/adma.202509281

T. Hao, A. T. Nguyen, D. Lublin, D. Kisailus
Materials and Manufacturing Technologies Program
College of Engineering
University of California
Irvine, Irvine, CA 92697, USA

R. Wehling, N. P. Lord
Air Force Research Laboratory/RW
Eglin Air Force Base, FL 32542, USA

S. Farajollahi, D. Nepal
Air Force Research Laboratory/RX
Wright-Patterson Air Force Base, OH 45433, USA

A. Arakaki
Institute of Engineering
Division of Biotechnology and Life Science
Tokyo University of Agriculture and Technology
Tokyo 184-8588, Japan

energy conversion (e.g., solar, fuel cell, nuclear), storage (e.g., batteries), and consumption (e.g., light-weight structures).

Currently, the synthesis processes of conventional nanomaterials often require complex chemistry, harsh conditions (extreme pH, temperature, vacuum), and significant energy expenditure, all of which have negative environmental impacts.[11] Many of the synthesis processes for these nanoscaled materials lack the ability to control interfaces or achieve the multiscale (nano-, micro-, and macro-) architectures needed for high performance and system integration.[12–16]

Over hundreds of millions of years, organisms have evolved by adapting against a broad range of ecological pressures and predation by developing robust structures for selected functions (e.g., mechanical, thermal, optical, and sensing). These biological structures, found in both animal and plant tissues, are formed from a limited selection of starting materials, and demonstrate performance greater than, or similar to, many traditional engineering materials.[17–19] The remarkable properties exhibited in these structures are related to their multiscale architectures, formed by the controlled synthesis and hierarchical assembly of nano- to micro-scaled building blocks.[20–42] Specifically, biological macromolecules, often structural polysaccharides and functional proteins, are spatially and temporally arranged to form scaffolds that dictate the multiscale architectures that are filled with either an organic (e.g., protein) or mineral matrix (the latter of which is afforded by the orchestration of mineral transport, nucleation, and growth).[37,43–47] In fact, the biological macromolecules are not only used to precisely guide the architectural frameworks, but also enable transport and deposition of minerals with precise control.[34,36,48–52]

Leveraging the synthesis-structure and structure-function relationships observed in biological systems, researchers are now developing bio-inspired nanostructures as a promising strategy to address many of the aforementioned technological challenges.[53] An advantage of bio-inspired materials is that thousands of blueprints from biological systems can be utilized, but with a significantly broader selection of material chemistries and phases that demonstrate performance under conditions far beyond (e.g., temperature, mechanical stresses, radiation intensity, etc.) those observed in nature. In addition, there is an abundance of biological systems that demonstrate multifunctionality that, if utilized, can lead to transformational developments in many technological sectors. Finally, the pathways through which biological systems control size, shape, phase, and crystallographic orientation of biogenic minerals continue to be investigated, presenting opportunities not only for controlled nanocrystal growth that yields higher performance (vs conventional methods) but also toward the development of efficient and accurate manufacturing processes that are less energy intensive and potentially less environmentally hazardous. In addition, these processes provide control in biological systems. Thus, there are significant opportunities to leverage knowledge from both biological designs and the orchestrated synthesis pathways through which these elegant structures are formed.

While there are existing reviews that discuss bio-inspired functional materials (and we advise readers to refer to them for a more holistic understanding of this field),[3,4,39,54–57] few have focused specifically on the role of nanoscale structures that afford function in these systems. Here, we provide an overview of nanostructured biological materials with structural, optical, thermal, and sensing functions, their bio-inspired derivatives, as well as insights into the new opportunities and challenges in this evolving field. These specific functions were selected as they are critical to enable adaptations to changes in the environment and protection against predation, ensuring the survival of organisms. Structural nanostructures serve as platforms for withstanding direct physical interactions, while both optical and sensing nanostructures enable tracking food, avoiding predation, finding prey, etc., and thermal nanostructures allow organisms to adapt to temperature fluctuations, especially those in extreme habitats. We refer readers interested in other functional materials inspired by biology to the following reviews on adhesives,[58–60] self-healing,[61,62] energy storage and transfer,[63–65] catalysis,[66,67] transport and delivery,[68–71] and information storage materials.[72] Readers interested in the broader field of bio-inspiration can find comprehensive reviews on bio-inspired interfaces,[73–77] nanomaterials,[78,79] modeling,[80,81] and synthesis (**Figure 1**).[82,83]

2. Structural Materials

Light-weight, energy-efficient, and high-performance structural materials that exhibit strength and toughness are highly desirable for many engineering applications. Creating materials for airframes, spacecraft, satellites, building structures, and human protection while also providing multifunctionality (such as thermal or radiation resistance) is a challenging task. This challenge arises from the fact that introducing constituents intended to enhance one function may detrimentally affect another. Nature has evolved efficient strategies to address this orthogonality, exemplified in the biological tissues and biomineralization processes of numerous animal and plant species that demonstrate precise control over the material architecture across multiple dimensionalities. Such strategies can be used for constructing multi-scale materials that often exhibit exceptional mechanical properties with additional functionalities, such as wear or thermal resistance, self-healing, sensing, and responsiveness.

2.1. Biological System Designs

Biological systems have developed structurally robust materials such as bones, shells, teeth, etc.[98–103] These structures, modified over millions of years in response to both biotic and abiotic stresses, integrate organic material components, often with nano and microscale minerals, into multiscale architectures to maximize fitness.

Many of the constituent mineral (ceramic) materials (e.g., silicon dioxide, calcium carbonate, calcium phosphate, and iron oxide) of these structures are inherently strong but brittle, whereas

W. Huang
State Key Laboratory of Materials Processing and Die and Mould Technology
School of Materials Science and Engineering
Huazhong University of Science and Technology
Wuhan 430074, China

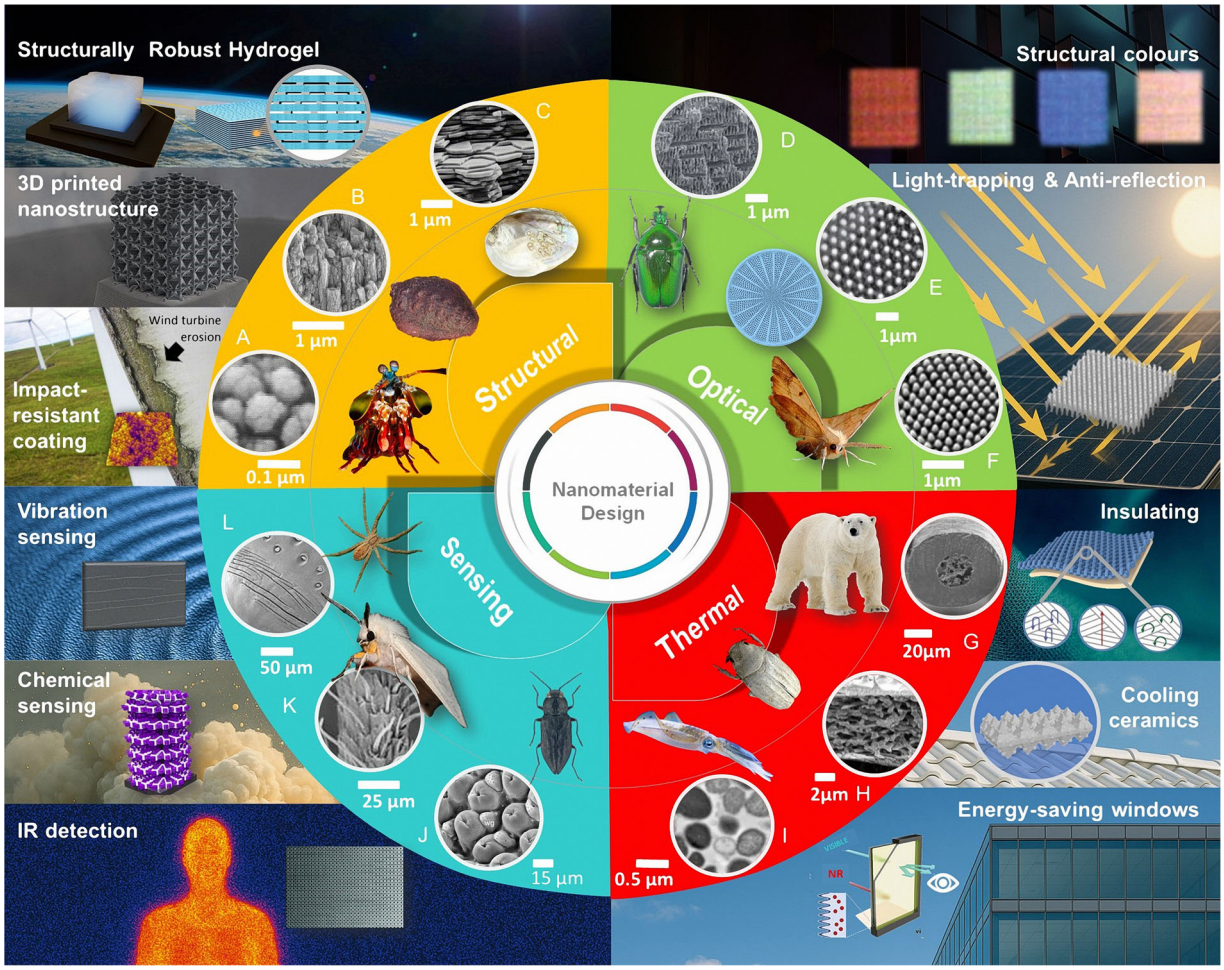

Figure 1. Overview of Biological and Bio-inspired Nanomaterial Design. Summary of key biological models and their translation into functional nanomaterials across four domains: Structural, Optical, Thermal, and Sensing material design. Structural Materials: A) Nanoparticulate impact-resistant architecture of the mantis shrimp, *Odontodactylus scyllarus*, dactyl club, inspiring durable protective coatings for multiple applications, including wind turbines. Reproduced with permission.[84] Copyright 2020, Springer Nature. B) High-performance radular nanofibers of chitons, informing bio-inspired 3D printed nanostructures. Reproduced with permission.[16,17] Copyright 2020, Springer Nature. Copyright 2017, Wiley. C) Brick-and-mortar nacre architectures, replicated in robust and stretchable hydrogels for space applications. Reproduced with permission.[85,86] Copyright 2024, Wiley. Copyright 2005, Elsevier. Optical Materials: D) Structural coloration in *Trigonophorus rothschildi varians*, guiding the development of vivid, pigment-free photonic materials. Reproduced with permission.[87] Copyright 2004, Royal Society. E) Nanoporous silica shells of diatoms, enabling light-trapping functionalities for photonic and energy applications. Reproduced with permission.[88] Copyright 2015, Springer Nature. F) Anti-reflective corneal nanostructures of moth eyes, adapted for high-efficiency solar panel coatings. Reproduced with permission.[89] Copyright 2018, Springer Nature. Thermal Materials: G) Thermoinsulating properties of polar bear fur, inspiring advanced textile insulation. Reproduced with permission.[90] Copyright 2019, Elsevier B.V. H) Ultrabright scattering scales of Cyphochilus beetles, leading to heat-reflective ceramic coatings and tiles. Reproduced with permission.[91] Copyright 2023, AAAS. I) Cephalopod chromatophores with dynamic thermal modulation, informing sustainable buildings (e.g., energy-efficient mechano-thermochromic windows.). Reproduced with permission.[92] Copyright 2020, Elsevier B.V. Sensing Materials: J) Infrared sensory organs of *Melanophila acuminata*, serving as models for IR detection devices. Reproduced with permission.[93] Copyright 2015, MDPI. K) Chemosensory antennae of Bombyx mori, inspiring chemical sensing platforms. Reproduced with permissions.[94,95] Copyright 2014, Frontiers. Copyright 2022, Elsevier. L) Mechanosensory nano-slits of *Cupiennius salei*, guiding the development of vibration-sensitive sensors. Reproduced with permissions.[96,97] Copyright 2007, The Royal Society. Copyright 2014, Springer Nature. All other images used in this figure are licensed under public use licensess. (See Supplemental).

the organic components (e.g., proteins and polysaccharides) are weak but tough.[104–107] The resultant biological composite structures are formed via an orchestrated synthesis and assembly across multiple dimensionalities (0D, 1D, 2D), resulting in larger complex 3D structures with optimized strength and toughness.[35] Furthermore, structural organics functionalized with charged proteins guide nucleation and growth of the mineral components, yielding morphologically controlled nanoscale building blocks, which are significantly stronger and tougher than bulk ceramics. The resultant increased strength and toughness of these nanoscale composites are afforded primarily via a reduction in flaw probability (i.e., Hall-Petch effect), as well as an increased number of organic-mineral interfaces per length—leading to additional crack deflection.[108]

Specifically, these interfaces that exist between nanoscale minerals and the organic scaffolds enable strengthening,

stiffening, and toughening through crack deflection, delamination, fiber bridging, and particle breakage.[109–112] The ability for crack deflection to occur at interfaces in composite materials is highly dependent on the modulus mismatch between material components.[113,114] Thus, the nanoscale building blocks in biological composite materials significantly increase the number of these dissimilar modulus interfaces (organic–mineral or organic–organic), resulting in a greater number of sites where energy can be absorbed via crack deflection.[115] Based on these observations, multiscale biological structures and their assembly processes provide inspiration for the design of advanced nanostructured materials and novel synthesis processes.

2.1.1. 0D Features

Many of the mechanically robust biological structures that have been described to date[105] involve 1D (nanofiber/nanorod) and 2D (nanoplatelet) features that are integrated into 3D structures. Many of these 1D and 2D structures originate from biomineralization processes that use 0D nanoparticle building blocks.[116] Recently, we uncovered 0D design features embedded within the highly impact-resistant dactyl club of the peacock mantis shrimp, *Odontodactylus scyllarus* (**Figure 2a**).[84] This mantis shrimp can strike and penetrate the hard-shelled armor of crustaceans and mollusks as part of its predatory and ritualized fighting behavior, exerting high-strain-rate impact forces as high as 1500 N.[117,118] The multiregional and hierarchical architecture of the dactyl club works cohesively to dissipate the incoming impact energy and minimize catastrophic failure (Figures 2a–c,k). At the impact surface, a thin (≈70 µm thick) nanocomposite coating comprised of 0D bi-continuous hydroxyapatite (HAP)–organic (chitin and protein) nanoparticles (≈60 nm) surrounded by additional chitin and protein matrix protects the underlying structure (Figures 2d–j). These chitin and protein macromolecules serve as a template for the growth of bi-continuous HAP-organic nanoparticles with multiple nanoscale mineral-mineral and mineral–organic interfaces (Figures 2g–j). The interpenetrating organic (chitin and protein) phase of these bi-continuous HAP-based nanoparticles enables an elastic response under quasi-static loading or strain stiffening during high-strain-rate impacts. Upon impact, these composite nanoparticles localize damage and dissipate impact energy via fracture, amorphization, and generation of dislocations within the mineral phase along low-angle grain boundary interfaces and through rotation and translation within the organic matrix (Figure 2).[84] The unique bi-continuous architecture of the nanoparticle substantially increases the stiffness and strength of the structure compared to traditional composites, which lack integrated phases, thereby improving energy absorption.[84,119]

2.1.2. 1D Features

Beyond 0D architectures, numerous biological materials feature 1D anisotropic structures that play a critical role in enhancing mechanical performance. These anisotropic elements are composed of organic, inorganic, or hybrid components, and often serve as the primary load-bearing frameworks in natural systems. Strong and often stiff biological macromolecules such as cellulose, chitin, collagen, and keratin are the main scaffolding structural components in nature. These macromolecules typically assemble into 1D nanofibers/nanotubules to control the formation of structures like wood, teeth, bone, skin, scales, horns, and hooves.[105,120] The specific arrangement of these macromolecules at the nanoscale translates into the bulk structures we observe, providing tensile strength, stiffness, toughness, and energy dissipation.[35]

As the most abundant biopolymer on Earth, cellulose contributes to many biological structural materials such as plant cell walls, tunicate mantles, and bacterial biofilms.[125,126] The use of cellulose in structural and architected materials throughout human history has garnered significant interest due to its lightweight nature, biocompatibility, and high specific strength.[127] The various types of hydrogen bonding in cellulose (e.g., the hydroxyl groups and oxygen atoms of the D-glucopyranose ring) contribute to its unique physical properties.[128] The most well-known example of this is found in wood, where its mechanical properties are mainly derived from the dense intra- and inter-molecular hydrogen bonds in its cellulosic fibers (**Figures 3a–c**).[129] These hydrogen bonds exist at the interfaces between the individual cellulose fibers and between fiber bundles. Under tensile loading, the hydrogen bonds at these interfaces can break and reform, dissipating energy and toughening the material.[130–132] In addition, the physical entanglement of cellulose fibrils also provides energy dissipation during high-strain-rate impacts.[121,127] Cellulose fibers found in wood undergo significant toughening due to the rotation and reorientation of microfibrils when strained.[130,133] Under the influence of tensile loading, the angles between the fibrils decrease, with cellulose fibrils rotating and reorienting in the direction of the applied tensile force, strengthening the material.[134,135] The nanofibril realignment during the loading process also induces plastic deformation and viscous flow of the lignin matrix, another mechanism of increasing strength and toughness.[130] These properties and mechanisms within cellulose make it a compelling source of inspiration for strong and tough bio-inspired materials and a promising candidate as an alternative to synthetic polymers.

Second to cellulose in abundance, chitin is found as an independent structural element (e.g., in cuticles of arthropods).[36,136,137] Chitin is a polysaccharide often co-assembled with proteins to form anisotropic nanofibrils ranging from 2 to 7 nm in diameter.[138,139] These further assemble into nanofibers (50–250 nm thick) with highly controlled spacing and orientation in higher order structures.[36,139,140] While the ring-like molecular structure of chitin monomers provides rigidity, extensive hydrogen bonding interactions between hydroxyl and acetyl groups on neighboring chitin molecular chains lead to significant toughening. This is observed in non-mineralized structures (e.g., insect cuticles such as beetle elytra) where nanoscale chitin-protein fibrils are assembled into unidirectional micron-sized bundles that are further architected into lamellae. These nanoscale 1D organic components provide significant strength and toughness. Furthermore, the proteins within these bundles can undergo biochemical hardening via catechol oxidation or di-tyrosine cross-linking (tanning and sclerotization), resulting in a graded stiffening of the material that enhances both hardness and toughness.[43,138,141,142]

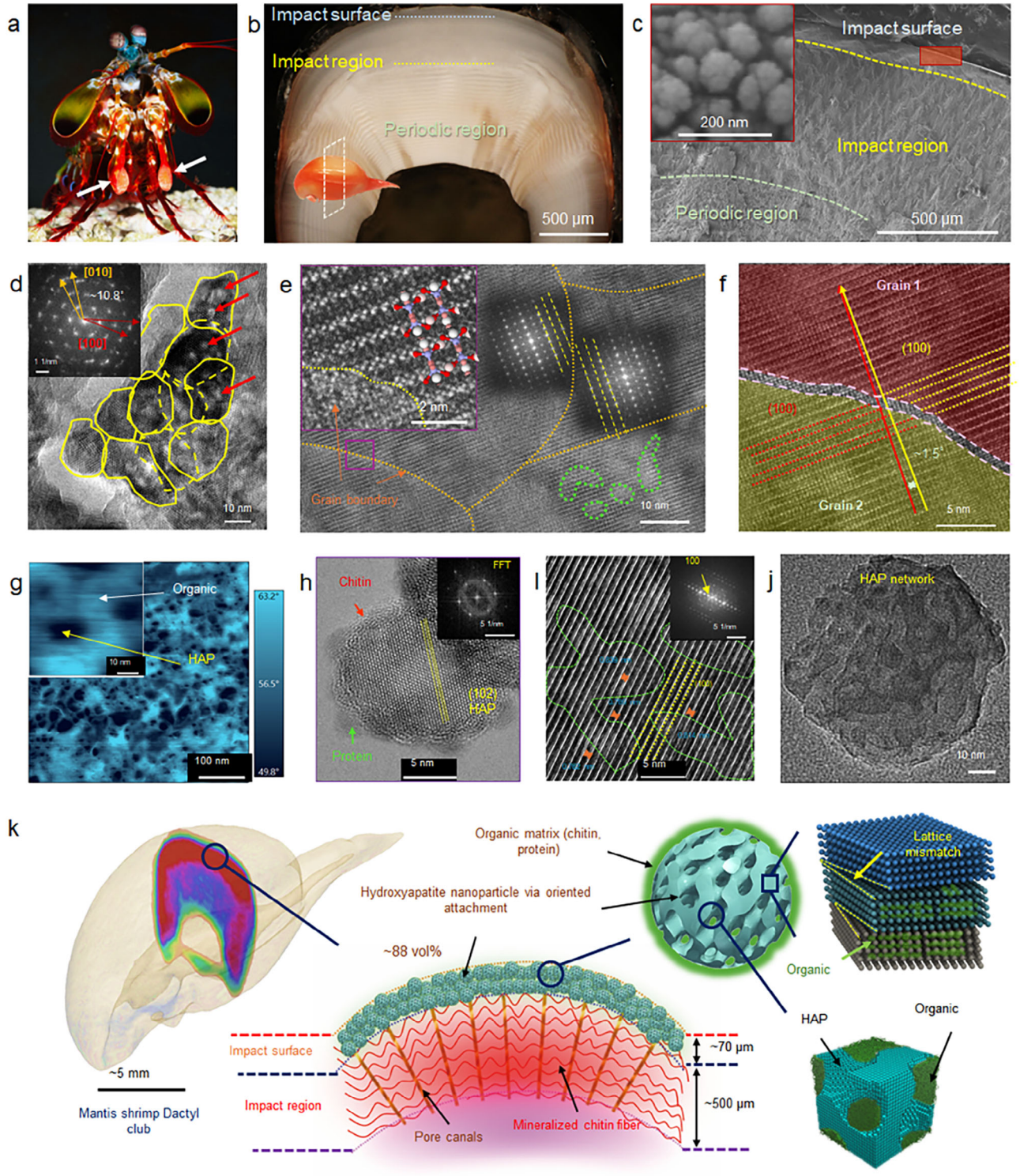

Figure 2. Impact surface and structure of the mantis shrimp dactyl club. a) Photograph of a mantis shrimp and its dactyl club, indicated with white arrows. b) Optical micrograph of the transverse section of an intact dactyl club showing the impact surface, impact region, and periodic region. c) SEM micrograph of a transverse section of an intermolted dactyl club. Inset: nanoparticles ≈60 nm in diameter are found within the impact surface. d) Primary grains were found assembled within a single ≈60 nm secondary particle. The white dots marked with red arrows suggest a second phase. Inset: the arcs in the FFT pattern indicate the misalignment of primary grains. e) Grain boundaries of adjacent grains, indicated by FFT spectroscopy. Inset: HRTEM demonstrating the disordered grain boundary adjacent to the (100) planes of HAP crystals. The second phase found in a is outlined in green. f) Misalignment (≈1.5°) of two adjacent grains. g) AFM phase map of a coronal section of the impact surface showing the network of two different phases. The angle (color scale) refers to the phase change/lag during the AFM tests. The phase change thus reflects changes in mechanical properties. Inset: high-resolution image illustrating the two different phases. h) HRTEM of stained samples showing chitin molecules surrounding a HAP crystal

Beyond non-mineralized structures, these protein–chitin assemblies can also serve as a scaffold for biomineralization (Section 2.1).[36] For example, both gastropods and mollusks utilize acidic proteins that are co-located within chitin-based scaffolds to template nucleation and growth of calcium carbonate (aragonite or calcite) to form 1D rod-like architectures (i.e., cross-lamellar) or 2D plate-like structures (i.e., nacre; see section 2.1.3) that are significantly tougher than geological minerals. These robust structures were designed to resist compressive and bending stresses experienced during predation as well as during impact with intertidal rocks. These multi-scale hierarchical crossed-lamellar structures are assembled from nanoscale domains into 1D aragonitic planks that subsequently align to form lamellae.[143,144] Fourth-order nanotwinned aragonite nanoparticles serve as the base unit for this structure,[145–148] assembling into third-order 1D aragonite planks coated in conchiolin (i.e., chitin + protein) that are 200 nm wide and several microns long.[143,146] As shown in **Figure 4A**, these third-order nanoplanks are bundled to form second-order lamellae, which further assemble in alternating directions at 45° into first-order lamellae.[149] These first-order lamellae are arranged in a 0°–90°–0° stacking sequence to form the various layers of the shell.[143,146,150] While the exact formation process of this complex structure has not yet been elucidated, preliminary work suggests that a combination of liquid-crystal precursors is involved in traditional biomineralization processes (Section 2.1).[151]

Figure 4B shows the greater crack resistance seen in cross-lamellar architected conch shells versus that of its constituent mineral component (geological aragonite). Under compressive loading conditions, alternating lamellae serve to enhance the fracture toughness through energy dissipation and crack deflection along a significant number of interfaces between the multilayered nanoscale lamellae (Figure 4C).[143] Additionally, the fourth-order nanotwinned particles serve to increase fracture toughness by inducing phase transformations that block crack propagation.[148] The path of crack growth can either travel along the length of the 1D aragonite nanoplanks and lamellae or propagate through the layers of lamellae.[146,149,150] When the crack path follows the length of the lamellae, they are redirected at the interfaces of orthogonal lamellae (Figure 4C).[143,146,149] Alternatively, cracks propagating within lamellae will lead to brittle fracture of the 1D aragonite planks. In both cases, significant amounts of energy are dissipated.[149,152] In conjunction with the aforementioned toughening mechanisms, the alternating directionality of lamellae act to bridge gaps in adjacent layers caused by fractures, preventing catastrophic failure.

Another organism that leverages 1D mineralized structures is the chiton, a mollusk with ultrahard teeth that inhabits intertidal rocks along coastal shores worldwide.[17,154] Chitons feed by scraping various types of algae (e.g., crustose and leafy algae) off rocky substrates, necessitating the development of ultrahard teeth to withstand stresses without frequent failure. One species of chiton, *Cryptochiton stelleri*, employs tri-cusped teeth with a core-shell structure consisting of 1D nanorods of magnetite within the shell and phosphosiderite within the core (Figure 3d); these teeth exhibit the greatest hardness and stiffness of any biogenic material, as much as threefold harder than human enamel and nacre.[17] This extreme mechanical performance is attributed to the combination of material components and their nanoscale architecture. These magnetite nanorods are aligned parallel to the long axis of the tooth, affording high tensile and compressive strength along the leading and trailing edges, respectively, of the tooth during rasping.[155–157] Nanoscale surface asperities and mineral bridges between each nanorod help to resist sliding and increase overall toughness.[17,154,155,158]

Interestingly, chitons also demonstrate the ability to produce new teeth every 3–4 days, aiding in their survival,[38,159] while also enabling investigation of the formation mechanisms of these nanoscale structures. Each of these 1D architected nanorods (≈150 nm diameter) is surrounded by a thin veneer of chitin-based fibers associated with charged proteins.[17,38,155] Here, the semi-crystalline nanoscale chitinous fibers are assembled and subsequently decorated by phosphorylated proteins that induce localized nucleation and growth of ferrihydrite nanoparticles via a controlled mesocrystalline assembly of 0D nanostructures,[160] which eventually transform to continuous rods of magnetite (Figures 3e–g). In fact, it was recently discovered that the protein co-assembly was spatially and temporally controlled by transport from the surrounding epithelial tissue into the tooth via nanotubules. This orchestration enables the careful construction of highly crystalline and ordered nanostructures within these highly abrasion-resistant and tough teeth.

While magnetite nanorods provide the robust abrasion resistance of these teeth, other species of chiton, such as *Acanthopleura hirtosa* and *Chiton articulatus*, utilize additional nanoscale iron oxide phases (goethite and lepidocrocite) as well as calcium phosphate phases (hydroxyapatite).[158,159,161] In *Chiton articulatus*, multiple mineral components (i.e., magnetite, goethite, lepidocrocite, and hydroxyapatite) form a stiffness and hardness gradient across the tooth cross-section. This enables the preferential wear of teeth as the softer hydroxyapatite erodes faster than magnetite during rasping, leading to self-sharpening.[159]

Mammals also demonstrate the utility of 1D structures in the form of bones and teeth, which consist of mineral-collagen nanofiber composites. Within each structure, poorly crystalline hydroxyapatite platelets are formed within a 1D collagen fiber scaffold, staggered ≈67 nm apart. Beyond mineralized structures, these 1D collagenous fibers are used in skin, which is critical for providing protection from predatory attacks and transducing stimuli from external environments. For example,

lattice. Proteins are stained as dark spots. Inset: FFT pattern of the chitin-wrapped HAP nanoparticles. Diffraction spots represent HAP crystals and the broad diffuse ring represents the chitin macromolecules. i) HRTEM image shows the organic network within the HAP crystalline network. The green dashed lines indicate areas that have organic phase, as suggested by the expanded d spacings of the lattice. Inset: FFT pattern. j) HRTEM of HAP particles after heat treatment at 800 °C. k) Schematic of the dactyl club highlighting the impact surface and illustrating its location and hierarchical nature. From left to right: drawing of the dactyl club, with the transverse cutaway highlighted in color; impact surface and impact region from the transverse section; HAP nanoparticles embedded in an organic matrix on the impact surface; bi-continuous network of the HAP nanoparticles within an organic phase (bottom); oriented attachment of HAP nanocrystals, in which the lattice mismatch and organics embedded within the HAP crystal lattice are illustrated (top). Adapted with permission.[84] Copyright 2020, Springer Nature.

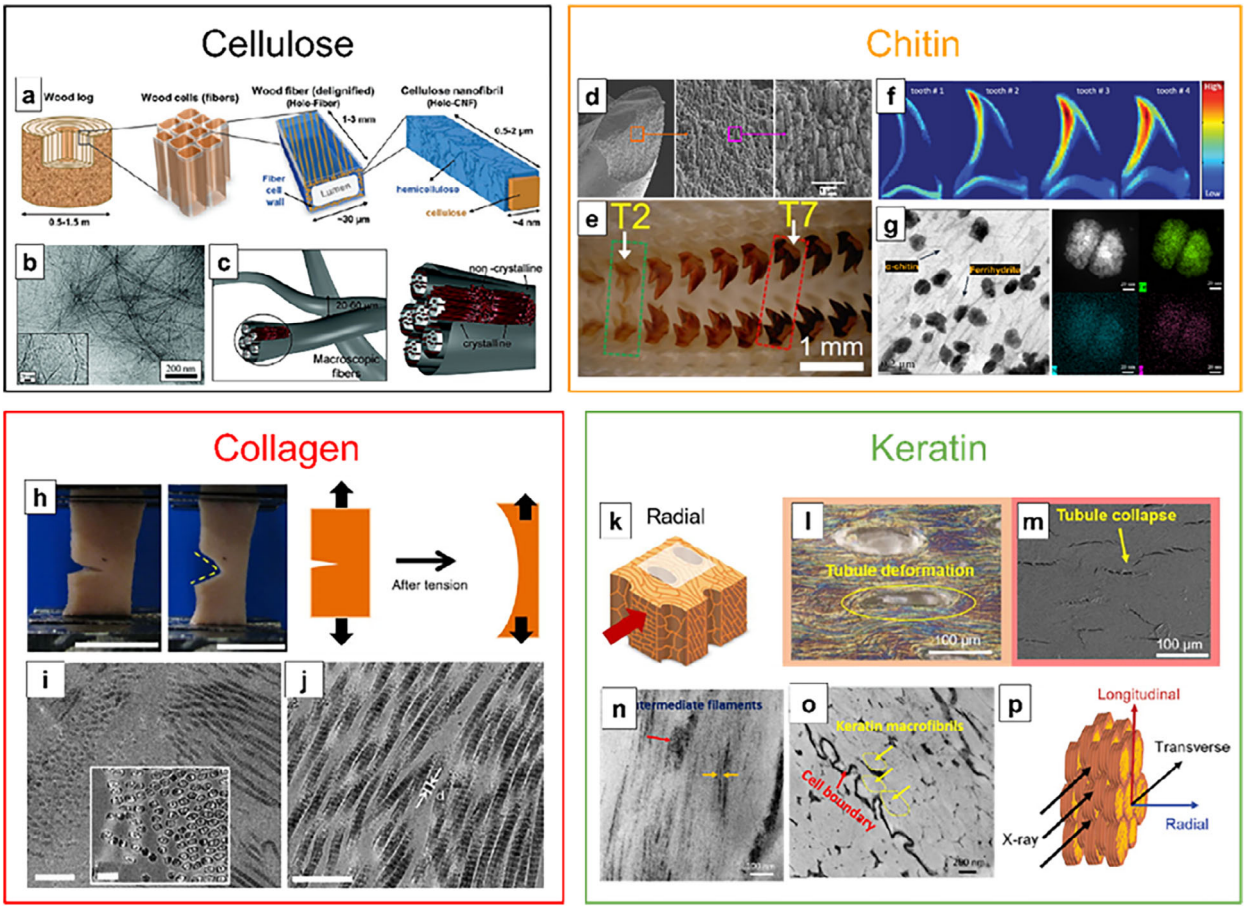

Figure 3. Representative biological macromolecules in structural biological materials. a–c) Hierarchical structure of wood and cellulose fibers. Crystalline and non-crystalline regions are shown. a) Reproduced with permission.[127] Copyright 2021, Wiley. b,c) Adapted with permission.[121] Copyright 2007, American Chemical Society. d–g) Mineralized iron oxide onto a chitin scaffold. Hierarchical structure of nanorods results in robust mechanical properties. Adapted with permissions.[17,38,160] Copyright 2013, Wiley. Copyright 2010, Elsevier. Copyright 2022, Wiley. h–j) Skin and collagen fibers at the nanoscale. Skins show resistance to crack propagation. Adapted with permission.[122] Copyright 2015, Springer Nature. k–p) Bighorn sheep horns and keratin fibers inside keratinized cells. Crystalline intermediate filaments are indicated. Adapted with permissions.[123,124] Copyright 2017, Elsevier. Copyright 2019, Wiley.

investigation into the mechanical properties of rabbit skin revealed toughening mechanisms, such as rotation, straightening, stretching, sliding, and delamination of individual collagen nanofibrils, which allow for tear resistance and an insensitivity to cracking (Figures 3h–j).[122] Another class of 1D macromolecules, keratins, represents the main component of horns and hooves, contributing significantly to energy absorption under high strain rate impacts.[19,123] At the nanoscale, keratin molecules form crystalline 1D fiber-like intermediate filaments (IFs) within an amorphous matrix (Figures 3k–p). The stretching of these IFs and subsequent breaking of hydrogen bonds inside the fibers were found to be the main sources of energy dissipation in keratin-based tissues when observed with in situ wide-angle X-ray diffraction (WAXD) combined with tensile tests.[124]

2.1.3. 2D Features

Beyond 1D structures, gastropods (as well as bivalves and cephalopods) have also evolved 2D plate-like nanostructures (nacre) to improve the toughness of their shell's inner region to mitigate the crushing forces from predators and impact against intertidal rocks.[162] Nacre is composed of 95 wt.% aragonite and 5 wt% organic biopolymer (chitin and protein) and exhibits 3000 times the toughness of geologic aragonite.[162–165] This exceptional mechanical performance arises from the combination of its organic and mineral components as well as their nanoscale architectures. The 2D aragonite nanoplatelets (200–500 nm thick, which is species dependent) are arranged in a highly ordered interlocking laminated structure. Each layer of 2D tablets is encased in an ultrathin (≈10–40 nm thick) biopolymer matrix, forming a classic "brick-and-mortar" architecture (Figure 4G).[86,163–166] These proteins, associated with the assembled chitin, dictate the nucleation of aragonite while the chitinous scaffold controls the size of the 2D platelets.[167–169] The formation of subsequent layers also creates mineral bridges between nanoplate layers as additional mineral grows through the pores, within the organic matrix, to the next layer.[169,170]

Figures 4G,H show the interlocking aragonitic platelets, which toughen the material through crack deflection due to the

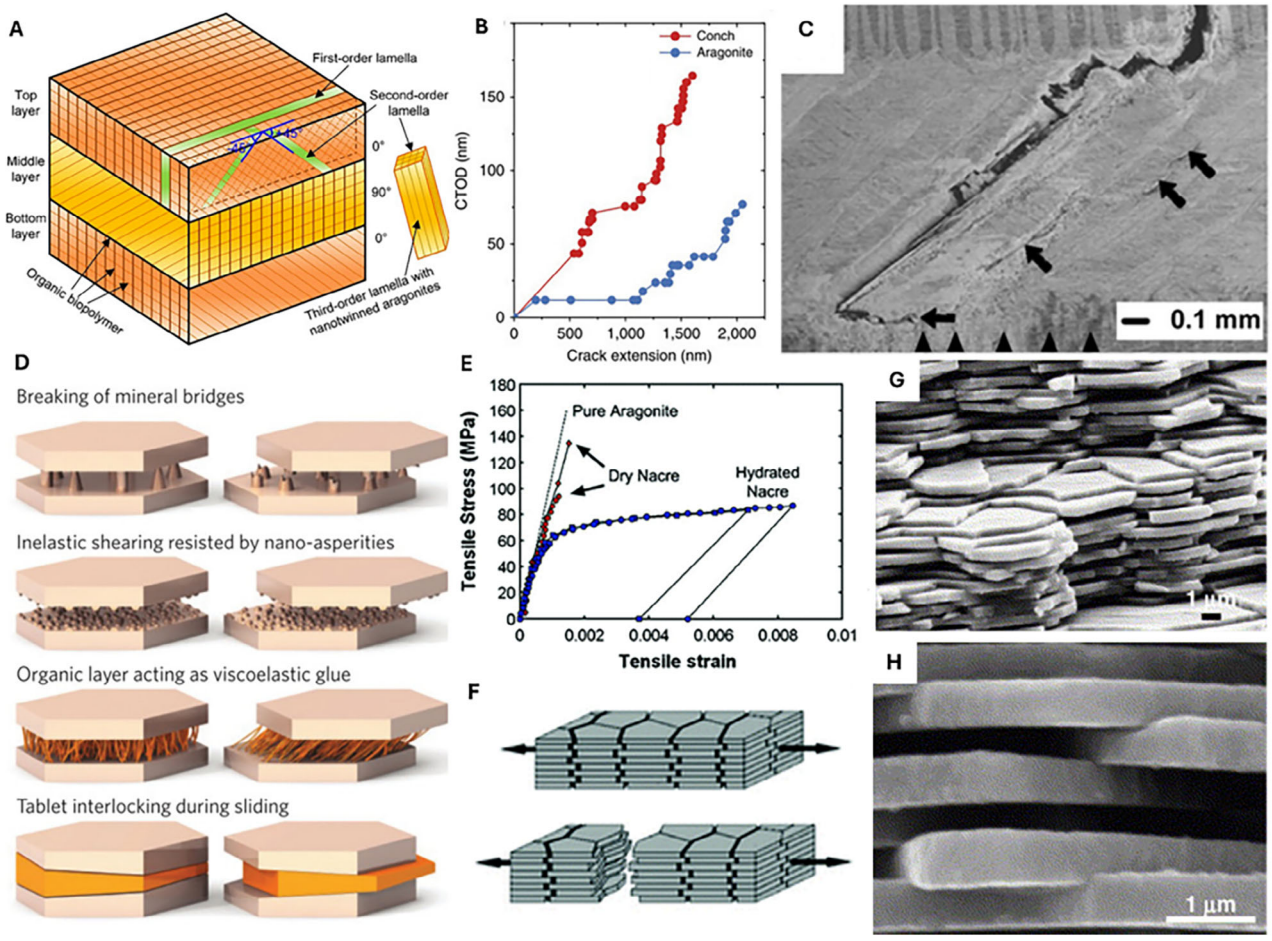

Figure 4. Schematic of A) the hierarchical crossed-lamellar structure observed in the conch shells. Adapted with permission.[144] Copyright 2025, Wiley. B) Plot of the crack tip opening displacement as a function of crack extension in conch and single crystal aragonite. Adapated with permission.[149] Copyright 2016, Springer Nature. C) Crack is shown traveling straight through the "weak" direction and being deflected within the next layer. Adapted with permission.[150] Copyright 2004, Elsevier. D) Schematic of different energy dissipation mechanisms in the platelet sliding process. Adapted with permission.[54] Copyright 2015, Springer Nature. E) Experimental tensile stress-strain curve for nacre and F) schematics associated with deformation modes. Adapted with permission.[154] Copyright 2007, Elsevier. SEM microscopy of nacreous structures exhibiting: G) platelet pullout and H) presence of interlocking between platelets. Adapted with permission.[86] Copyright 2006, Elsevier.

stiffness mismatch between the organic matrix and the aragonite nanoplates (i.e., Dundurs parameter). This mismatch at the many interfaces between these nanoscale platelets dissipates significant energy and prevents crack coalescence that would lead to catastrophic failure.[162] During loading, platelet pullout (Figures 4F,H) is another energy dissipation mechanism that augments nacre's toughness and strength. Furthermore, these interfaces also limit deformation between mineral layers, providing ductility by alleviating high local strain (Figure 4D).[12,54,133] Figure 4E exhibits the importance of the biopolymer layer, which allows nacre to deform more than pure aragonite, and significantly more when the biopolymer is hydrated. The aragonite nanoplatelets are also composed of nanograins that individually undergo rotation and deformation to dissipate energy.[164,171,172] This mobility of these nanograins also contributes to the high fracture toughness of nacre.[86,150,163,166] Additionally, nanoasperities on the surfaces of the nacreous plates (Figure 4D) and the mineral bridges between plates have been proposed as additional interlocking and toughening mechanisms. When sheared, nanoasperities between nacreous plates provide frictional forces during platelet sliding, which creates an additional layer of interlocking. Mineral bridges connecting neighboring aragonite plates are also broken, further toughening the material (Figure 4D).[12,54,133,173,174] These nanoscale mineral bridges are significantly stronger than bulk aragonite[108] while their small diameters afford a high number density on each 2D aragonitic table, leading to significant strengthening and toughening.

2.1.4. 3D Features

Many of the aforementioned 0D and 1D mineral and organic nanostructured features are also used as building blocks in the architected assembly of 3D structures with a unique combination of lightweight, stiffness, strength, and toughness that otherwise would not exist. Over the past decade, there have been significant studies of biological structures that maximize strength, stiffness, toughness, and impact resistance. In a recent review

highlighting multiple multiscaled biological structures in the Animal and Plant kingdoms,[35] it was determined that the helicoidal or Bouligand architecture (**Figure 5**) is a dominant architecture utilized in impact-resistant materials, particularly in arthropods. A few examples of Bouligand structures with organic-mineral or organic-organic components are discussed.

The lobster *Homarus americanus* cuticle, and other crustacean exoskeletons, exhibit a sophisticated hierarchical structure composed of chitin nanofibrils, proteins, and mineral nanoparticles (typically amorphous calcium carbonate) carefully arranged to form the robust macroscale multilayered cuticle (Figure 5a, VII). The α-chitin fibers found in the lobster exocuticle exhibit alignment on the [020] axis normal to the cuticle surface, which suggests a modulated alignment to enhance out-of-plane stiffness (Figure 5a, VII).[181] Starting from the molecular level, N-acetylglucosamine molecules, produced by enzymes,[182] (Figure 5a,I) aggregate to form polymeric α-chitin chains (≈10 Å chain spacing) (Figure 5a, II) that assemble into stronger anti-parallel crystalline 1D chitin nanofibrils wrapped with proteins (≈3 nm diameter) (Figure 5a, III). These nanofibrils assemble to form chitin-protein fibers embedded in a mineral-protein matrix (≈20–350 nm diameter) (Figure 5a, IV), which enhances strength and flexibility. The non-crystalline proteins associated with these chitinous matrices also contribute to toughness via sacrificial bonding or by acting as "soft" matrix elements between rigid fibrils to aid in crack deflection at fiber–matrix interfaces according to Dundurs' parameter.[111,113,136,137] These embedded fibers then form 2D honeycomb-like mineralized chitin-protein planes (Figure 5a, V) that stack with a rotation normal to the cuticle surface to form the helicoid structures used for localizing damage via crack twisting through the layers (Figure 5a, VI). This helicoid arrangement also has through-thickness pore canals, which facilitate biomineralization and ion transport to aid in growth during molting. The bulk 3D cuticle (1–3 mm) (Figure 5a, VII) is organized into three distinct layers: the thin epicuticle, the harder exocuticle (≈200–300 µm thick), and the thicker endocuticle (≈250 µm–2.5 mm). The exocuticle, with its smaller pore canals and tighter pitch of rotation, is designed to resist compressive forces, while the endocuticle offers ductility.[175,181] The hierarchical design of the lobster cuticle is not only effective in providing a robust structure but also optimizes material use. By controlling the architecture at various length scales, the lobster cuticle achieves a balance between rigidity, flexibility, and performance to defend against predators and hunt prey.

Similarly, in the dactyl club of the peacock mantis shrimp, the impact and periodic region below the surface of the 0D nanoparticle nanocomposite coating is a 3D structure composed of mineralized 1D α-chitin fibers (Figure 2b).[183–185] In the impact region, these anisotropic nanofibers (≈50 nm diameter) are arranged in a plane parallel to the club's surface in a herringbone arrangement. This optimized and modulated stacking of sinusoidal plies with specific clocking angles and graded amplitudes gives the dactyl club superior out-of-plane compressive strength while maintaining the toughness and fracture resistance needed to transfer the force behind its high-strain-rate punch. The sinusoidal arrangement of the impact region may further improve the toughness by introducing many interfaces afforded by the nanofiber architecture that inhibit crack growth via crack deflection and subsequent twisting.[186]

Below the impact region is the periodic region assembled and oriented chitin nanofibrils that are surrounded by an amorphous calcium phosphate and carbonate matrix. These nanoscale unidirectional sheets are stacked upon each other with subsequent offset in-plane angles to produce a 3D helicoid architecture.[176] Cracks that form upon impact must deflect at the many interfaces between the nanoscale fibers and subsequently twist in order to propagate, which significantly improves fracture toughness.[176,178,186,187] The entire club is also strengthened and toughened by the continuous fibrous pore canal tubules, which are oriented perpendicular to the fiber plane, and used for material transport during molting.[186] Comparative testing of the inner and outer regions of the dactyl club against geological fluorapatite (Figure 5g) demonstrated the difference in energy absorption for material with and without the helicoidal architecture via nanoindentation.[178] In their analysis of the highlighted regions of the load vs. contact depth curve where pop-in events occurred (Figure 5g), which are indicative of elastic energy release via cracking, there was an approximate 4X increase in contact energy absorbed. This is attributed to yielding within the club's outer layer before cracking, which is not observed in geologic fluorapatite that lacks the nanoscale features and interfaces found in the club.[178]

Similarly, other organisms have evolved helicoidal architectures to enhance survivability. These structures are found in beetle cuticles,[188,189] scorpion pincers,[190–192] lobster clubs,[136,193–195] crab shells,[106] fish scales,[196–200] and fish eggs.[201] Some of these structures are also non-mineralized. For example, in the elytra of the diabolical ironclad beetle *Phloeodes diabolicus* (Figure 5d), the endocuticle region (colored blue in Figure 5e) also exhibits a helicoidal structure built from lamellae composed of parallel bundles of fibers, which are further comprised of unidirectional chitin nanofibrils.[202] This helicoid-like architecture of the beetle endocuticle, which is subject to impact from birds, also provides toughened interfaces that encourage crack deflection and crack twisting to occur between the chitin fibers and cuticle proteins.[36,180] Another example is the coelacanth "living fossil" fish, which employs a similar strategy of a double helix within the collagen fibers of its protective scales to enable remarkable damage tolerance and protection against predation.[203]

To better understand the contribution of crack twisting in the overall fracture toughness of the helicoidal architecture, Suksangpanya et al. developed a theoretical model to predict the nature of crack propagation within (Figure 5h),[179] and subsequently validated the model by testing additively manufactured beams where the crack propagation path was carefully controlled (Figure 5i).[180] From the proposed model, it was found that the initial flat crack introduced into the helicoid structure (Figures 5hb and 5hc) has a tendency to twist (ϕ), such that the crack front is always a straight line and parallel to the fiber orientation (γ) with spacing (d). The local fracture mode also changes to reduce the local strain energy release rate to increase the necessary applied energy release rate to propagate cracks.[179] Furthermore, the crack driving force decreases with distance away from the crack front rotation axis, which promotes crack growth along the matrix, forming nested twisted cracks that spread the damage over a larger area.[179] Three-point bend testing of additively manufactured notched bars with variations in fiber

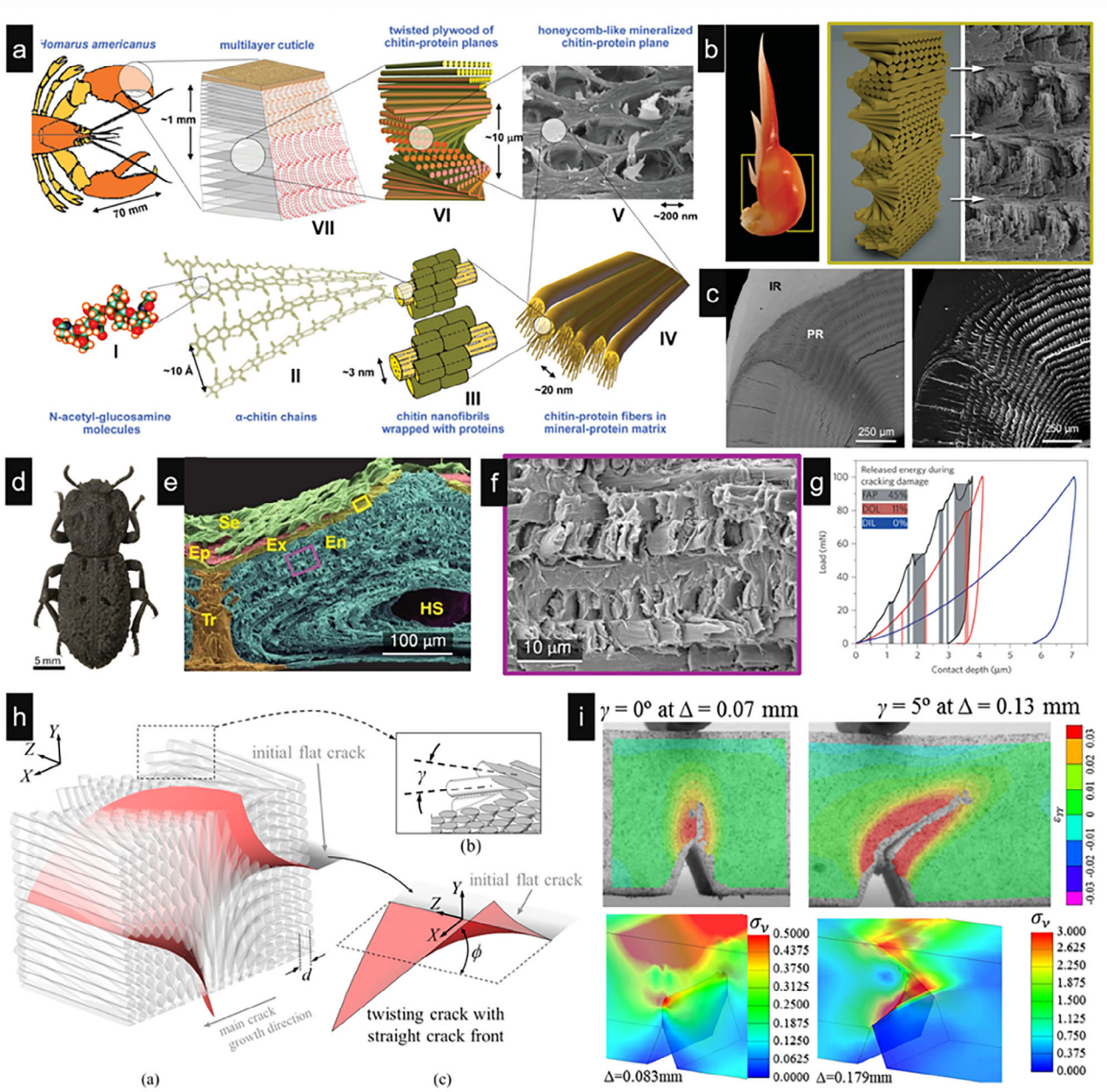

Figure 5. Helicoidal architecture in biological systems. a) Hierarchical structure of the lobster cuticle: a, I) N-acetyl-glucosamine molecules, a, II) antiparallel chains of α-chitin, a, III) chitin-protein nanofibrils, a, IV) chitin-protein fibers in a mineral-protein matrix (not shown), a, V) cuticle with pore canal system (in-plane cross-section), a, VI) twisted plywood structure, and a, VII) three-layered cuticle. Reproduced with permission.[175] Copyright 2010, Wiley. b,c) Helicoidal structural motif consisting of chitinous fibers surrounded by an amorphous calcium phosphate matrix within the periodic region (periodicity: ≈75 µm) of the dactyl club of the mantis shrimp, *Odontodactylus scyllarus*. b) A generalized three-dimensional model of a helicoid and accompanying SEM fractograph from the periodic region. c) Backscattered (BEI, left) and charge-contrast secondary (SEI, right) scanning electron micrographs of a transverse cross section through the dactyl club, indicating crack-arrest near the impact surface (IR: Impact Region) and at interfaces within the periodic region (PR). Adapted with permission.[176] Copyright 2012, AAAS. d–f) Helicoid structures within the cuticle of the Diabolical ironclad beetle (DIB), *Phloeodes diabolicus*. d) Image of DIB, e) false colored SEM of fractured section of beetle elytra. f) Helicoidal microstructure of chitin fibers, surrounded by a protein matrix, in the endocuticle. Adapted with permission.[177] Copyright 2020, Springer Nature. g) Nanoindentation curves of geological fluorapatite in comparison to the dactyl club outer layer (DOL) and dactyl club inner layer (DIL). Adapted with permission.[178] Copyright 2015, Springer Nature. h, i) Schematic illustration of a twisting crack behind an initial flat crack in the Bouligand structure in this study with interlayer spacing d (distance between adjacent fiber layers) and h, ii) pitch angle γ (difference in orientation of adjacent fiber layers). h, iii) The twisting crack is represented by a twisting surface. Adapted with permission.[179] Copyright 2017, Elsevier. i) (Top) Digital Image correlation strain distribution measured from 3D printed helicoid samples with a 0° (left) and 5° (right) misalignment between layers. (Bottom) Comparison with computational models. Adapted with permission.[180] Copyright 2018, Elsevier.

orientation (γ = 0°(Figure 5i, left), 5°(Figure 5i, right), 10°, 30°, and 45°) validated the predictions generated by the model while minimizing the contribution of competing mechanisms such as crack branching or sample delamination. This suggests that analysis of larger or more complex systems will require more powerful computational tools to capture the true behavior of the experimental system.[35,180]

While many of the aforementioned 3D structures are built from nanoscale building blocks to form ultra-tough structures, other organisms have evolved lightweight hierarchical porous 3D structures such as bones, teeth, horns, hooves, wood, and bamboo. This is made possible through the assembly of 1D nanofibers (collagen, keratin, and cellulose) and 0D nanoparticles (i.e., hydroxyapatite or silica) while maintaining strength and toughness.

Additional examples of low-density and tough 3D structures are found in the siliceous skeletons of diatoms and sponges.[204–206] Diatoms are a type of phytoplankton whose bodies range from 2 to 200 µm in diameter and are surrounded by a cell wall composed of nanosilica.[207,208] The diatom frustule (cell wall) has the highest specific strength (strength to density ratio) among any known biological material[209] and is comparable to the strongest natural polymers.[209–211] It is hypothesized that diatoms incorporate nanoparticles of silica into their cell walls to resist predation by copepods and digestion after consumption.[212,213] The frustule is primarily composed of two silica plates, the epitheca and hypotheca (top and bottom, respectively), which are colloquially referred to as valves.[214] The silicification process is not yet completely understood but is hypothesized to be enabled by silicon-interacting proteins (SITs) and mediated by silica deposition vesicles (SDVs), which template intricate nanoscale structures in three dimensions. The details of mineralization are outside the scope of this review, and we refer the readers to numerous references.[29,215–218]

In diatoms, the frustule is assembled from environmental silicic acid at physiological conditions within a specialized membrane known as the silicon deposition vesicle (SDV).[219,220] Within the SDV, diatoms synthesize ≈12–30 nm 0D silica nanoparticles as a precursor to their cell wall. These nanoparticles are then assembled by silaffins into a nearly defect-free biological composite of protein, polyamides, and silica.[209,216,218] Silaffins are poly-peptides which possess posttranslational modifications (such as phosphorylation and covalently attached polyamides), which enable them to assemble silicic acid into intricate patterned silica, resulting in the highly architected features present in diatoms.[217,221,222] The composition of the silica biological composite of diatoms has been studied in many model organisms, with large variations in resulting morphology depending on the chemical differences in the species-specific silaffins and long-chain polyamides.[29] In the *Coscinodiscus* diatom, the polyamines form a micron-scale hexagonal monolayer, which results in the precipitation of a honeycomb-network of silica at the largest pattern size. Once the hexagon pattern is established, the organic components phase segregate into smaller droplets within the pattern, creating new interfaces for silica deposition.[223,224] This results in self-similar patterns at progressively smaller scales, down to feature sizes of 50nm.[217] These patterns enable the frustule to function as a hierarchical structural nanoscale metamaterial built from their near defect-free assembly, which is responsible for the diatom's incredible specific strength at the macroscale.[221,225]

The mechanical response of different 3D diatom architectures has been studied. In the *Fragilariopsis kerguelensis* diatom, stress concentrations are distributed along the frustules by its microscale transversal ribs (costae). In Finite Element Method (FEM) studies without the nanostructured ribs (normalized to the same amount of material), it was estimated that the frustule fails with 60% less force. This is due to the mechanical interaction between the top and bottom plates of the frustule that is reinforced by the double wall honeycomb structure interface formed by the areola walls. This acts as an optimized 3D topology which is architected at the nanoscale for the given loading condition with a thickness of down to 70 nm.[204,226] This optimized 3D topology for mechanical strength must also be balanced with the biological needs of the organism. Luo et al. suggest that the pores formed by the honeycomb network inherent to diatoms' cell walls are stress concentrators that double as crack-arresting sites. This biologically necessary defect (utilized for exchange of gas and nutrients) is adapted by raised orifice reinforcements around each pore, decreasing the local FEM von Mises stress by 25%, thereby mitigating the failure mode.[221] Diatoms achieve their high specific strength through the near defect-free nanosilica domains, which are specialized for different loading conditions by species-specific organic templates.[29,209,217]

Sea sponges are siliceous marine invertebrates that are sessile filter feeders bound to the sea floor. Within the *Euplectella aspergillum* sea sponge, more commonly known as the Venus' flower basket, 0D nanosilica building blocks are used to create micron-sized fibers that form the intricate hierarchical lattice structures observed at the macroscale (ca. centimeters).[227,228] Its skeletal lattice allows fluid flow for feeding and waste removal without compromising structural stability in its natural deep-sea habitat. The incredible buckling resistance of sea sponge spiracles is the result of many different structures across dimensionalities. At the nanoscale, silica nanoparticles (≈50–200 nm) are templated by axial protein filaments. The mineral and protein are subsequently organized into alternating concentric layers of silica (0.1–2 µm) and layers of organic (5–10 nm) around a central core to form the spiracle.[41,205,229] These spiracles are then assembled to millimeter-scale lattices similar to those described in diatoms. Under nanoindentation and tensile testing, the multiple interfaces presented by the nanosilica-constructed layers of the spiracles delaminate and slide against each other to dissipate energy. During failure, cracks initiate in the outermost layers and must propagate through multiple concentric organic-mineral interfaces, which is afforded by the nanoscale structure to arrest and deflect cracks before proceeding to deeper layers. Upon further loading, the cracks propagate via deflection between the inner layers until they reach the inner core, where they ultimately fail.[230,231]

2.2. Biologically Inspired Structural Materials

While natural systems discussed in the previous sections exhibit exquisite architectures with robust mechanical properties, they are inherently limited by the narrow range of available biogenic minerals, which cannot function in conditions

required for most high-performance structural engineering applications. At the same time, biological materials are often constructed over days/weeks, making it difficult to implement their processes in industry. However, there are significant benefits of using blueprints from these natural structures, which have been optimized over millions of years, with high-performance nanomaterials and advanced manufacturing processes. This presents a transformational opportunity to manufacture ultrahigh-performance bio-inspired nanostructures for structural and other applications (i.e., optical, thermal, sensing, described in later sections).

2.2.1. 0D Bio-Inspired Building Blocks

0D building blocks are commonly used as nanoparticle filler materials in ceramic, metal, and polymer matrix nanocomposite engineering materials. Their addition improves the mechanical, thermal, optical, and electrical properties beyond those of the unmodified matrix, provided the interphase formed is strong and defect-free.[232–235] One such example of a bio-inspired polymer matrix nanocomposite is the impact-resistant silicon carbide (SiC)/chitosan nanocomposite coating developed by Hao et al.[236] By gradually increasing the volume fraction of SiC nanoparticles (≈60 nm) within the chitosan matrix, the Young's modulus and hardness of the ≈5–8µm thick coating increased up to 70% volume SiC, but diminished at 80% loading due to discontinuities in the matrix, leading to poor stress transfer.[237–239] Under high strain rates (i.e., $\approx 10^4\ s^{-1}$), coatings with 50% volume SiC provided the greatest damage area reduction against 10 and 100 repeated impacts. The strong interactions between the reinforcing particles and the matrix via the interphase allowed for particle rotation and translation, along with particle jamming, to maximize the energy dissipative capabilities of the coatings.[236] Further tuning of the particle morphology, crystallinity, and composition to more closely follow those found in nature, such as the bi-continuous HAP nanoparticles of the mantis shrimp, should yield further improvements, but requires further investigation of the biological system as well as additional improvements in bio-inspired processing techniques. In addition, integration of architected nanoscale ceramic reinforcing phases into polymeric matrices like the one described above can provide multifunctionality, such as improved barrier capability,[240] catalytic activity,[241–243] magnetism,[243–245] electrical conductivity,[246,247] anti-microbial,[248–251] enhanced biocompatibility,[252–254] flame retardancy,[255,256] and abrasion resistance.[257,258] This wide range of applications can be implemented in multiple industries.[259]

Silica-based materials have received considerable attention in bone tissue engineering for their biocompatibility and ability to covalently graft osteoinductive signaling peptides that promote bone regeneration.[260] Diatoms are able to precipitate silica nanoparticles via silaffins, in near ambient conditions with remarkable control over nanoparticle size and morphology.[261,262] This process has enabled the controlled synthesis of 0D silica nanoparticles used in tissue engineering and drug delivery.[263,264] A silaffin of interest, silaffin-1A,[265] and a peptide derivative (referred to as R5) were developed and used not only to make silica nanoparticles, but also to create a bio-inspired silica-forming protein glue for bone implants.[265] They successfully fused the R5 silaffin peptide with a recombinant mussel adhesive protein to create an osteopromotive silica nanoparticle (111.5 ± 31 nm) coating for titanium implants that improves the stability of orthopedic and dental implants. The nanoparticle coating allows direct control of the surface roughness of the implants for cell adhesion while providing cohesive strength an order of magnitude greater than traditional hydroxyapatite coatings. Jo et al. have utilized a modification of this peptide modified R5 to create a bio-inspired silica-forming protein glue for bone implants.[265–267] They successfully fused the R5 silaffin peptide with a recombinant mussel adhesive protein to create an osteopromotive silica nanoparticle (111.5 ± 31 nm) coating for titanium implants that improve the stimulate bone tissue growth to provide improved life and stability of orthopedic and dental applications of implants. The nanoparticle coating allows direct control of the surface roughness of the implants, which promotes bone tissue formation, for cell adhesion, while mechanically performing an order of magnitude higher in cohesion above traditional hydroxyapatite coatings.[267] The diatom's biosilicification process has also inspired different chemical mimics. In work by Ismail et al. polyallylamine hydrochloride was used to mimic the function of silaffins to deposit negatively charged nanosilica onto the surfaces of steel fibers to create stronger cementitious composite materials due to the increased interfacial bonding, afforded by the nanosilica coating, between the steel and cementitious matrix.

2.2.2. 1D Bio-Inspired Features

The design of biological macromolecules at the nanoscale provides abundant inspiration for the fabrication of structural engineering materials.[120,262] Natural nanofibers composed of proteins or polysaccharides play a pivotal role in imparting toughness, tensile strength, and energy dissipation to biological tissue. Both the nanoscale structure (i.e., molecular architecture) and the organized arrangement of these fibers, with intermolecular bonding, have provided insight for the design and fabrication of strong, tough bio-inspired fiber-based materials, which are discussed below.

Inspired by the high specific tensile strength and stiffness observed in cellulosic nanofibers, ultra-strong fibers were fabricated using bacterial cellulose via a wet-stretching and twisting method (**Figures 6e–h**) that imparted superior specific tensile strength and modulus compared to natural cellulose and silk-based materials (Figures 6i–j).[268] Similarly, Li et al. significantly improved the tensile strength, flexural strength, and toughness of bamboo by compacting the cellulose fibers present within biogenic bamboo.[269] Bulk bamboo stalks were flattened and chemically treated to remove lignin and hemicellulose, which allows for more hydrogen bonding and van der Waals interactions between cellulose nanofibrils. The resulting mechanical properties of densified bamboo (up to 1 GPa tensile strength and 400 MPa flexural strength) surpass those of some engineered steels and metallic alloys, making it a promising sustainable and lightweight alternative material for use in aerospace and construction.[269]

In a similar strategy, protein-based biological fibers were used as components to make biologically based nanostructures. Here, a hierarchical keratin-based shape memory material was

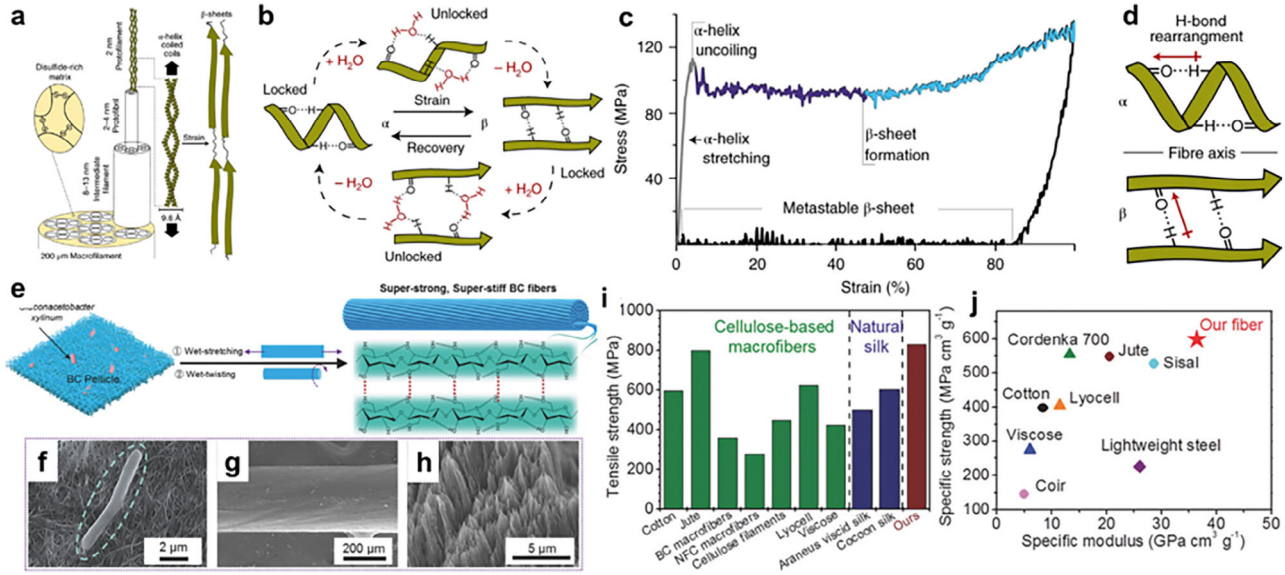

Figure 6. Bio-inspired designs of strong and tough fiber materials. a) Schematic showing hierarchical structure of wool keratin and transition from α-helix to β-sheet that is feasible under strain. b) Schematic representing the water-triggered shape memory mechanism. c) Mechanical tests and toughening mechanisms of keratin fibers. Adapted with permission.[270] Copyright 2021, Springer Nature. e) Schematic of fabricating strong and tough cellulose macrofibers based on bacterial cellulose. f–h) SEM images of the as-fabricated cellulose fibers. m,n) Comparison of mechanical properties and Ashby plot. Adapted with permission.[268] Copyright 2017, Wiley.

developed using 1D keratin fibers extracted from biogenic wools (Figure 6a).[270] The transformation of keratin fibers from α-helix to β-sheet conformation provided the resulting nanofibers with extraordinary tensile strength and toughness while the reversible hydrogen bonds inside the keratin macrofibrils yielded shape memory effects within 3D printed keratin-based structures (Figures 6b-d). These studies highlight the promise and potential of robust structural materials by leveraging specific nanoscale strengthening and toughening mechanisms of biological macromolecules. Extending such bio-inspired designs to synthetic polymers offers a compelling route to further enhance material functionality and performance for a wide range of applications.

The aforementioned description of biological fibers, cellulose, and keratin provides insight towards producing 1D fibers using additive manufacturing (AM). Here, the creation and development of sustainable feedstock has driven research towards bio-inspired alternatives to the polymeric materials currently used.[271] For example, templated growth of oriented mineralized nanorods within the mature chiton teeth by chitinous scaffolds, inspired Montroni et al. to synthesize 1D chitin-based nanofibers using a one-step multivariable process. By tuning the induced shear stress during the extrusion of chitinous feedstocks through a variety of needle gauges using direct ink write (DIW) printing, control over the nanoscale fibrillar alignment, which increased tensile strength, was achieved.[272] The biocompatibility of these chitin-gel scaffolds with aligned 1D chitin fibril nanostructures also supported the culturing, localization, and growth of mammalian cells, which demonstrated the potential of nano-architected chitin in applications beyond structural engineering. For example, tissue engineering has benefited from chitinous scaffolds through the fabrication of hydrogels and matrices with tunable form and mechanical properties.[139,273,274] Other engineered applications of nano-scale chitin range from drug delivery, cancer treatment, food packaging, and energy storage.[275–278]

Beyond 1D organic-based nanomaterials, ceramic composites utilizing cross-lamellae nanostructures found within gastropod shells have also been employed to augment engineering materials via with ultrastructure optimization.[146,279] Karambelas et al. utilized a process termed SHELL (Sequential Hierarchical Engineered Layer Lamination) to sequentially architect the cross-lamellar structures in silicon nitride/boron nitride ceramic composites, where the Si_3N_4 and BN are analogs of the aragonite planks (ceramic phase) and conchiolin (organic phase), respectively. Through co-extrusion, second-order, and third-order lamellae analogs were created (**Figure** 7A), where the blue layers correspond to Si_3N_4 and the green regions correspond to BN. Through cutting and rebonding of the laminates, the cross-laminated structure was recreated, exhibiting an elevated work of fracture of 3620 J m^{-2} vs 2860 J m^{-2} for monolithic Si_3N_4 (Figure 7B). This is a result of both crack deflection and bridging within the ceramic system, a property directly observed and replicated from biogenic cross-lamellar structures (Figure 4C). While there have been successful replications of gastropod cross-laminated structures, as featured by Karamelas et al., the inherent multiscale complexity of the structure has provided a barrier towards replication at smaller length scales.[279,280] While features produced were not at the nanoscale, the cross-lamellar architecture has demonstrated improvements in impact resistance by 85%, which is due to numerous crack deflection events at the interfaces present between the multi-order arrangement of lamellae.[281] Adaptation of these mimetic structures on the nanoscale should further enhance impact resistance for use in protection against aerospace debris or personal protective equipment, such as helmets and armor.

While bio-inspired designs have been used to create 1D engineered materials such as ceramic composites with superior

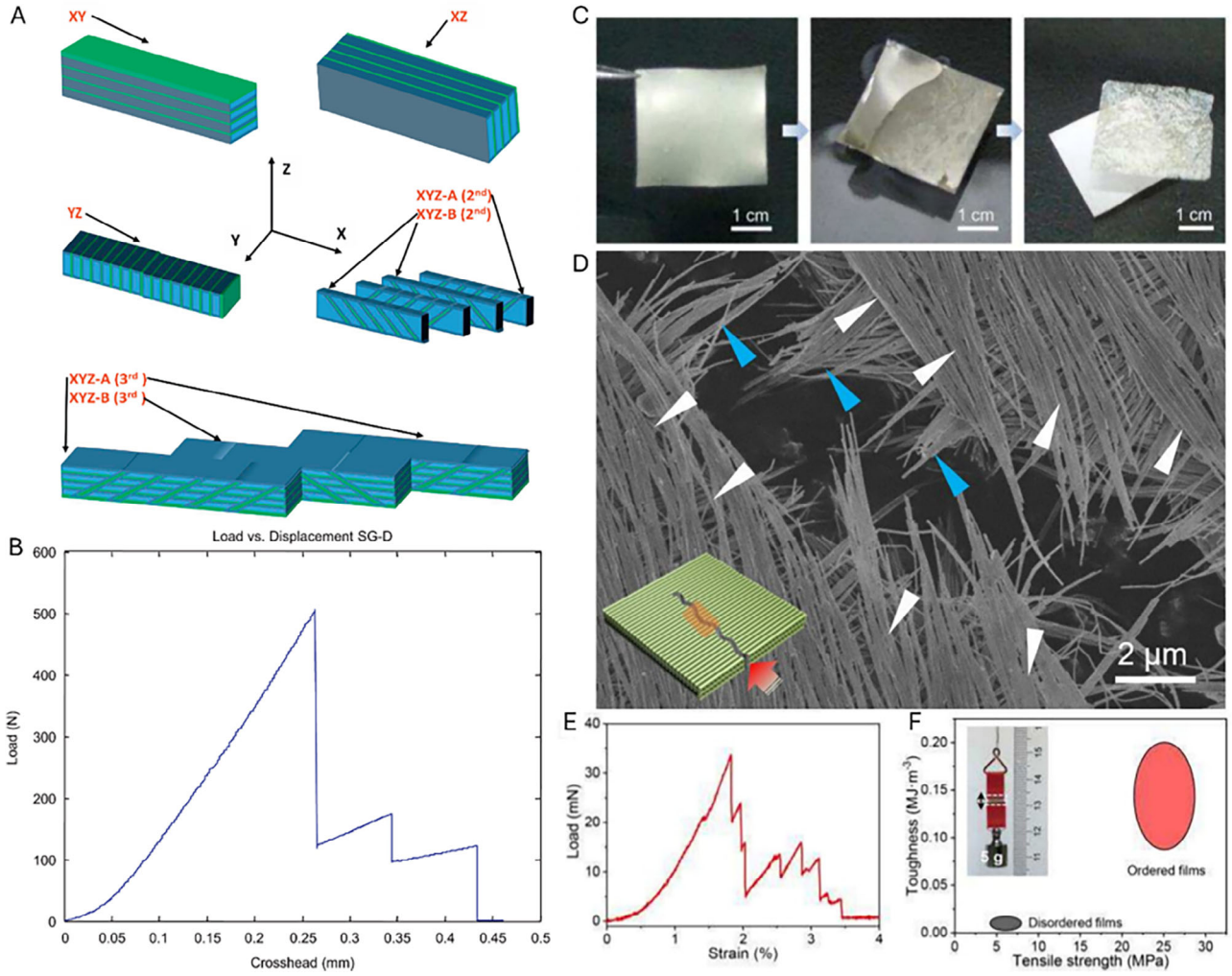

Figure 7. a) Orientation of Si_3N_4 (blue) and h-BN (green) laminates. b) Four-point bend test load vs displacement for biomimetic ceramic. Adapted with permission.[279] Copyright 2013, Elsevier. c) Mono-lamellar Ag-NW film was separated from the porous MCE substrate in water. d) Crack extension characterization of 5-lamellar Ag NW film. High magnification SEM image shows typical debonding and pullout of Ag-NW in the fracture surface of a freestanding ultrathin Ag-NW film. White arrows indicate the direction of load redistribution. Blue arrows indicate the path of crack propagation. Inset image shows a schematic diagram of crack propagation. e) Typical sawtooth pattern on the load-displacement curve in mechanical tearing tests. f) Ashby diagram of toughness versus tensile strength for disordered and 5-lamellar Ag-NW films. Adapted with permission.[286] Copyright 2024, ACS Publications.

mechanical performance, additional functionality can be achieved. For example, one-dimensional nanowires (NWs) have emerged as promising building blocks for inverse photoconductivity, photocatalytic activity, and ionic conductivity in polymer electrolyte batteries.[282–285] Integrating functional 1D NWs into bio-inspired structural motifs offers a compelling strategy to improve both the durability and functional performance of these systems. Zhang et al. utilized the cross-lamellae structure to build nanoarchitected electrically conducting devices with enhanced mechanical stability. Here, silver NWs and polyvinylpyrrolidone (PVP) were used to mimic the aragonite lamellae and organics of the shell, respectively.[286] PVP-coated silver NWs, with diameters of 55 nm and lengths of 4 μm, were placed into suspension and shaken in an oscillator to generate large amounts of bubbles, which helped to facilitate the self-assembly of the silver NW enabled by the oxygen-silver interactions present between the PVP and silver. The bubbles were subsequently removed through centrifugation, and the NW films were extracted via a mixed cellulose ester (MCE) substrate (Figure 7C). The organization of silver NW in the cross-lamellar structure (Figure 7D) exhibits crack deflection, as seen within the biological system, with debonding and fiber pullout to toughen the material (Figure 7D). Energy dissipation is observed in the sawtooth patterns observed in Figure 7E. While the cross-lamellar assembly of NW films offers marked improvement over disordered films (Figure 7F), the difficulty of fabricating nanoscale mimetic structures that encapsulate the multiple degrees of complexity featured in the cross-lamellar structure prevents the utilization of the full breadth of toughening mechanisms seen in biogenic cross-lamellar structures. Despite only replicating a simplified version of the structure, Zhang et al. created a silver nanowire film that is more

structurally robust than non-architected 1D silver nanowires while preserving its electron transport capabilities, opening the door to advanced nanodevice assemblies for long-term operation, by increasing its damage resistance over time.

2.2.3. 2D Bio-Inspired Features

Similar to 1D nanofibers and nanorods, 2D structures—such as nanoplatelets and thin walls have also been utilized using bio-inspired methods to strengthen materials. Nacre is one of the most well-known examples, and has attracted significant research interest as a source of bio-inspired designs. In an effort to recycle over 10 million tons of annual shell waste and create sustainable yet strong ceramics, Yan et al. developed a method to create a conductive ceramic from recycled aragonite nanoplates. Aragonite plates from biogenic nacre were extracted by dissolving the biopolymer matrix and subsequently functionalized via hydrogen bonding with 1.8 nm-thick MXene sheets, a family of 2D transition metal carbides and nitrides.[18,287] To replicate the chitin-protein matrix in natural nacre, a mixture of CNF and PVA was used as the matrix phase.[18,288,289] The resulting slurry of functionalized aragonite, MXene, and CNF/PVA was doctor-bladed onto a PET substrate, dried, and hot-pressed to form a 3D conductive nacre composite (**Figure 8a**). SEM microscopy of the conductive nacre cross-section is displayed in Figures 8b,c. Backscattered electron microscopy was further used (Figure 8c) to differentiate the aragonite plates, MXene sheets, and CNF/PVA matrix. In addition to augmenting the fracture toughness of biogenic nacre by over 1.6 times (Figures 8d–g), the resultant composite material also exhibited electrically conductive properties. Figures 8d–g also indicates that conductive nacre provides similar toughness and strength compared to mimics synthesized via the same protocol without MXene sheets, while eliminating the need for environmentally unfriendly epoxy resins. Hydrogen bond interactions between the CNF-PVA matrix and the MXene functionalized aragonite plates enhance the flexural strength of the conductive nacre, surpassing that of biogenic nacre and mimics without MXene. The presence of MXene sheets also bridges neighboring plates, resulting in a bulk conductivity of 0.01 S m^{-1}, displayed in Figure 8e.[18] Additionally, the presence of MXene in the conductive nacre enables it to possess a monitoring function for damage as well as shielding against electromagnetic interference, offering potential applications in the aerospace and defense industries.

Ceramic aerogels, traditionally used for thermally insulating applications, are greatly limited by their lack of robust mechanical properties.[291–295] Synthesis of aerogels with 1D ceramic nanofibers and imitating the brick-and-mortar structure of nacre (Figure 8h) has shown promise in augmenting energy dissipation, tensile strength, and toughness by over tenfold compared to traditional ceramic nanofiber aerogels.[85] Zhang et al. demonstrated the principle via the synthesis of SiO_2 aerogels, utilizing 2D SiO_2 nanofiber membranes (NFM) in place of the aragonite platelets and montmorillonite nanosheets (MMT) in place of the biopolymer matrix to bind the platelets.[18,85] SiO_2 ceramic nanofibers were fabricated via traditional methods of electrospinning and sintered into a nanofibrous membrane. The resultant membranes, with ceramic nanofibers and Montmorillonite nanosheets, were then soaked in a AlBSi (an aluminoborosilicate-based ceramic) precursor solution for 2 h. The soaked 2D nanomembranes were stacked and frozen with liquid nitrogen and calcined at 600 °C for 1 h to form the ceramic aerogel. Figures 8j,k illustrates the proposed interactions of MMT nanosheets fortifying the interfacial bonding between the ceramic nanofiber sheets and their subsequent assembly process through layer-by-layer immersion and freeze drying to form the resultant bulk ceramic aerogel. The resultant 3D ceramic aerogel fabricated with the nacre microstructure was able to withstand a maximum compressive stress of 317 kPa, with the stress distribution on the mimetic aerogel presented in Figure 8i, surpassing traditional ceramic aerogels by a factor of 5–10 times.[296–300] In addition, Zhang et al. demonstrated multifunctionality of these nacre-inspired materials through their use of thermally insulating aerogels, broadening their application to space travel. Equipment, such as rovers or habitation spaces, will be able to more readily employ these materials as ceramic aerogels are able to be utilized in more load-bearing components.[85] Recent work by Zhu et al. demonstrated a further increase in the operational temperature of nacre-inspired ceramic materials to 1300 °C[301] by substituting the polymer matrix with a spongey ceramic.

In addition to the retrosynthesis and sol-gel methods utilized to synthesize the nacre-like systems described above, researchers have also explored bio-inspired synthesis pathways to better reproduce the biogenic nacre structure. To that end, Finnemore et al. proposed a layer-by-layer deposition method that involves both organic functionalization and inorganic crystallization, creating artificial nacre (Figure 8m) with 400 nm 2D platelet-like structures (Figure 8l). Glass slides were cyclically dip-coated into poly (acrylic acid) (PAA) and poly (4-vinyl pyridine) (PVP) solutions to form a continuous 30 nm thin film. The film was etched (i.e., the PVP layer was partially etched to form pores) and subsequently immersed in a calcium-containing solution and mineralized to form calcium carbonate layers (separated by polymer layers) via a vapor phase and humidity-driven crystallization method (Figures 8n,o). Interestingly, the nanoporosity in each PVP layer enabled pathways for calcite growth, connecting each adjacent layer and thus replicating the aforementioned nanoscale mineral bridges in biological nacre. The artificial nacre also demonstrated analogous fracture mechanisms and similar ratios of plane strain modulus (Figure 8p) as compared to natural nacre.[290]

2.2.4. 3D Bio-Inspired Features

Over the past decade, a significant effort has investigated common design themes in natural systems that enable strength, toughness, and stiffness.[35] One of the most dominant architectures observed has been the helicoidal structure (and described in the biogenic systems earlier). This robust architecture, observed in many biological systems, has been emulated using microscale fibrous components, at macroscale dimensions in engineered composites. Helicoidal architectures applied to glass,[302,303] carbon,[304,305] and Kevlar[306] fiber-based composites have demonstrated superior toughness, perforation resistance, and energy absorption compared to conventional quasi-isotropic fiber layups currently used in industry.[307] These improvements are attributed to the large in-plane delaminations

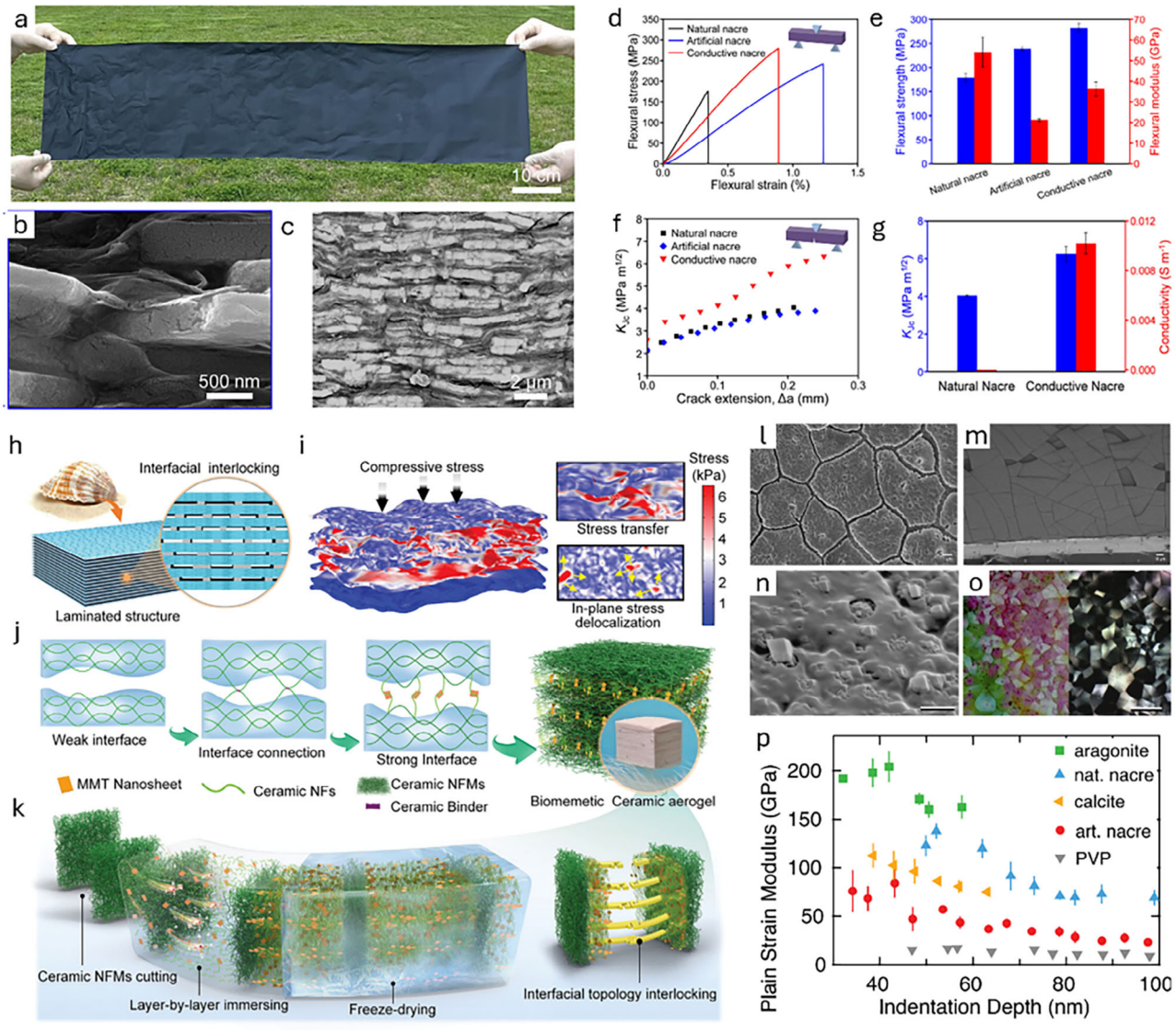

Figure 8. a) Digital photograph of a large area (100 cm × 25 cm) layered composite film fabricated by blade coating. b) SEM image of the cross-section of the conductive nacre showing lamellar structure. c) SEM image of the cross-section of the conductive nacre is taken using backscattered electrons. d) Flexural stress-strain curves of the natural nacre, artificial nacre, and conductive nacre. e) Comparison of flexural strength and flexural modulus of the natural nacre, artificial nacre, and conductive nacre. f) Rising crack extension resistance curves (R-curves) of the natural nacre, artificial nacre, and conductive nacre showing the resistance to failure in terms of the fracture toughness (K_{JC}) as a function of crack extension (Δa). g) Comparison of fracture toughness and electrical conductivity of the natural nacre and conductive nacre. Adapted with permission.[18] Copyright 2024, Wiley. Nacre-biomimetic structure design and fabrication of ceramic aerogels. h) Conceptual structure design principle inspired by nacre. i) Stress distribution of the laminated structural model showed stress transfer and in-plane stress delocalization. j) Weak to strong interface structure design concept for biomimetic ceramic aerogels. k) Fabrication process of biomimetic ceramic aerogels with laminated structure and interfacial topology interlocking. Reproduced with permission.[85] Copyright 2024, Wiley. l) Partially demineralized biogenic and m) a single layer of artificial nacre, showing the crystalline domain boundaries. n) SEM image showing early-stage crystallization through single PVP pores in a trilayer of calorg/organic/calorg (scale bar, 500 nm). o) Optical micrograph showing 5–35 μm birefringent crystalline domains (right: though crossed polarizers) (scale bar, 25 μm). p)The plain strain moduli for the two natural and three man-made samples as a function of the indentation depth. Adapted with permission.[290] Copyright 2012, Springer Nature.

and unique spiraling damage pattern that spread the damage from impacts over a larger area (**Figures** 9e–h), while also providing a more tortuous crack growth path.[176,178,186,187,308] For example, in Figures 9a–d, a 49% reduction in dent depth and 16% improvement in residual strength over quasi-isotropic layups were observed in medium angle (≈16.3° alignment) helicoids for 100J drop tower and compression testing, respectively.[304] These helicoid-based composites are now being used in the sporting industry with potential for the energy and automotive sectors.[309]

While there are great successes in mimicking these helicoidal structures at the micro- and macro-scale,[313–315] the synthesis of nano-scale helicoidal structures has not seen such prevalence. Nevertheless, the development of additive manufacturing

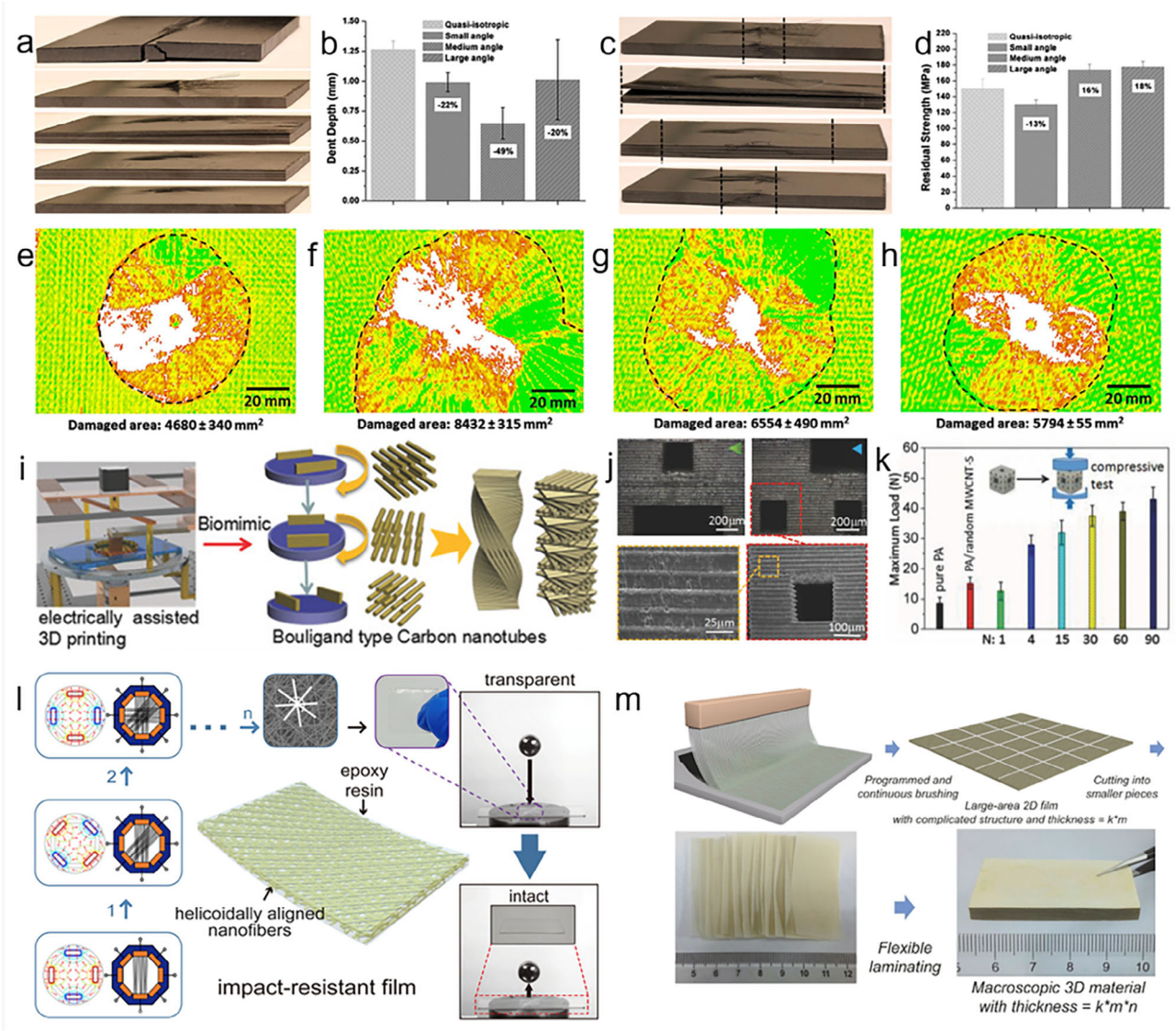

Figure 9. a) Photographs showing damage (from top to bottom) in unidirectional, quasi-isotropic, small-angle, medium-angle, and large-angle carbon fiber reinforced composites after 100J drop tower testing. b) Dent depth measurements for each sample as percentage reduction in dent depth listed for helicoidal samples. c) Photographs of damage in (from top to bottom) quasi-isotropic, small-angle, medium-angle, and large-angle composites after compression tests. d) Residual strength calculated from compressive data, with percentage change listed for helicoidal samples. Ultrasonic C-scan images showing internal damage fields in the e) quasi-isotropic, f) small-angle, g) medium-angle, and h) large-angle composites after drop tower testing, showing the increase of in-plane damaged area after a 100J impact. Adapted with permission.[304] Copyright 2014, Elsevier. i) Schematic diagram of the controlled alignment of carbon nanotubes by the rotation of electrodes immersed in a photocurable resin bath. Progressive rotation of electrodes and curing of resin by a digital micromirror device (DMD) produces structures in j) with helicoidal arrangement. k) Compression tests of the printed samples with different fiber clocking angles, where N = 1 is a rotation angle of 45°, N = 15 is 12°, N = 30 is 6°, and N = 90 is 2°. Adapted with permission.[310] Copyright 2017, Wiley. l) Schematic illustration of electrospinning setup with patterned collector and programmable voltage collector used to fabricate a periodic helicoidal microstructure within a transparent impact resistant film. Reproduced with permission.[311] Copyright 2019, ACS. Schematic illustration and digital micrographs showing high-efficiency 'brushing and laminating' strategies for flexibly fabricating biomimetic macroscopic 3D bulk materials. Adapted with permission.[312] Copyright 2018, Oxford University Press.

techniques capable of controlling nanoscale features has advanced substantially in the last decade due to it being one of the most effective and efficient ways to fabricate customized parts with complex geometries. One such method developed by Yang and co-authors utilizes electrically assisted nanocomposite 3D printing to dynamically align surface-modified multiwalled carbon nanotubes (MWCNT-S).[310] In this modified stereolithography method, a photo-curable resin containing MWCNT-S is cured after mask images are projected upward onto the bottom of the substrate by the projector. By controlling two parallel plate electrodes to apply a rotating electrical field in tandem (Figure 9i), a Bouligand-type anisotropy can be induced in the final MWCNT-S reinforced architecture (Figure 9j).[310] The printed structures were then tested with the compression force vertical to the

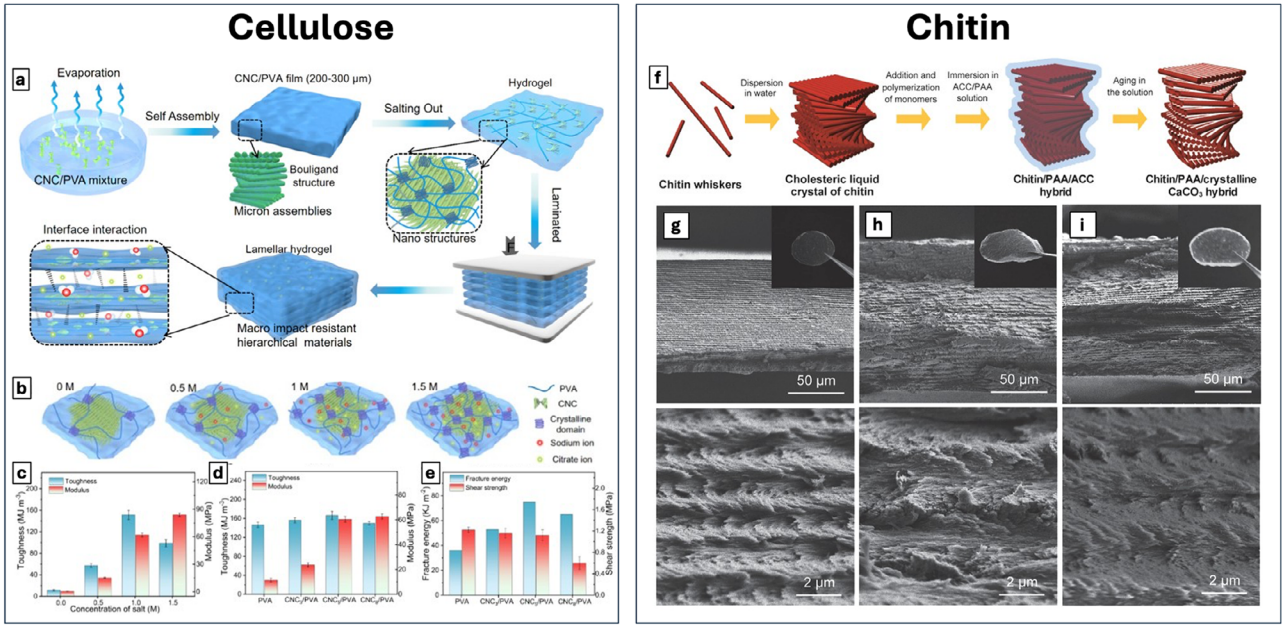

Figure 10. Schematic illustration of a) poly (vinyl alcohol)/cellulose nanocrystals (CNC/PVA) composite lamellar hydrogel fabrication process with the helicoid multiscale structure. b) Fabrication of CNC/PVA hydrogels by salting out sodium citrate solutions of varying concentrations. c) Modulus and toughness of CNC_5/PVA hydrogels after salting-out in sodium citrate solutions of varying concentrations. d) Modulus and toughness of CNC/PVA hydrogels with varying CNC concentrations. e) Fracture energy and shear strength of CNC/PVA hydrogels with varying CNC contents. Adapted with permission.[316] Copyright 2024, ACS. f) Schematic representation of the development of helically ordered chitin/$CaCO_3$ hybrid materials. g) SEM micrographs of the cross sections of the chitin/PAA organic template sample, and the films after the $CaCO_3$ crystallization processes for h) 1 day and i) 7 days. Adapted with permission.[317] Copyright 2015, Wiley.

alignment of the Bouligand composite. The maximum load of these samples was profoundly enhanced and attributed to the fracture resistance of the helicoid, with smaller rotation angles improving its ability to withstand deflection (Figure 9k).

Another method that utilizes a similar electrical field-controlled alignment of nanofibers was developed by Chen et al. In their work, helicoidally aligned nanofibers were prepared by an electrospinning system that collected the spun nanofibers with specified pitch angles based on a programmable voltage control system.[311] Four pairs of electrodes were mounted on the collector of the electrospinner to guide the stretching and alignment of nanofibers through electrostatic interaction along the electrodes. This specialized setup deposited unidirectionally aligned nanofibers, layer by layer, with a clockwise rotation to form a transparent nanofiber helicoid film(Figure 9l). The tensile strength and ductility of the composite films reinforced with 3 vol% nanofibers increased by 50% and 150%, respectively, and outperformed the toughened glass film and resin film controls in steel ball drop testing. The impact-resistant performance of these helicoid-bearing films suggests promising use as a protective layer in applications such as bendable displays and airplane windows.

In a simpler approach, Chen et al. demonstrated control over nanofiber orientation through brushing-induced assembly.[312] In this method, a dispersion of hydroxyapatite (HA) microfibers and sodium alginate (SA) polymer was formulated to mimic typical inorganic 1D building blocks and polymer matrix, respectively, found in nature (Figure 9m). This mixture was deposited across a heated substrate using a commercially available brush to form 2D films that contained highly ordered arrangements of HA fibers embedded in a SA matrix. By precisely manipulating the angle and orientation of the 1D micro/nanofibers between each film layer, 3D biomimetic twisted plywood structures similar to those found in nature were successfully fabricated. Mechanical testing showed that the strength and stiffness of the materials decreased as the fiber twist angle increased, however, samples with the ≈10° configuration retained remarkably high values (257.7 MPa and 15.6 GPa), outperforming the more extreme twist angles. Post-failure SEM imaging revealed that cracks propagated preferentially along the axial direction of the HA fibers, occasionally deflecting between adjacent HA and SA layers. Employing this strategy allows the engineering of nano/microstructural features at the macroscale for a variety of different materials and systems.

Beyond additive manufacturing, materials such as cellulose nanocrystals (CNC), can self-assemble into helicoids during drying, driven by the chirality of the CNC surfaces, which imparts a torque along the twist direction when in contact (**Figure 10a**).[318] To control the pitch angle of CNC helicoids, the concentration[319] and surface chemistry[318] can be modified. Cui et al. successfully fabricated helicoid CNC/polyvinyl alcohol hydrogels via an evaporation-based self-assembly and salt-out technique, which yielded a 9-fold improvement in tensile strength and 13-fold improvement in toughness compared to films only immersed in DI water due to promoted aggregation and crystallization of PVA chains (Figures 10b,c).[316] The combination of the rigid 3D CNC helicoid structures with the soft PVA networks and the multiple supramolecular interactions between them results in a

composite with a 5.5-fold improvement in elastic modulus, a near doubling of fracture energy, and force attenuation of 80.4% in impact tests when compared against non-structured PVA hydrogels (Figures 10d,e). Integration of helicoid CNC nanorods yields the same benefits as those at the macroscale, which emphasizes the versatility of the helicoidal architecture at various length scales.

Self-assembly of 3D helicoidal structures using nanoscale constituents was also achieved by Matsumura et al. through chitin-$CaCO_3$ hybrid materials.[317] Colloidal liquid-crystalline chitin assemblies were used to form chitin-whisker suspensions that subsequently developed a fingerprint texture due to the helical ordering of cholesteric structures. These assemblies were then fixed through photopolymerization of PAA and a crosslinker, resulting in a stable gel-like scaffold on which $CaCO_3$ mineralization could occur (Figure 10f). To accomplish this, calcium precursors were introduced to the cured helicoidal chitin gels, allowing for mineralization via the controlled diffusion of carbonate ions. The helical structure of the chitin template was maintained as the $CaCO_3$ crystallized to calcite. SEM cross sections of the films before and after mineralization demonstrate this structure (Figures 10g–i), providing insight into how biologically-inspired templating can guide the synthesis of hierarchically structured hybrid materials.[320] This design and tailorable fabrication method, with a broad array of materials selection, offers significant potential for multifunctional impact-resistance materials, such as structural batteries, self-cleaning panels, optically active windows, etc.

3. Optical Materials

Optical biomaterials are among the most captivating natural innovations. These structures can manipulate light through precision micro- and nano-scale architectures with refined chemical composition. Leveraging self-assembly and hierarchical organization with a limited material palette, biophotonic systems can create not only brilliant structural colors, but also fulfill roles such as communication, photosynthetic enhancement, anti-reflection, and thermoregulation. Such naturally evolved strategies offer powerful design principles for constructing bio-inspired optical materials with multifunctionality and tunable optical performance that can be utilized in engineering-relevant applications such as communications, defense, energy, etc. In both biological and related inspired systems, the optical properties arise directly from the material composition and related nanoscale structural features (such as nanopores, nanotubes, and multilayered lamellae) that govern how different wavelengths of light are reflected, transmitted, or absorbed.[321] These nanostructures, often arranged hierarchically and with precise periodicity, function through mechanisms like interference, diffraction, and scattering, offering wavelength-specific responses that can be mimicked and tailored in synthetic analogues. Understanding and replicating these optical effects thus relies on elucidating the fundamental structure–property relationships embedded at the nanoscale.

3.1. Biological System Designs

A remarkable diversity of materials exhibiting unique optical properties can be observed in organisms, manifested either as controlled pigmentation or highly periodic ultrastructures.[322–325] Pigments generate colors by selectively absorbing and reflecting specific wavelengths of light, while micro- and nano-structures manipulate light, producing a range of colors without the use of chemicals.[323,324,326] In this section, structure-based optical biomaterials are discussed in detail based on their primary functions observed in nature. Optical structures of different sizes and morphologies can be found in both animals and plants, serving multiple optical functions,[327] including communication (e.g., warning, attraction, camouflage), photosynthetic efficiency, anti-reflection, and thermoregulation, ultimately contributing to a significant increase in survival and fitness.[325,328–330] One of the most striking examples of natural optical materials is the vibrant and iridescent coloration seen in numerous insects, birds, and fish.[328] The formation of these optical materials involves mainly: i) self-assembly of organic components into stable, ordered/hierarchical patterns, which is functionally regulated at cellular levels (e.g., chitin self-assembled scales of the *Morpho* butterfly); ii) biomineralization (i.e., the controlled deposition of minerals within organic matrices), enabling organisms to form hard, often translucent or iridescent ordered structures (e.g., the intricate silica frustules of diatoms with highly ordered/patterned micro-nanopores).[82,331] As previously mentioned, many organisms have evolved optimized engineering structures using only a limited set of materials, which often serve additional functions. Optical materials are often combined to provide a structural support function. Some examples of dually functional optical/structural materials include aragonite and calcite in mollusk shells and echinoderm skeletons, chitin in the arthropod exocuticles, guanine in fish scales, keratin in avian feathers, and cellulose in plants.[332,333]

3.1.1. Structural Color

Iridescence in biological systems plays a crucial role in intra- and inter-specific communication (i.e., interactions within the same species or between different species).[332,333] As seen in *Morpho* butterflies and hummingbirds, it is used for mate attraction, species recognition, and territorial signaling, or also for predatory avoidance through camouflage and mimicry.[334,335] *Morpho* butterflies showcase iridescent blue hues resulting from the chitinous multilayer micro and nanostructures. Tree-like chitinous shapes arranged in rows found in the *Morpho* scale diffract and interfere with light, creating vivid colors through structural coloration.[322,324,336,337] The layered structure strongly reflects blue wavelengths while canceling out others through "constructive interference."[328,338] The precise color reflected is determined by the shape of these structures and the spacing between them, ranging from 0.5 to 5.0 µm, depending on the species.[336] The refractive index of the cuticle material is crucial in determining the conditions for the interference and directly influences the efficiency and wavelength of reflected light. As demonstrated on the single-scale microstructure of two *Morpho* species, the difference in refractive index n between chitin ($n \approx 1.56$) and air ($n \approx 1$) creates strong reflections at each interface.[336] Kinoshita et al. also discovered that the presence of some irregularity in the ridge height eliminates the interferences among the

ridges, resulting in a diffuse and broad reflection of a uniform coloration.[324,338]

While *Morpho* coloration results from an ordered multilayered system, other insects achieve iridescence through alternative photonic designs. A notable example is in the elytra of the beetle *Trigonophorus rothschildi varians*, consisting of a multilayered structure with randomly distributed cylindrical holes that reflect light, resulting in orange, green, and violet colorations.[87] Birò et al.[87,338] examined these natural structures using a combination of SEM, optical measurements, and simulations to reveal non-specular, wide-angle reflectance due to the intercalated design. In particular, the cylindrical rods within the multilayer scatter light over a broad angular range, enhancing visibility from different perspectives. Nanostructural coloration can also be found in hummingbirds. Their feather barbs have small, flat melanin structures (i.e., platelets about 2.5 μm wide) immersed in a keratin matrix, with specially designed air gaps. The unique nanometer-scaled melanin/keratin architecture with a refractive index of ≈2 interacts with light, reflecting, refracting, and thus resulting in vivid color displays.[339,340] The mosaic arrangement and physical characteristics of these platelets differ subtly among species, creating a spectrum of colors tailored to each hummingbird's specific needs, such as mating or territorial defense. Giraldo et al.[339] studied the feather variability and the reflective properties within the genus *Coeligena*. The coloration results from two key factors: the Venetian-blind-like alignment of the barbules and the V-shaped angular orientation of barbules on opposite sides of the barbs (**Figure 11**A). As illustrated in Figure 11, scanning and transmission electron microscopy revealed the angled positioning of laminar and sidewall structures within individual barbules (Figures 11B–E), while angular reflectance measurements and scatterograms confirmed species-specific light-scattering behaviors (Figures 11F,L–O). These optical properties are closely tied to the nanostructural organization of the barbules, with angular inclination (δ) influencing the directional reflectance and iridescence, which determines the bird's macroscopic appearance. In particular, the angle between the primary axis of the barb and the lamella, δ, increased from *C. violifer* (0°) to *C. prunellei* (39°), while γ, the angle between barbules on opposite sides of the barb, decreased from 173° to 117° (Figures 11H–K). These structural changes correspond with the scatterograms (Figures 11L–O), which display increasingly divergent light reflections, indicating species-specific scattering behavior driven by fine-scale morphological differences. Functionally, these configurations modulate how light is reflected during courtship. When γ is close to 180°, as in *C. violifer*, reflections from both sides merge into a single, intense flash (Figure 11L). In species with smaller γ, like *C. prunellei*, the reflected beams diverge, creating two weaker flashes (Figure 11O). Such variation reduces iridescence and suggests an evolutionary role in optimizing signal visibility for communication and mate attraction.

Beyond fixed coloration, some organisms can dynamically alter their optical properties in response to environmental changes. For example, Sun et al. found that the exocuticle of the beetle, *Dynastes tityus*, exhibits a reversible color change from yellow-green to deep-brown due to different degrees of water absorption within its spongy chitin-protein multilayer structure. This mechanism offers valuable insights for developing photonic materials with controllable iridescence.[341]

3.1.2. Photosynthetic Efficiency (Light Trapping)

In addition to their role in communication, optically relevant biological structures offer additional functionality in increasing selective light absorption and quantum yield—defined as the efficiency with which absorbed photons are converted into emitted photons—particularly in the adaptation to low-light environmental conditions of photosynthetic organisms.[329] Interestingly, Jacobs and colleagues[330] discovered a link between the iridescence in certain *Begonia* leaves and enhanced photosynthetic performance. These plants contain iridoplasts (i.e., specialized chloroplasts featuring photonic crystal structures) and have adapted to the dim light of tropical forest understories. These structures selectively enhance the absorption of light wavelengths that penetrate the forest canopy and increase quantum yield by 5–10% under shaded conditions. While light absorption refers to the amount of light captured by the leaf, quantum yield measures how efficiently that absorbed light is converted into usable energy for photosynthesis. A system may absorb a large amount of light, but if the conversion process is inefficient, the quantum yield remains low. In *Begonia*, both factors are crucial: iridoplasts not only increase the capture of available light but also improve conversion efficiency, offering a dual advantage for survival in low-light environments. Another fascinating example is the silica frustules of diatoms, photosynthetic organisms that originated during the early Jurassic period (150–200 Ma). Their pores span from 50 nm to more than 1 μm and follow a periodic species-specific arrangement that influences how light interacts, making them living photonic crystals.[342,343] These periodic nanostructures can create photonic band gaps, where certain wavelengths of light are absorbed (e.g., the photosynthetically active radiation) and others are either blocked or reflected (UV radiation).[344,345]Thus, these structures allow diatoms to not only manipulate light, but also optimize photosynthesis and protection from harmful radiation. Using rigorous coupled wave analysis (RCWA) and finite-difference time-domain (FDTD) simulations, which are numerical simulation techniques to calculate optical responses of periodic structures, Chen et al.[88] found that the light scattering by the hierarchical frustule structure consisting of micro-/nano-scale periodic pores results in enhanced light absorption in the regions from 380–500 nm and from 650–800 nm (**Figures 12**A,B). This effect is further elucidated in Figure 12, which shows a detailed morphological breakdown of the frustule's pore architecture and FDTD simulations, comparing light absorption for two configurations: Case 1, where light enters from the valve side at cribellum, and Case 2, where it enters from the internal plate (Figures 12C–E). The distinct stacking sequences in each case, along with the simulated electric field distributions at various wavelengths, demonstrate how the multilayered, quasi-photonic crystal structure of the diatom enhances localized field intensities and overall absorption efficiency. Experimental data confirm these predictions, showing increased light absorption when diatom frustules are integrated on top of an active organic thin film layer (Figure 12F). The number and geometric arrangement of nanopores in diatom frustules play a fundamental role in defining their photonic response. A comparative analysis across hundreds of species has revealed an evolutionary trend wherein square lattice configurations (emerging from earlier quasi-ordered morphologies) gave rise to

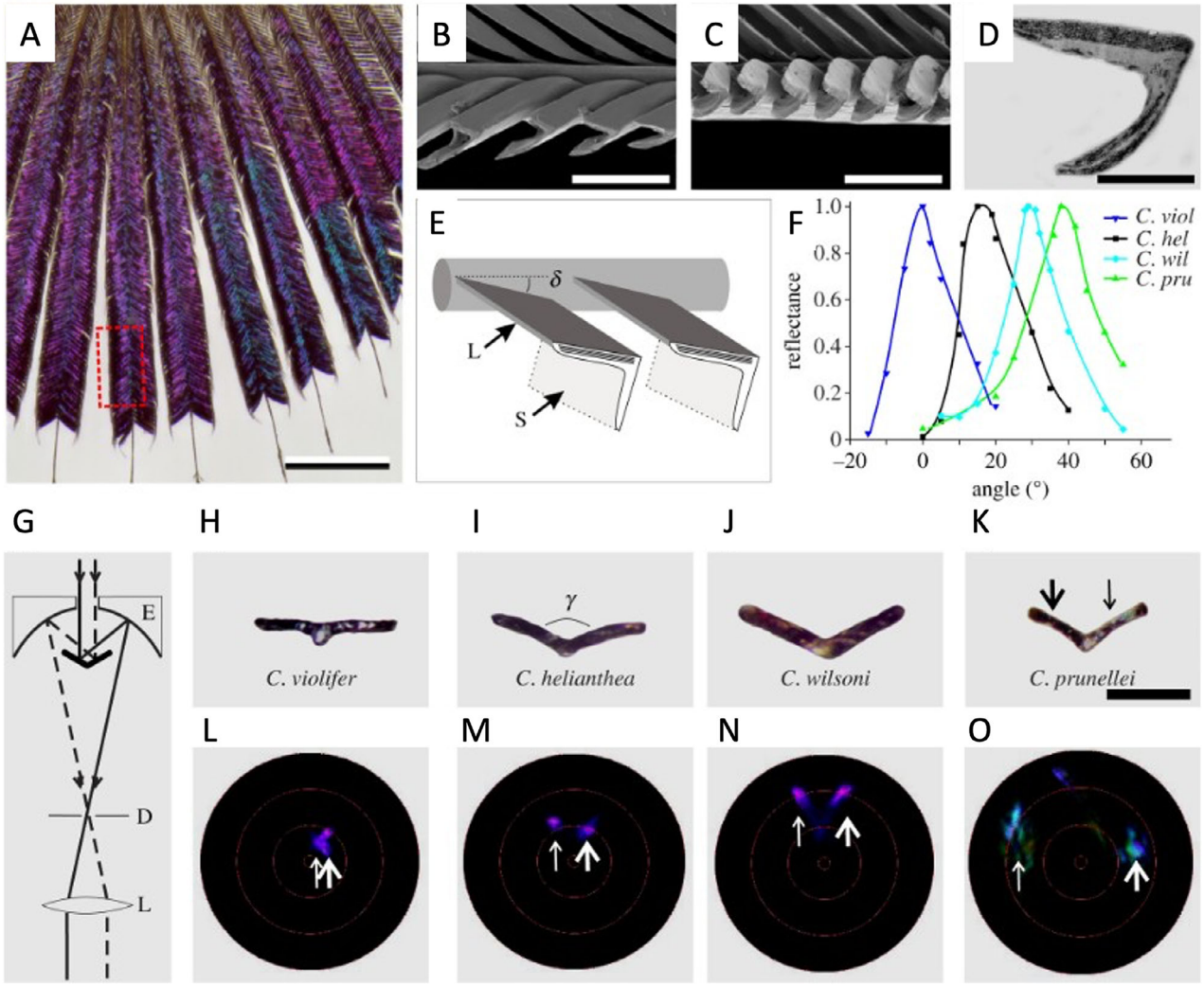

Figure 11. Structural arrangement and light-scattering analysis of Coeligena feather barbules. A) Microscopic image showing the gorget feather of *C. helianthea*. B) SEM image of a longitudinal section of *C. violifer* barbules, corresponding to the dashed area in (A). C) Equivalent section for *C. prunellei*. D) TEM image of a cross-sectioned barbule from *C. helianthea*. E) Schematic representation of a feather barb with two barbules, indicating lamina (L) and side wall (S). The lamina is inclined by an angle δ relative to the barb's axis. F) Angular reflectance spectra (normalized) for barbules from *C. violifer, C. helianthea, C. wilsoni*, and *C. prunellei*. G) Schematic of the scatterometry setup, featuring ellipsoidal mirror (E), diaphragm (D), and lens (L); two parallel rays strike opposite barbule surfaces. H–K) Transverse sections of barbs from different Coeligena species. L–O) Their corresponding scatterograms, with arrows indicating the direction of incident rays as in (G). Red circles in (L–O) denote scattering angles of 5°, 30°, 60°, and 90°. Scale bars: A) 2 mm; B,C) 50 µm; D) 5 µm; H–K) 150 µm. Adapted with permission.[339] Copyright 2021, Royal Society.

hexagonal arrangements, which offer denser packing and possibly enhanced optical functionality (Figure 12G).[346] This progression from structural irregularity to higher order may reflect selective adaptations linked to light harvesting or photoprotection. The degree of periodicity along the *z*-axis (i.e., the direction normal to the frustule plane) was shown to be a key determinant of photonic response (Figures 12Gb,c). Numerical simulations demonstrate that a minimum of 15 regularly spaced pores is required to produce a well-defined photonic stopband, with greater structural order leading to stronger spectral filtering (Figure 12H). These findings not only shed light on the functional evolution of diatom nanostructures but also provide valuable inspiration for the development of synthetic photonic devices with tunable optical properties.

3.1.3. Anti-Reflection

While many organisms rely on structural colors to enhance visibility, other organisms, such as insects, have evolved anti-reflective surfaces on their wings for camouflage and on their eyes to improve their vision in low-light conditions.[331,347] As first demonstrated by Bernhard and Miller[348] on the corneal lenses of nocturnal *Lepidoptera*, specifically on the wings of hawk moths, these surfaces consist of a regular array of nanoscaled conical protuberances which can modify the refractive index at the boundary between the insect's chitinous body (refractive index, *n*, of 1.54) and the surrounding air ($n = 1.0$).[337,348–350] Blagodatski et al.[351] conducted an extensive study of the nipple-like nanostructured surfaces across 23 insect orders, which revealed their fascinating

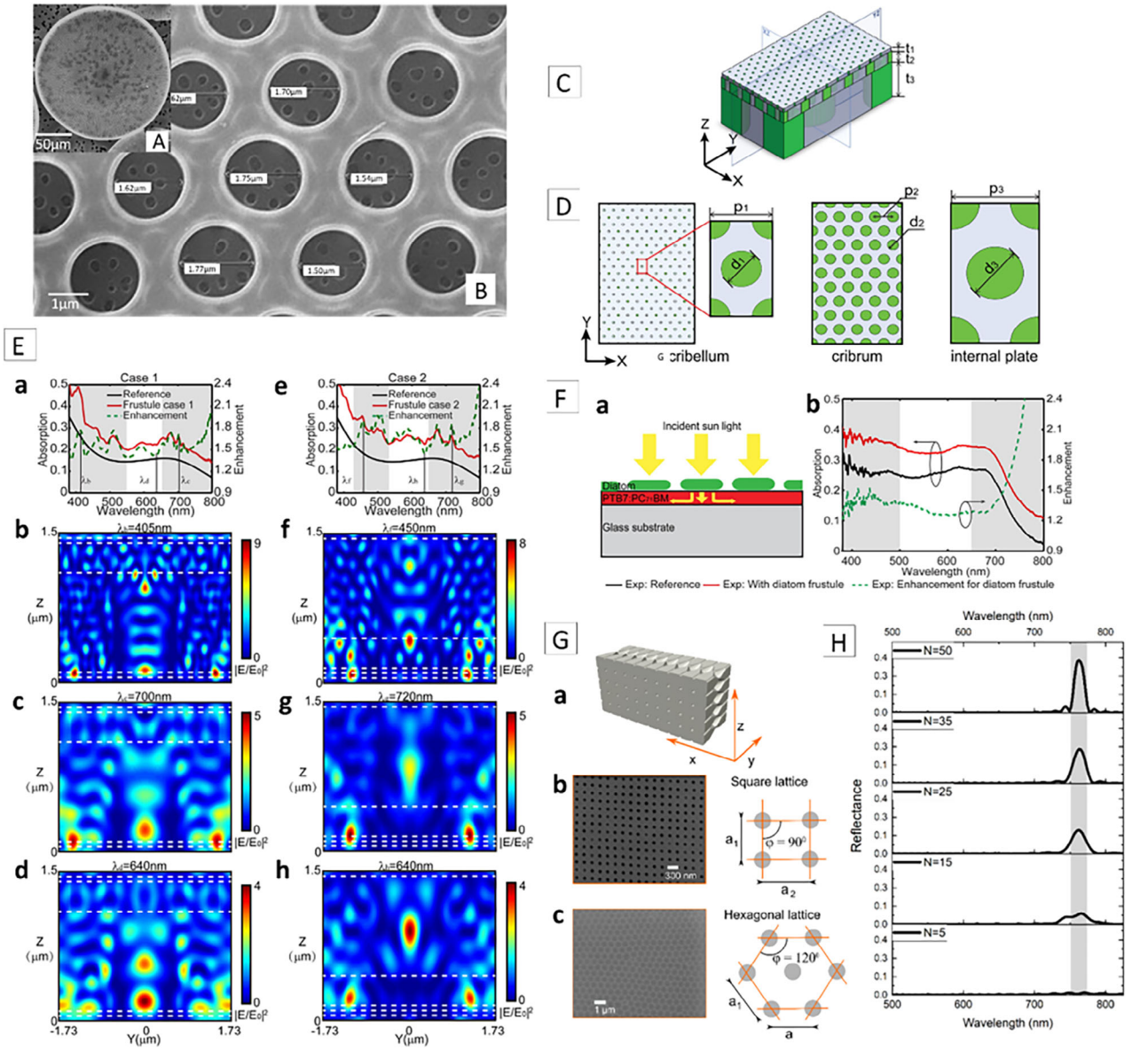

Figure 12. A) SEM Micrograph of the diatom *Coscinodiscus walesii* and B) morphometric details of its pore ultrastructure. A,B) Adapted with permission.[343] Copyright 2009, Elsevier. C) Simplified 3D structure of the unit cell of diatom frustule with a thickness of the three layers: Cribellum $t_1 = 50$ nm, Cribrum $t_2 = 300$ nm, Internal Plate $t_3 = 1000$ nm. D) Left: top view of cribellum, the lattice constant $p_1 = 200$ nm and the hole size $d_1 = 50$ nm. Middle: top view of cribrum, the lattice constant $p_2 = 400$ nm and the hole size $d_2 = 250$ nm. Right: top view of internal plate, the lattice constant $p_3 = 2$ μm and the hole size $d_3 = 1.3$ μm. E) FDTD simulated absorption spectra of the simplified diatom frustule model with the 50 nm thick active layer, case 1 (a), in which the light enters from the valve side, and case 2 (e), in which the light enters from the girdle band side. And normalized electric-field-intensity $|E/E_0|^2$ distribution on the Y-Z plane at λ_b (b), λ_c (c), and λ_d (d) for case 1, λ_f (f), λ_g (g), and λ_h (h) for case 2. Stacking sequence of case 1 (From top to bottom: air, cribellum, cribrum, internal plate, active layer, and substrate), stacking sequence of case 2 (From top to bottom: air, internal plate, cribrum, cribellum, active layer, and substrate). F, a) Schematic representation of a PTB7:PC_{71}BM-based thin film with the diatom frustules on the top layer. F, b) experimental absorption spectrum for the model of planar active layer without diatom frustule on top (black curve) and with diatom frustule (red curve), with the experimetnal absorption enhancement curve for diatom frustule (green dashed curve). C–F) Reproduced with permission.[88] Copyright 2015, Springer Nature. G) 3D model and SEM images showing square and hexagonal lattice arrangements in diatom girdle bands, including a schematic diagram of photonic stopband formation in periodic pore structures. H) Simulated reflectance curves showing the increase in stopband intensity with increasing number of periodic pores along the z-direction. The data highlight how precise control of pore number/geometry directly influences optical performance. Reproduced with permission.[346] Copyright 2025, Spinger Nature.

diversity and functionality, as unique adaptations to their respective environments. Using atomic force microscopy, they characterized an extraordinary variety of corneal nanocoatings that effectively minimize light reflection. Remarkably, these nanostructures exhibit the full spectrum of Turing patterns—geometric formations driven by reaction-diffusion processes that underpin many biological and physicochemical phenomena—that reveal both convergent and divergent evolution. The insights gained from this study have profound implications for understanding the molecular origin, their evolutionary diversification, and their replication in biomimetic material design. The detailed modeling of these Turing-patterned nanocoatings provides a parametric framework for engineering novel materials with customizable surface functionalities that have potential applications in optics, energy-efficient coatings, and stealth technologies.

3.2. Biologically Inspired Materials

The vast array of structural colors observed in the biological realm is the result of millions of years of evolution, offering valuable functional strategies for biomimetic or even paleomimetic applications.[328,352] Notably, color-producing structures have also been discovered in extinct species.[112,353] Drawing from these natural examples, researchers have synthesized photonic nanomaterials to mimic their optical functionalities.[350] These materials are finding applications as nontoxic colorants, iridescent devices, and engineered anti-reflective surfaces.

3.2.1. Structural Color

The fabrication of synthetic *Morpho*-like structures has enabled the development of materials with vibrant structural colors that are more sustainable, durable, and fade-resistant than conventional dyes and pigments. Currently, adding color to human-made products and fabrics typically relies on dyes and paints (i.e., processes that contribute to ≈20% of global wastewater). In contrast, structurally colored materials offer an eco-friendly alternative, with promising applications across industries such as paint, printing, and textiles.[350,354–357] In this regard, the company *Cypris Materials* has developed structural color coatings composed of block copolymers that self-assemble into photonic crystals when dried. These form periodic microstructures that can reflect UV, visible, and infrared light, serving as coatings for various sectors like automotive, construction, and packaging.[358]

An artificial analogue of the beetle *T. rothschildi varians* has also been fabricated by drilling submicron-sized holes in a SiO/SiGe regular multilayer structure (Bragg reflector), which exhibits similar color behavior to its biological counterpart, such as non-specularity and slightly angle-dependent reflectance.[87] As shown in **Figures 13**A,B, the beetle displays vivid structural colors (violet, green, and orange; Figure 13C) across different regions of the elytra, with corresponding reflectance spectra and well-defined photonic crystal periodicities observed in cross-sectional micrographs. To mimic these features, bio-inspired nanoarchitectures with both random (Figure 13D) and regular (Figure 13E) hole patterns were fabricated in a multilayered (SiO/SiGe) system, which successfully replicated the iridescence and angular color shifts (Figure 13F). This confirms that the hierarchical photonic design observed in the beetle can be effectively translated into engineered materials with tunable optical properties.

Sophisticated optical devices with nanoarchitectures similar to those found in insects can also be applied in anti-counterfeiting industry, in which the bio-inspired pattern can be read only by specialized detectors. For instance, inspired by the polarization effects found in insect wing scales, Poncelet et al.[359] replicated the bio-optical features for anti-counterfeiting applications. In particular, using photolithography and wet etching processes, they created cylindrical (C-grooves), and triangular (V-grooves) grooves, respectively, which are inspired by the scales of *Papilio blumei* and *Suneve coronata*. The multilayer coating was produced through plasma-enhanced atomic layer deposition, involving alternating deposition of titanium oxide (TiO_2) and aluminum oxide (Al_2O_3). Analyses showed that V-grooves produce stronger polarization contrast with a specular reflection spectrum, while C-grooves exhibit a more dispersive reflection spectrum with lower polarization. Both structures also display unique optical effects, such as diffraction and color contrast in polarized light, enhancing their potential for anti-counterfeiting applications.

3.2.2. Light Trapping and Anti-Reflection

Solar radiation offers one of the most abundant renewable energy sources, with thin-film solar cells emerging as a promising low-cost solution for solar energy conversion. However, their efficiency is limited by the mismatch between light absorption and carrier transport lengths. To overcome this, advanced light-trapping strategies have been developed using nanostructures like photonic crystals, triangular-pyramid gratings, and plasmonic nanostructures.[88,360,361] Yet, fabricating these subwavelength structures remains costly and complex. Nature, however, provides elegant and efficient alternatives. As previously mentioned, organisms demonstrate remarkable light-harvesting capabilities due to their need to optimize the photon capture for photosynthetic processes or improve their vision using anti-reflection mechanisms. Hence, mimicking these biological structures can lead to efficient, low-cost solar cell improvements.

Accordingly, antireflective surfaces mimicking the nanoarchitectures of butterfly scales have been used on Si-based solar cells to reduce light reflection. Researchers discovered that these inspired design structures reduced light reflection from over 35% to under 5%, increasing the short-circuit current by 66%.[362] Using a high-density electron cyclotron resonance plasma etching technique, Huang et al.[363] developed a simple aperiodic array of silicon nanotips (SiNTs) on a 6-inch wafer with subwavelength features that minimize light reflection across a wide range of wavelengths, from ultraviolet to terahertz. Another interesting example is provided by Sun et al., who developed a scalable and cost-effective approach for fabricating antireflective surfaces inspired by the nanostructures of moth-eyes.[89] Using Roll-to-Plate ultraviolet nanoimprint lithography (R2P UV-NIL) on transparent polycarbonate substrates, the authors replicated the sub-wavelength nipple-array structures observed on moth ommatidia (**Figures 14**A–C). These nano-patterns mimic the natural refractive index gradient of moth eyes, which suppress reflections and enhance optical transmission. As illustrated in Figure 14D,

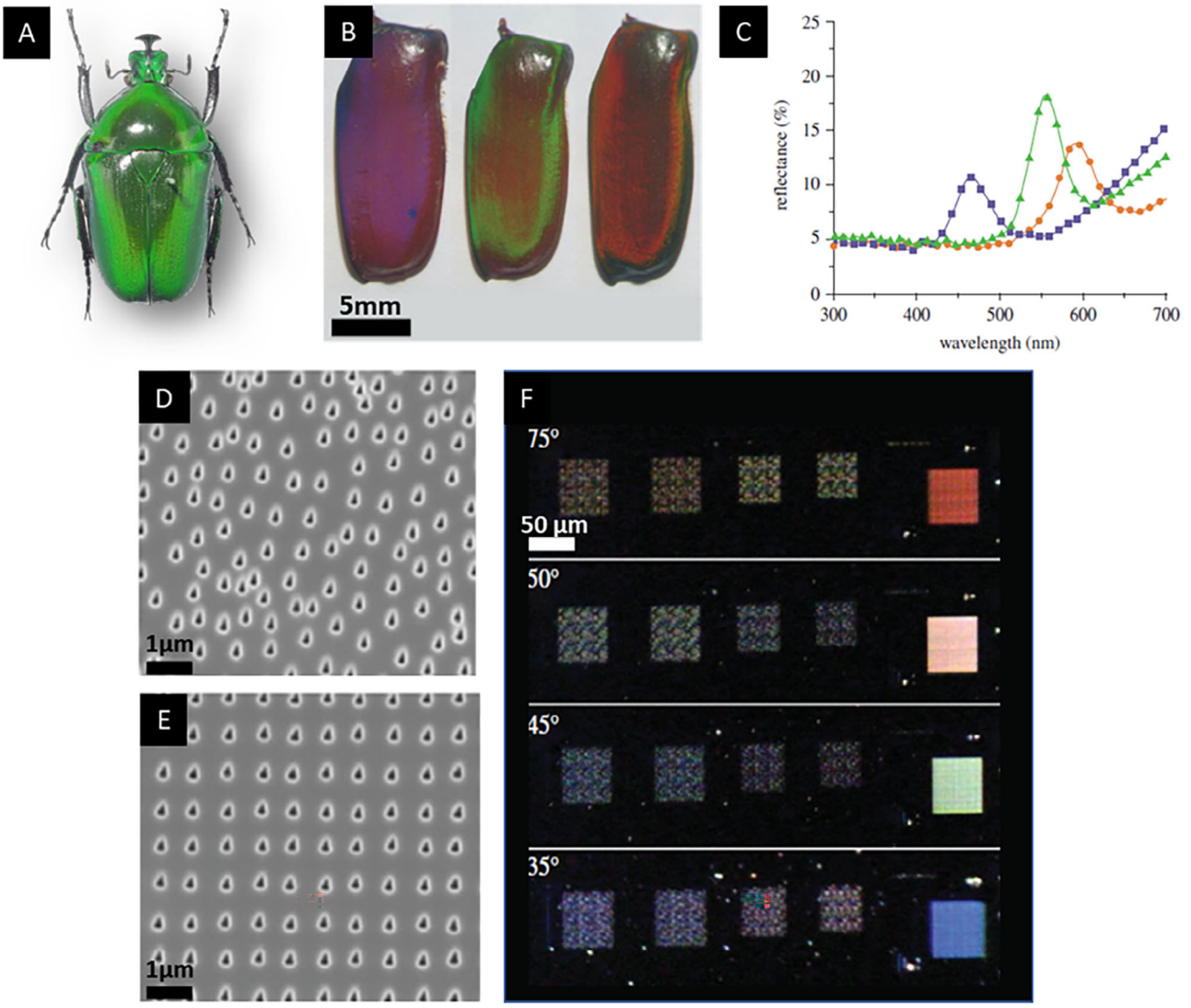

Figure 13. A) *Trigonophorus rothschildi varians* and B) macroscopically observed colors of the elytra: violet, green, and orange. C) Reflectance of the elytra (circle, orange; square, violet; and triangle, green). D) Micrographs of the elytra cross sections with the calculated averaged period p of the one-dimensional photonic crystals and the position of the reflectance maxima λ for normal incidence. E) Micrographs of the nanoarchitected 5X (SiO/SiGe) multilayer with random hole distribution (upper) and regular square hole pattern (bottom) (scale bar 1 µm). F) Photographs showing the same fabricated nanoarchitectures under different illumination angles. Adapted with permission.[87] Copyright 2010, Springer Nature.

different sub-wavelength geometries (i.e., flat, columnar, triangular, and conical) were compared to assess how shape influences refractive index transition. While flat coatings exhibit sharp refractive index contrasts that lead to undesirable reflection, conical and parabolic nanostructures generate a smooth refractive index gradient. This enables more efficient impedance matching between air and the substrate.

The fabrication process was further optimized by controlling two critical parameters: the imprinting force and the viscosity of the UV-curable resin (Figure 14E). Atomic force microscopy characterization demonstrated how increasing the imprinting force from 150 to 350 N led to more pronounced and uniform nanostructures. Additionally, using higher-viscosity resins produced taller and more defined features, which contributed to reflectance reduction down to 1.21% across the visible spectrum and maintained performance at oblique incidence angles up to 50°. Besides antireflective properties, the fabricated surfaces displayed hydrophobicity (contact angles >100°), offering self-cleaning benefits.

Overall, this study highlights the multifunctional potential of moth-eye-inspired nanostructures and their suitability for large-scale implementation in optical devices such as solar panels, touchscreens, and LED displays, marking a significant advance in nature-derived surface engineering. Nonetheless, while natural compound eyes offer an elegant solution for wide-angle vision and anti-reflective performance, their artificial replication presents technical challenges, specifically to the alignment of three-dimensional optical geometries with conventional two-dimensional sensor platforms.[364] Most synthetic compound eyes generate curved focal planes that do not conform to

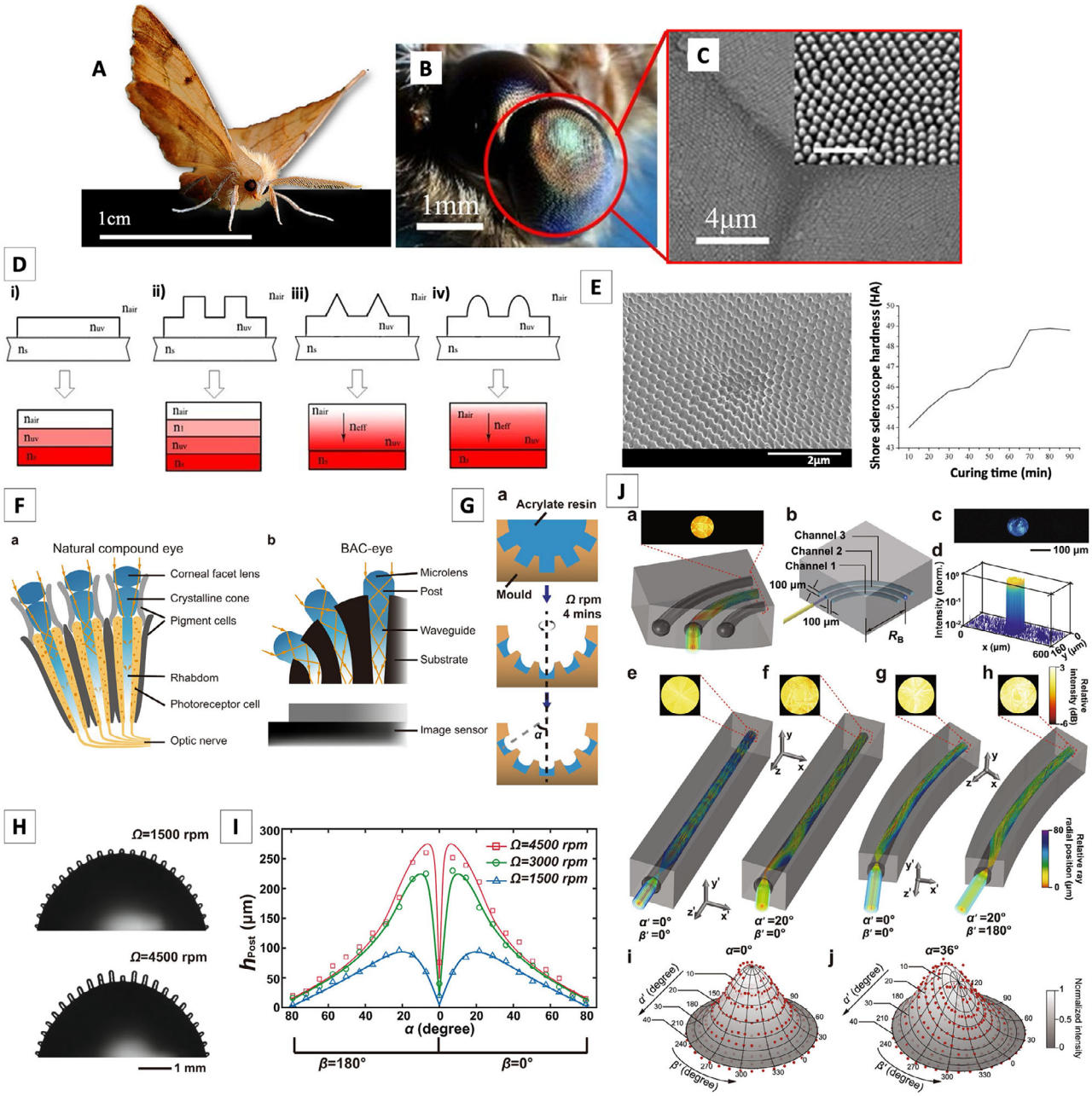

Figure 14. A) Photo of moth, B) the compound eye, and C) the sub-wavelength array structure constituting the ommatidia. D) Schematics of refractive index variations: i) flat UV-curable resin coating, ii) columnar sub-wavelength structure, iii) triangular sub-wavelength structure, and iv) conical sub-wavelength structure. E) Micrograph of the poly(dimethylsiloxane) (PDMS) prepolymer female mold and hardness variation of the mold with different curing times under 110 °C. B–E) Adapted with permission.[89] Copyright 2018, Springer Nature. F, a) Natural moth compound eye with anti-reflective nanostructures and b) schematic of the developed BAC-eye system, where microlenses are optically coupled to a flat base via index-matched waveguides. G) Illustration of the fabrication process involving microfluidic-assisted 3D printing of hemispherical molds. H) Image of a single row of ommatidia formed on the curved surface, where post height variation reflects the spatial distribution of forces during fabrication. I) Experimental and simulated results showing the distribution of post height across the hemispherical surface as a function of rotation rate. J) Cross-sectional image of the BAC-eye substrate showing internal tapered waveguides connecting microlenses to a flat output panel. J, a–j) Optical performance of the fabricated artificial ommatidia. a) Simulated light intensity profiles illustrating crosstalk between adjacent ommatidia with different angular orientations: ($\alpha = 64.8°$, $\beta = 0°$), ($\alpha = 72°$, $\beta = 0°$), and ($\alpha = 79.2°$, $\beta = 0°$). b,c) Experimental setup and output image used to evaluate the spatial separation and light delivery from three curved silicone waveguides. d) Quantified light distribution at the output facet. e–h) Ray tracing simulations in ommatidia with orientations of e,f) ($\alpha = 0°$, $\beta = 0°$) and g,h) ($\alpha = 36°$, $\beta = 0°$) for light incident at different angles, demonstrating how orientation modulates intensity at the waveguide output. i,j) Angular sensitivity functions of the ommatidia with orientations of ($\alpha = 0°$, $\beta = 0°$) and ($\alpha = 36°$, $\beta = 0°$) derived from both experimental data (red points) and Gaussian fitting (grey surface), indicating directional optical response. Together, these data demonstrate how precise control of nanostructure geometry and optical alignment enables the fabrication of scalable, high-performance, bioinspired imaging systems. F–J) Adapted with permission.[364] Copyright 2021, Springer Nature.

flat commercial detectors, thereby requiring complex image correction algorithms or multiple sensor arrays. To overcome this incompatibility, Dai et al.[364] developed a biomimetic apposition compound eye (BAC-eye) system taking inspiration from the natural compound eye (Figures 14Fa,b). The fabrication process relies on a microfluidic-assisted molding technique, a key innovation that enables the precise formation of microlenses directly on a hemispherical substrate (Figure 14G). Specifically, a 3D-printed mold patterned with cylindrical microcavities is filled with a liquid resin, which, under rotational motion, self-forms concave lens shapes through surface tension effects. After UV curing, these lens cavities are replicated onto a polymer substrate. The resulting structure incorporates tapered, refractive index-matched waveguides that connect each microlens on the curved surface to a corresponding output point on a flat base. This fabrication approach enables spatial control over lens height and geometry, as illustrated by both experimental imaging and simulations of height distribution across the hemispherical surface at varying rotation speeds (Figures 14H,I). These variations in microlens curvature directly affect the focal properties and alignment with underlying waveguides, ultimately influencing the imaging fidelity of the device. To assess the optical functionality of the fabricated ommatidia, Dai et al.[364] conducted a combined simulation and experimental analysis of light propagation through the curved waveguides made within the photosensitive polymer mixed with 1500 µg mL^{-1} solvent dye. Simulations revealed how the angular orientation of the ommatidia modulates optical crosstalk and light intensity profiles at the output (Figure 14Ja), while a custom three-channel setup (Figures 14Jb,c) confirmed the directional light transmission and separation achieved by the BAC-eye. The recorded intensity distribution (Figure 14Jd) demonstrated a strong correlation with simulated patterns, validating the optical alignment strategy. Further ray-tracing studies across different incident angles and ommatidial orientations of (e, f) ($\alpha = 0°$, $\beta = 0°$) and (g, h) ($\alpha = 36°$, $\beta = 0°$) revealed how precise spatial design minimizes inter-channel interference and enhances angular resolution (Figures 14Je–h). Finally, the angular sensitivity functions (Figures 14Ji–j), derived from both experimental data and Gaussian fitting, quantify the directional selectivity of each ommatidium.

The synthesis of these biomimetic materials typically involves advanced techniques, such as soft lithography, nanoimprinting, focused-ion-beam, or chemical-evaporation-deposition.[82,359] These methods enable the precise fabrication of periodic nanostructures on a substrate, resulting in synthesized materials with optical properties comparable to those of the natural systems.[82,331,350,365] Each of these techniques presents distinct advantages and limitations depending on the target resolution, scalability, material compatibility, and fabrication cost. Soft lithography and nanoimprinting, are relatively suitable for large-area replication.[366] Among these fabrication methods, the direct use of biological materials as substrates or templates has emerged as a particularly powerful strategy for faithfully replicating natural hierarchical micro- and nanostructures.[82,367] By using natural surfaces directly as a mold or deposition scaffolds, this method enables the retention of structural intricacies that are otherwise extremely challenging to engineer synthetically.

A compelling example of this biomimetic fabrication is provided by Huang et al.[362], who replicated the fine structure of *Morpho peleides* butterfly wing scales. With the wing itself as a substrate, the team used atomic layer deposition (ALD) to build a coating of amorphous alumina on top of the delicate organic structure, reacting precursors ($Al(CH_3)_3$ and H_2O) at a mild temperature (100 °C). Thickness was controlled by varying ALD deposition cycles, which added a 1 Å layer per cycle, and the reflected color of the wing shifted as the coating grew from 10 to 40 nm. The coatings were subsequently annealed (800 °C for 3 h in air) to remove the underlying organic template and crystallize the alumina to improve physical robustness. This inverse replica preserved the wing's nanometer-scale structures, and reflection peaks in the violet/blue range were observed in optical micrographs and confirmed by UV–vis Spectroscopy for both the replica and wing. Interestingly, the alumina replicas demonstrated functionalities as waveguides and beam splitters, presenting a more affordable and reproducible alternative to sophisticated photonic integrated circuit production compared to conventional lithography methods.[363,368] Another example is the direct use of cicada wings (*Megapomponia intermedia*) to fabricate multifunctional nanostructured surfaces through silica deposition, followed by chemical etching and replication using polymethyl methacrylate (PMMA).[369]

The key advantage of these biological template techniques is the ability to reproduce complex architectures with minimal design or computational input. However, it is constrained by the fragility of biological templates, sensitivity to thermal and chemical treatments, and the difficulty of template removal without damaging the resulting structure. Additionally, reproducibility and scalability remain significant challenges when working with natural variability in biological specimens,[366] which will be discussed in the final section of this review.

Alternative biologically based methods involve cell-culture techniques and bio-engineering.[350] Recent works have focused on the cell-culture of butterfly scales. Cultured scales can be embedded in polymeric materials or paints or even applied in optical gas sensors, providing different optical responses to different vapors.[370] Other examples can be found in the direct use of diatoms or modified versions to create photonic devices.[350,371] Other researchers used in vitro assembly of *Wiseana* iridescent virus to produce iridescent films with structural colors more vivid than those seen in insects.[350,372] While these biologically driven fabrication methods are highly promising in terms of sustainability, low environmental impact, and offer the possibility for bottom-up self-assembly, they still face considerable challenges related to scalability, control over uniformity, and integration with current manufacturing processes. Standardization, long-term stability, and large-area production remain critical barriers to their widespread application in commercial photonics.

4. Thermal Materials

4.1. Biological System Designs

Thermal regulation is a fundamental factor in the survival of organisms, but also critical in many engineered systems. The development of thermal regulation technologies must be both nuanced and powerful to advance science and reduce energy consumption.[365] Conventional materials like metals, polymers, and oxides have inherent limitations, such as thermal expansion

in metals, thermal instability in polymers, and low thermal conductivity in oxides, which make it challenging to develop efficient thermal regulation materials. Over millions of years, nature has adapted to diverse environments, including extreme thermal conditions found in polar regions and deserts, through efficient thermal regulation via absorption, reflection, scattering,[373] and emission.[374] Some of the most precise thermal regulation systems are found in nature, particularly within the microstructures of organisms' surfaces. By emulating the strategies of animals that thrive in extreme cold[375] or heat,[376] we can develop robust thermal insulating materials that incorporate features such as energy storage and transformation, passive radiative cooling, solar steam generation, radiative heat dissipation, and infrared stealth or detection.[377,378]

Solar radiation serves as the primary energy source for the Earth's surface and living organisms. Effective utilization of this energy is essential for survival, whether by retaining warmth in glacial regions, maintaining cooling in deserts, or dynamically adjusting in response to temperature fluctuations in the surrounding environment.[379] It is known that thermal radiation plays a significant role in temperature regulation during solar exposure for heat exchange. Controlling temperature and surface emissivity are two key approaches to managing thermal radiation energy in both biological and engineering systems. The modes of thermal transport, including convection, conduction, and radiation, can theoretically be engineered by adjusting their nano-, micro-, and macro-structures. This structural control allows for the precise tuning of their emissivity, reflectivity, and absorptivity within specific electromagnetic ranges. Consequently, understanding the role of an organism's ultrastructure in thermal response is essential when selecting and designing materials for customized performance in practical applications. For example, the hollow and crimped hair structure, along with the thick fat and fur of cold-adapted animals such as polar bears, Tibetan antelopes, and yaks, effectively absorb and reflect the infrared radiation emitted from their bodies, helping them retain warmth in extremely cold environments.[380] Silver ants can regulate their body temperature in the scorching desert by leveraging the efficient interaction between their triangular hairs and electromagnetic waves (**Figures 15a–c**). This adaptation enhances reflectivity in the visible to near-infrared range while increasing emissivity in the mid-infrared band.[374] Therefore, it is essential to understand the relationship between the ultrastructures of organisms and their thermal response behaviors to guide the design and manufacturing of materials for engineering applications such as thermal camouflage, energy-efficient building materials, and heat management in electronics.

4.1.1. Insulating

Animals that thrive in extremely cold environments have evolved specialized fur to survive. For instance, polar bears exhibit a remarkable ability to regulate their body temperature in the Arctic's extreme cold, primarily due to the insulating properties of thick layers of fat and a unique fur design.[358] Their dense, double-layered fur coat is comprised of long, oily guard hairs and a thick undercoat. The water-repellent nature of these guard hairs prevents moisture from penetrating to the inner layers, thus maintaining their insulating effectiveness. These medullated (hollow) guard hairs (≈200 µm diameter and 15–20 µm pore diameter) are also translucent, allowing solar radiation to reach the polar bear's dark skin, underneath the thick fur, maximizing the absorption of heat.[359] Additionally, their structure scatters light, contributing to their white camouflage. The size and spacing of internal nanostructures fall within the regimes of both Mie and Rayleigh scattering, producing broad-spectrum scattering of visible light and resulting in a white appearance. Moreover, the hairs contain little to no pigment, minimizing absorption and allowing most incident light to be reflected or scattered, enhancing the bear's ability to blend into snowy environments. Beneath this protective outer layer, the dense, woolly undercoat forms an effective barrier, trapping a layer of warm air directly against the bear's body.[357] Further enhancing this insulation is a substantial layer of blubber, a thick deposit of fat located directly beneath the skin. Blubber functions as an effective thermal insulator primarily due to the inherently low thermal conductivity of lipids, which conduct heat far less efficiently than water or muscle tissue. Its high concentration of triglycerides and low water content reduce heat transfer. In addition, the microstructure of blubber, composed of adipocytes embedded in a collagen-rich extracellular matrix, creates a heterogeneous, disordered environment that scatters phonons and disrupts coherent thermal conduction, similar to the behavior of amorphous solids or foams. This structural complexity further impedes heat flow from the bear's warm core to the cold external environment. Combined with its considerable thickness and the bear's ability to regulate peripheral blood flow, blubber serves as a crucial adaptation for thermal protection, especially in icy waters.

The emperor penguin, the only bird species that breeds during the Antarctic winter, employs a similar insulating strategy to survive extreme conditions, with ambient temperatures dropping as low as −40 °C and wind speeds reaching up to 40 m s^{-1}. This remarkable thermal insulation is largely attributed to the feather surface, which provides over 80% of the total insulation and exhibits high resistance to wind penetration. A closer examination of the ultrastructure of penguin feathers reveals a hierarchically branched architecture: long barbs, with average pore diameters of around 190 nm, extend from the central rachis, and each barb is further composed of finer barbules, which themselves contain nanostructured filaments and porous matrices that trap air at multiple length scales. These nanoscale air pockets and filamentous networks reduce convective and conductive heat loss by limiting air movement and disrupting heat flow pathways. The combined effect of hierarchical porosity, surface roughness, and material heterogeneity results in a multiscale insulation system, in which nanostructured features play a critical role in enhancing thermal performance under harsh Antarctic conditions. These feathers are constructed from β-keratin sheets with interconnected porosity, highlighting the critical role of porosity in adaptive thermal insulation.[380–383] At the molecular level, β-keratin is a hierarchically assembled biopolymer, consisting of extended polypeptide chains stabilized by covalent intra-chain bonding, while the assembly of these chains into higher-order sheet structures is mediated through weaker non-covalent interactions, including hydrogen bonding and van der Waals forces. This multiscale organization results in a material with anisotropic mechanical and thermal properties. The disordered, heteroge-

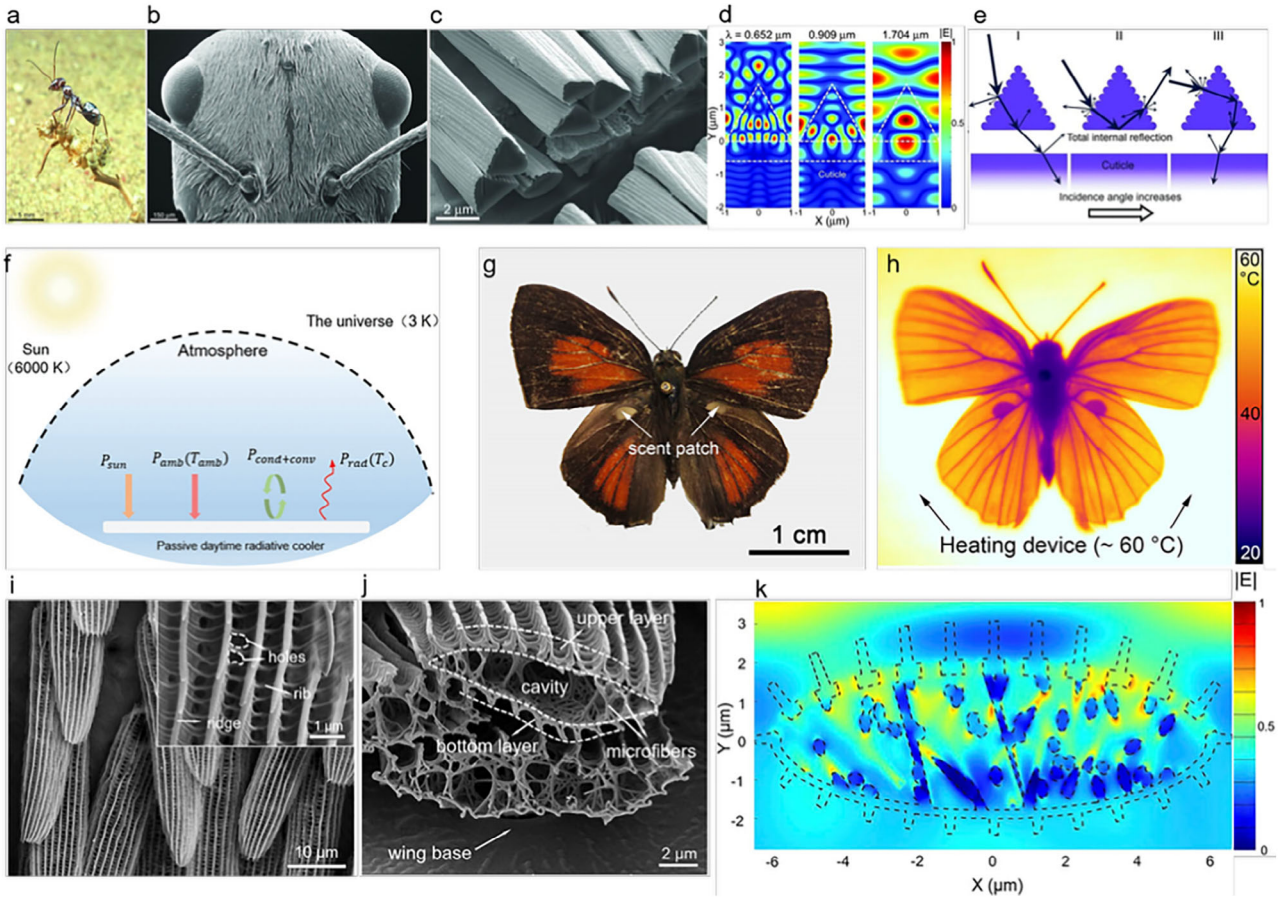

Figure 15. a) Silver ant. b) SEM and c) cross-sectional view of the hairs and d) 2D distribution of a light field around a triangular hair for three exemplary Mie resonances. e) Schematic diagram showing the interaction between visible and NIR light and a hair at different incidence angles. a–e) Adapted with permission.[373] Copyright 2015, AAAS. f) Thermal energy flow in a typical passive daytime radiative cooling system. Reproduced with permission.[378] Copyright 2022, Wiley-VCH. g) Photograph of the dorsal side of the male butterfly. h) IR image of the butterfly above the heating device (set at 60 °C) with the ambient temperature at 25 °C. Top-view (i) and cross-sectional view (j) SEM images of the non-scent patch scales and the scent patch scales on the *Rapala dioetas* hindwing. k) Cross-sectional view of a two-dimensional normalized light field intensity distribution at wavelength = 8 μm inside the simulation model of a scent patch scale. h–k) Adapted with permission.[385] Copyright 2021, AIP Publishing.

neous arrangement of keratin molecules and their bonding interfaces creates significant phonon scattering, impeding coherent thermal transport. Furthermore, the porous structure introduces multiple solid–air interfaces, where acoustic impedance mismatches further disrupt phonon propagation. Together, these factors lead to low thermal conductivity, making β-keratin an effective thermal insulator. When integrated with the feather's microscale and nanoscale porosity, this molecular architecture plays a central role in minimizing heat loss and enabling emperor penguins to maintain core body temperature in extreme polar conditions.

4.1.2. Cooling

For organisms in hot environments, maintaining thermal homeostasis is crucial for survival. Saharan silver ants exemplify the principle of survival of the fittest. Unlike the 1D porous and hollow structure of polar bear hairs, optimizing two-dimensional biomimetic nanostructural parameters (such as geometric configuration and size) can enhance thermal performance and improve cooling efficiency. For example, Wehner et al.[373] reported that these ants maintain their bodies at a temperature lower than that of the desert sand by utilizing a coating of silver colored hairs on their backs and sides (Figures 15a–c). These hairs serve a dual optical-thermal functions: they reflect a broad spectrum of solar radiation while simultaneously enhancing thermal emissivity in the mid-infrared range. The hairs possess a triangular cross-section with corrugated surfaces and are aligned in a uniform orientation across the body. This specific geometry facilitates high reflectance of visible and near-infrared solar radiation through constructive interference and minimized absorption, acting as a biological photonic structure. Any visible light that is absorbed is converted into heat and re-emitted as longer-wavelength infrared radiation. The triangular shape and surface corrugations increase the effective surface area and create a high emissivity in the thermal infrared region (8–12 μm), which corresponds to the atmospheric transparency window. This allows heat to be efficiently radiated away into the sky, even under direct sunlight (Figures 15d,e). Thus, the ant's hairs function not merely as a

reflective shield but as a sophisticated thermal management system, coupling photonic reflection with radiative heat dissipation. This hierarchical structural adaptation enables the ants to forage under extreme midday desert conditions, when surface temperatures can exceed 60 °C, without succumbing to thermal stress. Additionally, the smooth silver surface on the ants' undersides reflects heat rising from the sand. These evolutionary adaptations enable the ants to forage during the hottest parts of the day, when other insects and lizards seek shelter, giving them a unique advantage over their competitors. This capability arises from the corrugated triangular surface of hairs, with ≈220 nm corrugations and a nanoscale air gap that is hundreds of nanometers thick. These provide a barrier between the hair and cuticle, reducing thermal transport via convective processes.

While sunlight is vital for all life on Earth, excessive exposure can cause harmful overheating. The Earth's atmosphere is transparent to infrared (IR) radiation in the 8–13 µm wavelength range, allowing terrestrial emitters to dissipate heat into the cold universe through this atmospheric window. This process enables passive cooling, allowing objects to reach temperatures below the ambient environment (Figure 15f).[378] Conventional cooling methods not only demand substantial energy but also contribute to environmental concerns by emitting greenhouse gases. Alternatively, passive radiative cooling efficiently dissipates heat into the cold universe through thermal radiation without consuming energy. Many biological organisms, primarily composed of proteins, polysaccharides, and minerals, can selectively absorb mid-infrared (MIR) light, exhibiting high MIR emissivity. Additionally, many biological species possess nanostructures that regulate light-matter interactions across the UV, visible, near-infrared (NIR), and MIR ranges. For instance, the triangular cross-section of the aforementioned desert silver ant hairs plays a crucial role in enhancing thermal regulation. During hot summer days, their foraging activities may peak when desert surface temperatures reach 60–70 °C, while their body temperatures range from 48 to 51 °C.[384]

Pores and holes are another key structural adaptation that enhances radiative cooling in organisms. The introduction of air voids disrupts the uniformity of optical properties, enabling the regulation of light-matter interactions. Nanoscale pores scatter visible light, while microscale pores enhance MIR light scattering, effectively modulating MIR emissivity. For example, the hierarchical scent patch region on the wing scales of the butterfly *Rapala dioetas* exhibits enhanced MIR emissivity due to its porous structures. The incident MIR light is scattered at the interfaces of these microfibers, improving passive radiative cooling (Figures 15g–k).[385]

4.1.3. Dynamic Temperature Regulation

In another example of dynamic thermal regulation, mammals with fur use piloerection, a process where arrector pili muscles contract, causing hair to stand erect.[386] This action traps a thicker layer of insulating air close to the skin, effectively reducing heat loss in response to cold environmental temperatures. The degree of insulation can be adjusted dynamically by varying the extent of hair erection, providing a rapid and responsive mechanism for conserving body heat. While less effective in sparsely haired mammals like humans, piloerection is a crucial adaptation for maintaining warmth in many furry species.

Beyond evolving and adapting to survive in either extreme cold or hot environments, most organisms also require a thermostat-like mechanism, as they can only function within a narrow temperature range. Therefore, dynamic thermoregulation is crucial for their survival. In nature, opportunities for developing bio-inspired thermal regulation are found in organisms that can rapidly change color to blend into their surroundings for defense or foraging.[92] For example, cephalopods like squid alter their skin appearance by contracting and expanding chromatophore pigment cells.[387] Although these biological camouflage effects primarily operate in the visible spectrum, they have inspired innovations in adaptive IR camouflage for thermal engineering applications. The squid's dynamic color-changing ability offers a blueprint for creating tunable thermoregulatory materials. Similarly, chameleons can rapidly and intricately change color by dispersing or aggregating pigment-containing organelles within dermal chromatophores. Meanwhile, a deeper layer of cells broadly reflects light, primarily in the near-infrared range, mitigating the thermal effects of intense solar radiation and providing passive thermal protection.[388] Inspired by this, materials that control the roughness or alignment of nanoscale structures can be designed to dynamically modulate their ability to absorb or reflect heat, thereby enhancing heat management under varying conditions.

4.2. Biologically Inspired Materials

The ability to regulate thermal radiation is crucial across various technologies, such as thermal management in electronics, passive radiative cooling systems, infrared stealth and camouflage, thermophotovoltaic energy conversion, and spacecraft thermal control. With the rapid advancement of micro to nano-manufacturing techniques and characterization methods, bio-inspired synthetic materials developed from the investigation of these organisms have demonstrated promising applications in thermal engineering. The representative materials are described with emphasis on the relationship between the structural features and the corresponding thermoregulation functions. In addition, the breadth in materials selection—metals, ceramics, polymers, composites, and even biological materials—offers the ability to target a wide array of commercial and defense applications such as aerospace, electronics, housing, etc. This diversity in material selection is particularly valuable for tailoring thermal, mechanical, and optical properties to meet application-specific requirements. At the same time, a number of synthesis methods are available or are being developed to engineer these nanostructured materials. These include, for example, freeze-spinning/casting,[389,390] 3D printing,[391] self-assembly,[392] as well as utilizing natural biomaterials either by preserving their structures or modifying them through carbonization.[393]

4.2.1. Insulating

Bio-inspired materials that replicate natural structures, such as polar bear fur, provide lightweight, high-efficiency thermal

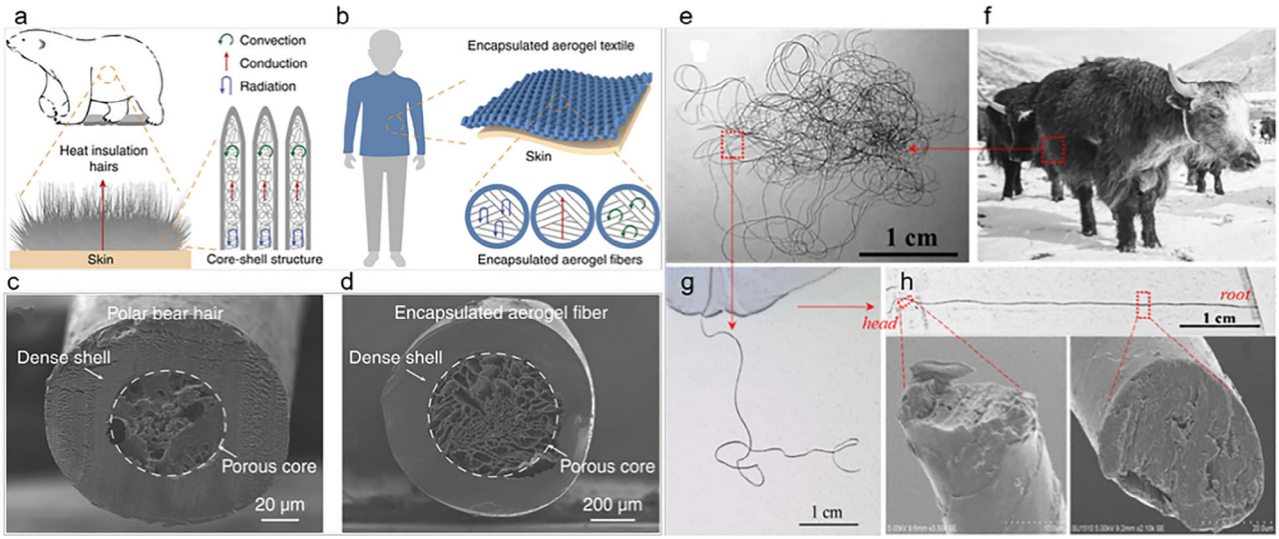

Figure 16. Schematic of thermal insulation in a) polar bear hairs and b) encapsulated aerogel fibers. SEM images of c) a polar bear hair and d) encapsulated aerogel fibers. a–d) Adapted with permission.[380] Copyright 2023, AAAS. e) Yak on the Tibetan Plateau (>4000 m), f) raw yak hairs with guard and down hairs, g) naturally crimped yak hair, h) stretched yak hair showing extended length. e–h) Adapted with permission.[90] Copyright 2019, Elsevier B.V.

insulation, making them ideal for cold environments and applications like thermal clothing or building insulation. In contrast, conventional materials like foams also offer thermal insulation but are often flammable and can emit toxic gases when subjected to high temperatures. Polar bear hairs feature a porous core and dense shell structure that minimizes heat loss. Replicating these design characteristics and selecting from a broad base of materials (e.g., polymers, ceramics, natural materials) can lead to structures with extremely low thermal conductivity for practical thermal insulation applications. Inspired by the nanostructure of the polar bear hair, a natural radiative-cooling fiber, Qiu et al. developed a 2D Ag/cellulose/carbon nanotube (CNT) laminated nanofiber membrane that combines sunlight absorption and thermal radiation reflection.[383] Maintaining outdoor thermal comfort in cold environments requires maximizing heat gain while minimizing heat loss, as heat exchange between the human body and the surroundings is complex. The CNT layer, with its nanoscale tubes, exhibits broadband solar absorption due to several intrinsic optical and electronic properties. First, the high aspect ratio and quasi-one-dimensional structure of CNTs enable strong light-matter interaction through multiple scattering and absorption events across a broad spectral range, from ultraviolet to near-infrared. Additionally, the electronic structure of CNTs, characterized by delocalized π-electrons, allows efficient absorption of photons, converting incident solar energy into heat via non-radiative relaxation processes. The presence of defects, tube-tube junctions, and their random orientation within the membrane further enhances light trapping by increasing optical path lengths and reducing reflectance. Together, these factors contribute to the CNT layer's high and broadband solar absorptance, making it effective for solar thermal harvesting. Meanwhile, the Ag layer, with its high carrier density, provides exceptional infrared reflectance. Using a foam finishing process and magnetron sputtering, the researchers achieved high solar absorptivity through the CNT coating and strong infrared reflectivity via the Ag coating. When applied to a skin-simulating heater, the laminated membrane increased the temperature by 2.3 and 2.9 °C compared to CNT/cellulose and cellulose/Ag membrane, respectively, demonstrating that thermal insulation results from the combined effects of the Ag and CNT layer. This synergy enhances radiation-based warming by optimizing solar heat absorption while reducing infrared heat loss. The natural insulation, inspired by the design of fibers that mimic polar bear fur, is now being explored for its potential in human thermal management devices.[394] Additionally, yaks residing in cold plateau regions possess a dense coat of long hair with abundant microcrimps. Each yak hair naturally forms spiral microcrimps.[90] Unlike the hollow structure of polar bear hair, both fine and coarse yak hairs feature solid cross-sections without a porous medulla, emphasizing the essential role of microcrimps in heat retention (**Figure 16**).

4.2.2. Cooling

Inspired by the aforementioned silver ants, Wu et al.[395] fabricated hierarchical, flexible, hair-like photonic structures with a triangular air gap (TAG) using soft nanoimprint lithography with polydimethylsiloxane. The optimal cooling effect was achieved when a TAG-covered glass bottle exhibited a temperature reduction of ≈6.7 °C compared to a bare bottle. Additionally, these flexible films can be applied to wearable devices. For instance, in a watchband, areas covered by TAG showed an average temperature reduction of 4.5 °C compared to uncovered regions (**Figures 17a-c**). Inspired by the *Cyphochilus* beetle (Figures 17d,e), Tso et al.[91] found that its whiteness arises from a network of chitin filaments combined with an interconnected structure of air pockets. This ultrathin structure produces exceptional visual whiteness, primarily due to multiple scattering from the randomly entangled, disordered network of

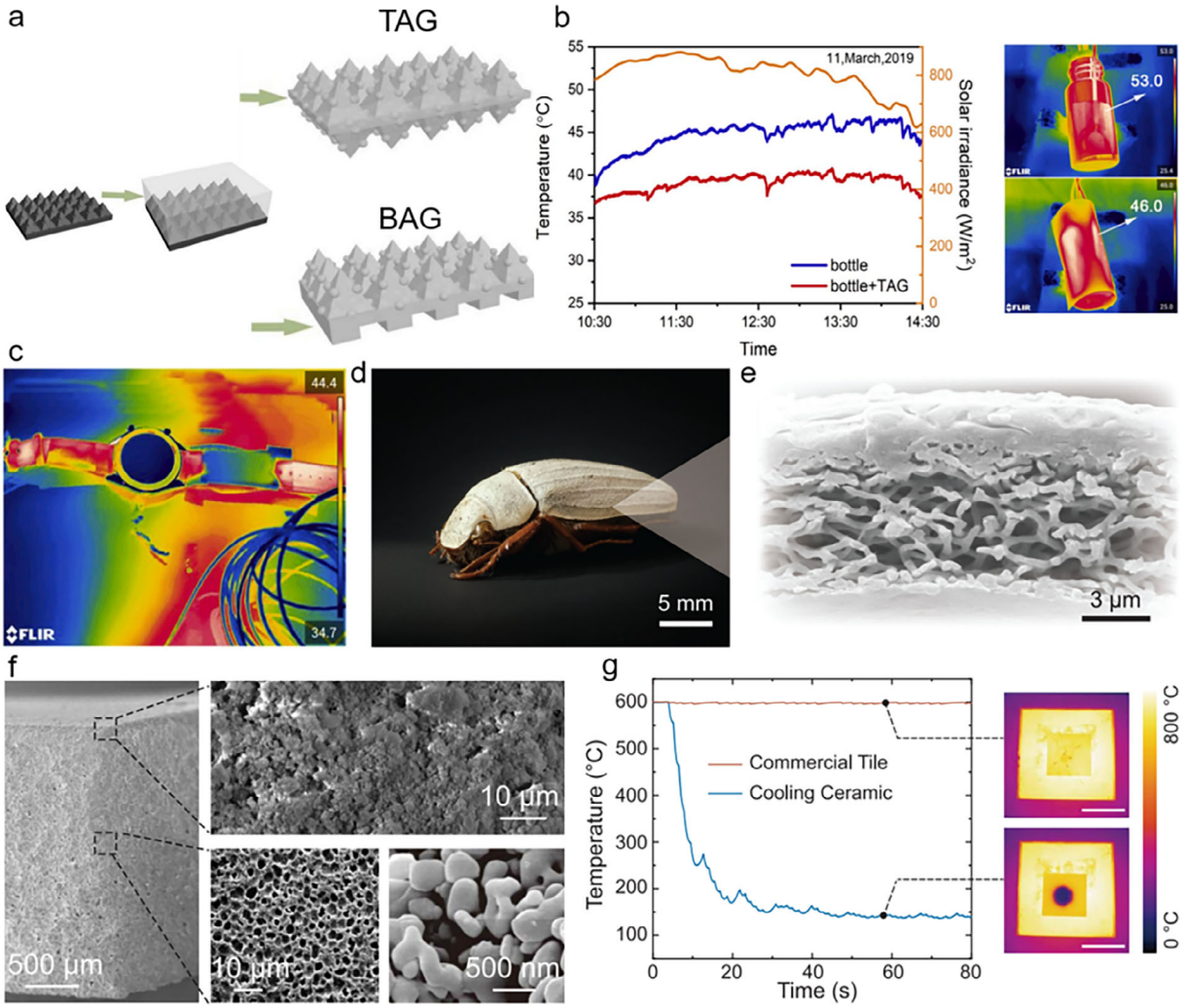

Figure 17. a) Schematic illustration of the preparation of the TAG and BAG samples and flexible films. b) Rooftop measurement and thermal images of the bare bottle and the bottle covered by TAG. c) Thermal image of the watchband areas covered and uncovered by TAG. a–c) Adapted with permission.[395] Copyright 2020, Elsevier B.V. d) The optical and e) cross-sectional SEM image of a *Cyphochilus* scale. f) SEM images of a fabricated cooling ceramic sample showing the hierarchically porous structure. g) Variation in the surface temperature. d–g) Adapted with permission.[91] Copyright 2023, AAAS.

chitin filaments, and shows great potential for applications in efficient daytime passive radiative cooling. Based on the structural designs revealed in these biological materials, they synthesized alumina nanoparticles via phase inversion and sintering to create a cooling ceramic with a densely packed outer layer and numerous internal nanovoids. This cooling ceramic maintained a temperature below ambient air, with an average sub-ambient temperature reduction of 3.8 °C and a maximum reduction of 8.8 °C. Additionally, its effective evaporative cooling performance was demonstrated by a rapid surface temperature drop, while commercial tiles exhibited only negligible temperature variation, as observed through infrared imaging (Figures 17f,g).

4.2.3. Dynamic Thermoregulatory Materials

Thermoregulatory materials were originally designed to control the temperature of spacecraft and satellites, ensuring internal stability by minimizing thermal fluctuations. The dynamic coloration of animal skins provides a wealth of inspiration for IR adjustment systems. Effective IR attenuation is vital for areas including intelligent thermoregulation, adaptive thermal camouflage, and energy-efficient buildings. Drawing inspiration from squid skin, Gorodetsky et al.[396] developed an artificial thermoregulatory platform that combines the static infrared-reflecting design of space blankets with the dynamic color-changing abilities of squid skin. They engineered a composite material made of a soft, stretchable infrared-transparent polymer matrix, overlaid with an array of infrared-reflecting metal domains anchored within the matrix by columnar nanostructures (**Figures 18**a–f). Unlike traditional space blankets, these composite-based sleeves can be actively adjusted to manage heat flux between the wearer and the surrounding environment in real time, allowing for nearly an order of magnitude improvement in controlling local changes in body temperature (Figures 18g,h).

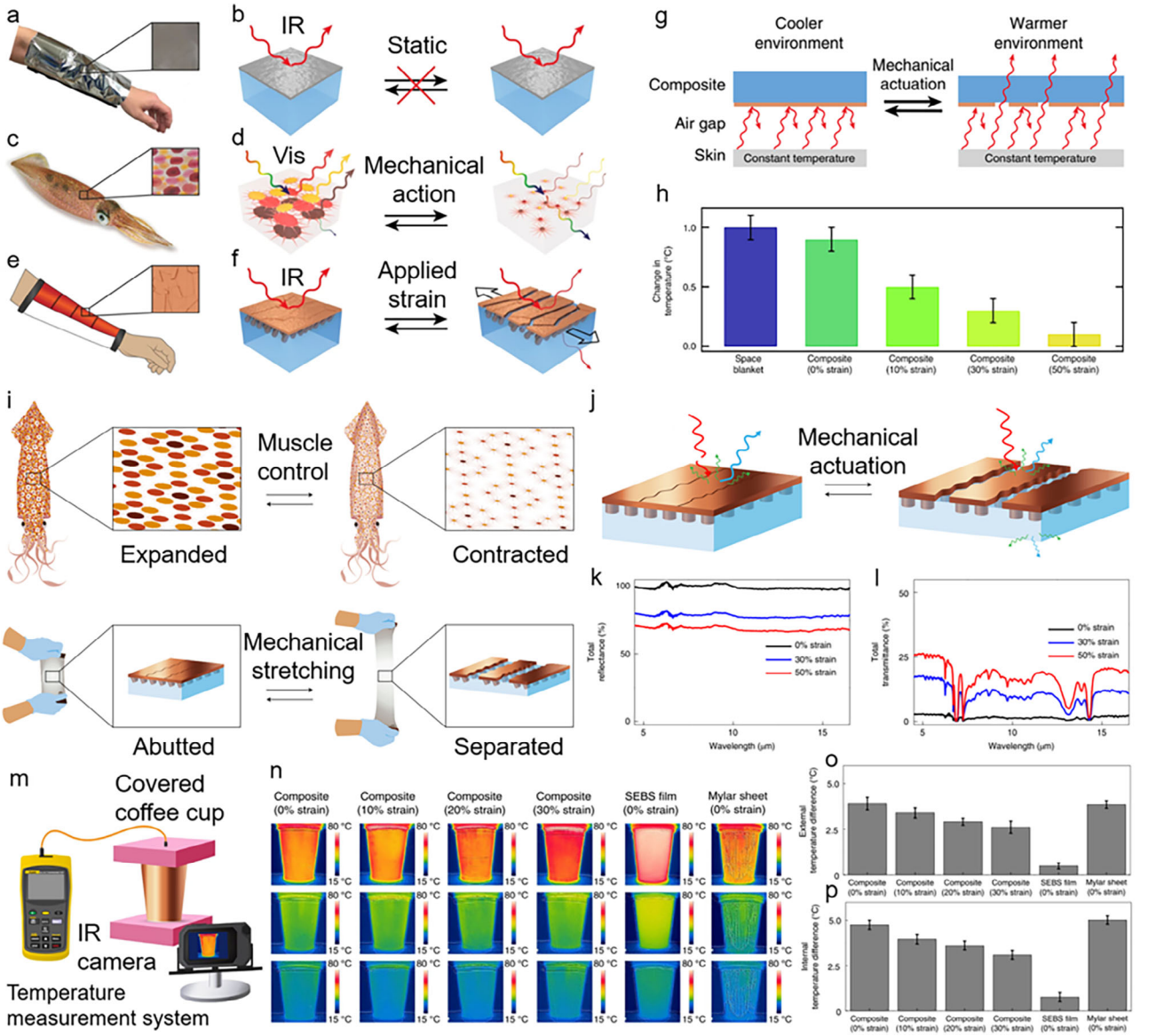

Figure 18. a) Image of a space blanket on a human arm. b) Schematic of the space blanket. c) Image of a squid. d) Schematic of squid skin layer. e) Composite material on arm in wearable form. f) Schematic of the composite. g) Heat flux through the composite without (left) and with (right) actuation. h) Temperature increase of forearms with space blanket- and composite-based sleeves under 0%, 10%, 30%, and 50% strain. a–h) Adapted with permission.[396] Copyright 2019, Springer Nature. i) Squid in expanded (left) and contracted (right) states. j) Strain-induced transition of metal domains from abutted (left) to separated (right). k,l) Reflectance and transmittance spectra of composite under 0%, 30%, and 50% strain. m) Coffee-filled cup covered with composite. n) Thermal camera time-lapse images. o,p) External and internal temperature differences after 90 min for material-covered vs. bare cups. i–p) Adapted with permission.[397] Copyright 2022, Springer Nature.

Later, the same research group drew inspiration from a common squid's unique skin,[398,399] where muscle-controlled chromatophores enable changes in appearance by switching between contracted and expanded states (Figure 18i).[397] They developed reconfigurable nanostructured metallized composite materials that alter their infrared reflectance and transmittance by mechanically stretching, which switches the surface metal domains between abutted and separated states (Figure 18j). To explore how these composite materials interact with mid-infrared light before and after mechanical actuation, they applied strains ranging from 0% to 30% and then to 50%. The resulting spectra indicated a decrease in total reflectance and an increase in total transmittance (Figures 18k,l). Additionally, the thermoregulatory performance was assessed by observing the cooling effects on a hot beverage-filled disposable paper cup. The external and internal temperature differences between the insulated cup and a bare cup stabilized at approximately 2.6 ± 0.3 °C and 3.1 ± 0.2 °C, respectively, after 90 min (Figures 18m–p). These innovative materials could provide a viable technological solution to the cost, performance, and sustainability challenges currently facing the food and beverage packaging industry.

5. Sensing Materials

Highly efficient, sensitive, selective, and cost-effective sensors are needed in many advanced manufacturing sectors. For example, in semiconductor fabs, sensors with ultralow detection limit and rapid response times are needed for precise control of different chemical precursors. For example, in semiconductor fabs, sensors with ultralow detection limit and rapid response times are needed for precise control of different chemical precursors. The increasing demand in automation and construction of smart cities necessitates sensors that can provide real time detection in complex environments.[400] In medicine, biocompatible nanoscopic sensors are needed to detect different biomarkers for the diagnosis of diseases.[401] Although high-performance conventional sensors exist, many still suffer from drawbacks such as complex instrumentation, high cost, substantial energy expenditure, and stringent maintenance requirements. To meet future demands, a new generation of sensors must possess enhanced sensing performance while concurrently being robust, cost-efficient, and easily deployable and integrated. All living systems have engineered intricate sensory strategies that demonstrate remarkable performance and recognition capabilities[402] and thus, offer valuable inspiration for advancing conventional sensing technologies.

5.1. Biological System Designs

Biological sensory systems function similarly to artificial sensors, wherein stimuli are converted into electrical signals via a transduction process, but require far less energy to operate and utilize relatively simple materials (e.g., proteins) as the active sensing elements. Organisms detect different stimuli through a variety of specialized receptors that convert various stimuli into electrical signals via a sensory transduction system, which exhibits remarkable selectivity and sensitivity in the complex environment of nature.[403]

Some of the most important biological sensors, such as chemoreceptors,[404,405] mechanoreceptors,[406–409] thermoreceptors,[410–412] and photoreceptors,[413–415] utilize sophisticated nanostructures resulting from millions of years of evolution. All modalities of organismal sensing rely on biological macromolecules as the fundamental functional unit, among which proteins are the most well-studied. From stimuli recognition to signal transduction, different classes of proteins, such as enzymes,[416,417] antibodies,[418–420] and receptors,[421–424] execute highly specific tasks, with receptor proteins responsible for most external stimuli detection.[425,426] Though our current understanding of proteins is rather superficial, the breadth of existing literature is substantial, thus we refer the readers interested in the field to these outstanding works on proteins.[427–431]

Receptor proteins located on cell membranes are genetically programmed to respond to different stimuli and act as reversible gates of ion channels.[432] When activated, these proteins undergo conformational (structural) changes to allow the flow of ions, which initiates an action potential for a variety of cascading cellular processes.[433] Although the size of receptor proteins varies, they are inherently nanoscopic (largest known VLGR1 receptor protein composed of ≈6300 amino acid residues, measuring ≈4 nm in diameter and ≈180 nm in length).[434,435] Exquisite functional characteristics arise from the small size of receptor proteins. For example, low molecular weight proteins diffuse faster and can be expressed more frequently on cell membranes, leading to greater interaction with a target analyte and consequently, faster response time.[436–438] In general, smaller proteins are less susceptible to steric hindrance and experience greater ligand-binding events,[439] but larger proteins (still at the nanometer scale) possess greater selectivity against specific analytes due to their more complex chemical environment.[440,441]

While receptor proteins form the foundational sensing units, they do not act in isolation. Their capabilities are fully realized when strategically arranged within specialized cellular architectures and ultimately embedded in sensory structures (e.g., sensilla), forming the complex sensory organs.[442] This hierarchical assembly allows for the integration and amplification of individual protein-level responses, converting nanoscale biochemical recognition into organism-level perception and response.[442] This complex sensing then arises from the cooperation among multiple receptors or the involvement of specialized structural elements. For example, scorpions employ arrays of slit receptors to achieve omnidirectional sensitivity and further refine their signal recognition through interfaces with viscoelastic pads.[443,444] While these examples illustrate the effects of receptor integration, the focus of this review is directed towards the nanoscale features and their specific functional roles in sensing, rather than the collective operation of distinct receptor classes.

5.1.1. Chemical Sensing

For many organisms, olfactory information is critical in many aspects, including prey and predator detection, mating, and foraging.[94] As early as the 1970s, researchers found that the male silk moth, *Bombyx mori*, can detect sex pheromones with great sensitivity and selectivity at low concentrations despite having far fewer neurons (10^5–10^6) than that of mammalian olfaction.[94,445] Male silk moths can detect the pheromone bombykol at concentrations as low as 3,000 molecules per ml (in air) at an airspeed of 57 cm/s,[446] showing canine-like sensitivity with significantly fewer olfactory neurons. In these moths, nanoscale chitin-protein complexes are assembled in a hierarchical structure within their antennae, which enables this high level of sensing.[447,448] On the antennal stalk, pairs of antennal side branches extend out to form a bipectinate structure (**Figure 19a**).[94] At an average of 2–3 µm, the olfactory sensilla are the smallest structures of the antenna and can be found on both the antennal stalk and side branches (Figures 19a,b).[449] The sensilla located on the inner side of the side branches act as microscopic sieves for odorant molecules[450,451] while nanoscopic pores (diameter 10–60 nm) and channels on the surface of the sensilla facilitate the diffusion of odor molecules to the sensillum lymph (aqueous fluid).[452–454] The excellent pheromone recognition capabilities of moth antennae are largely attributed to both its hierarchical structure, assembled from nanoscale chitin-protein complexes, and facile binding of pheromone molecules to specific receptor proteins, formed via expression and subsequent folding and anchoring of polypeptides at the nanoscale.[455] The sieve-like antennae effectively trap air, allowing infiltration and diffusion of odorant molecules into the sensillum lymph

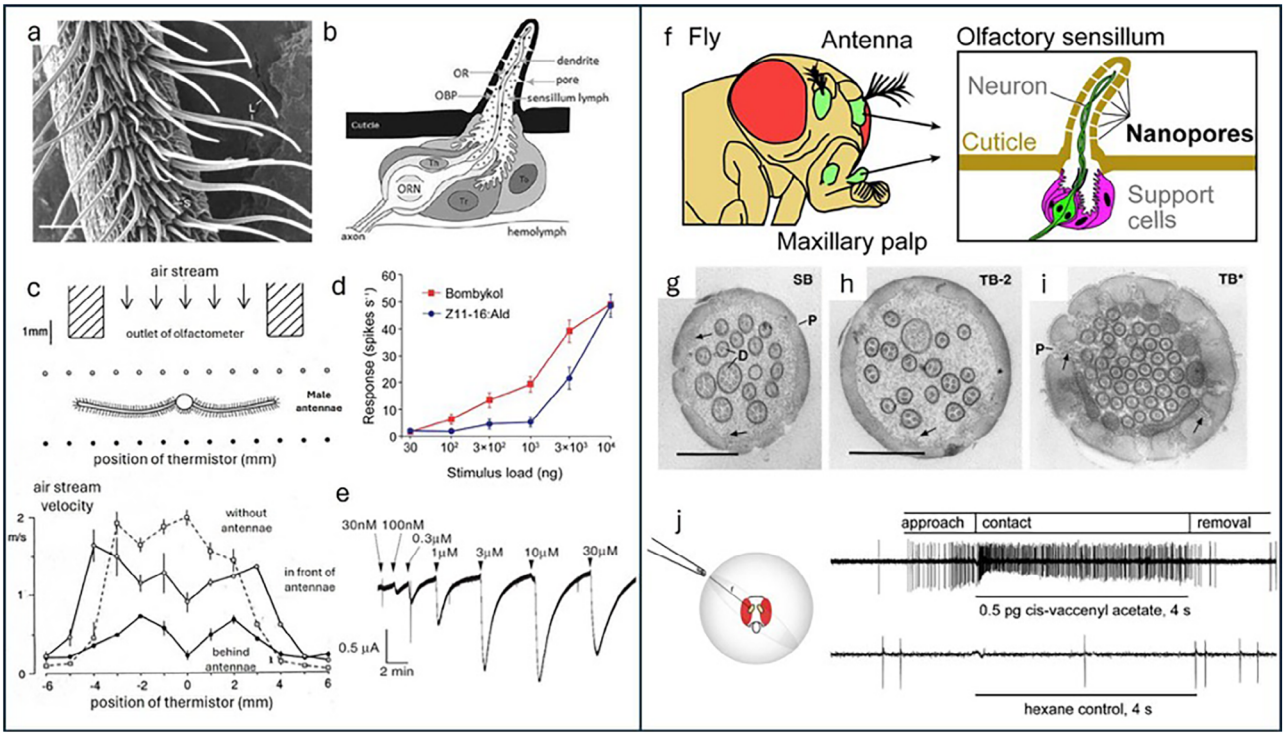

Figure 19. Main olfactory sensory organs of the silk moth, *Bombyx mori*, and the fruit fly, *Drosophila melanogaster*. a) Single antennal branch at higher magnification showing the different sensillum types. Scale bar: 25 μm. Adapted with permission.[460] Copyright 2005, Springer. b) Schematic diagram of an olfactory sensillum showing the detailed configuration of ORNs and accessory cells with respect to cuticular specializations. Adapted with permission.[461] Copyright 2004, Springer. c) Airflow at the antenna of the male moth *Antheraea polyphemus*. Air was blown from a glass tube toward the antenna. Scheme of the glass tube, antenna, and thermistor positions drawn to scale. By means of a thermistor (0.2 mm diameter) the airstream velocity was measured without the antennae (open squares and dashed lines), in front of the antenna (open circles), and behind the antenna (dots). Reproduced with permission.[446] Copyright 2009, Springer. d) Dose-dependent increases in the bombykol (red) or Z11-16:Ald (blue)-induced spike frequency of *BmOR1-GAL4IUAS-PxOR1* male moths. Error bars represent ± SEM ($n = 10$). Adapted with permission.[462] Copyright 2011, PLoS Genet. e) Current trace with application of the indicated concentrations of bombykol. Bombykol was sequentially applied to the same oocytes. Adapted with permission.[463] Copyright 2005, AAAS. f) Schematic representation of *Drosophila* olfactory organ. Adapted with permission.[464] Copyright 2019, Cell Press. g–i) Cross-sections through various subtypes of *sensilla basiconica (sb)* on the antenna of *Drosophila* with pores labeled (P) and arrows indicating pore tubules. SB: small *sb*. TB-2: thin *sb*. TB*: thin *sb* with relatively thick cuticular wall and different internal morphology. Adapted with permission.[465] Copyright 1999, Elsevier. j) Recording responses with a capillary tip containing the stimulus. Left, schematic of stimulus presentation showing a capillary tip containing material; r indicates the radius at which the impulse rate exceeds the spontaneous rate by more than 20 impulses s^{-1}. Right top, response of the T1 neuron to an intermediate dose of *cis*-vaccenyl acetate. Approach of the stimulus to the sensillum, the time of sensillum contact, and stimulus removal are indicated. Right bottom, control stimulus. Adapted with permission.[466] Copyright 2007, Cell Press.

through the nanoscopic pores (Figure 19c). Due to the hydrophobicity of most pheromone molecules, solubilization and transport of pheromone through the sensillum lymph to receptor proteins is facilitated by small soluble proteins (≈15 kDa) called pheromone binding proteins (PBPs), which are highly enriched in the sensillum lymph and exhibit great binding affinity against pheromone molecules.[456–459] Subsequently, binding between pheromone components and receptor proteins activates the chemo-electrical transduction mechanism for pheromone recognition.[94] (Figure 19d shows excellent sensing performance of silk moth receptor proteins). Furthermore, unlike the general perception mechanism involved in odorant recognition from foods and plants, pheromone recognition is selective, wherein sex pheromones are detected by specifically tuned olfactory receptors expressed in male antennae (Figure 19e shows greater sensitivity against pheromone bombykol). With this lock-and-key configuration, the full array of sexual behavior of silk moths can be elicited by a single compound, bombykol.

Chemical sensing organs and mechanisms similar to that of male silk moths can be found in other insects. For example, in the common fruit fly, *Drosophila melanogaster* (Figure 19f), researchers have observed high sensitivity against analyte molecules despite having only ≈1300 olfactory receptor neurons, 62 odorant receptors, and ≈50 glomeruli.[467,468] Although chemical sensing is inherently a chemical process wherein neural signals are generated due to binding of volatile ligands to odorant receptors, the nanoarchitected structure of the sensing organ can greatly enhance sensitivity and response time. Adult fruit flies also possess sensilla similar to the aforementioned silk moths (Figure 19f).[465,468,469] Pores ranging from 50 to 200 nm in diameter can be found on the cuticular sensillum wall[464,469] under which pore tubules can be found, acting as diffusional pathways for odorant molecules to reach the olfactory receptor neuron dendrites within the sensillum lymph space (Figures 19g–i).[468,470] It is widely believed that the nanoporous morphology of the sensillum wall allows for selective diffusion

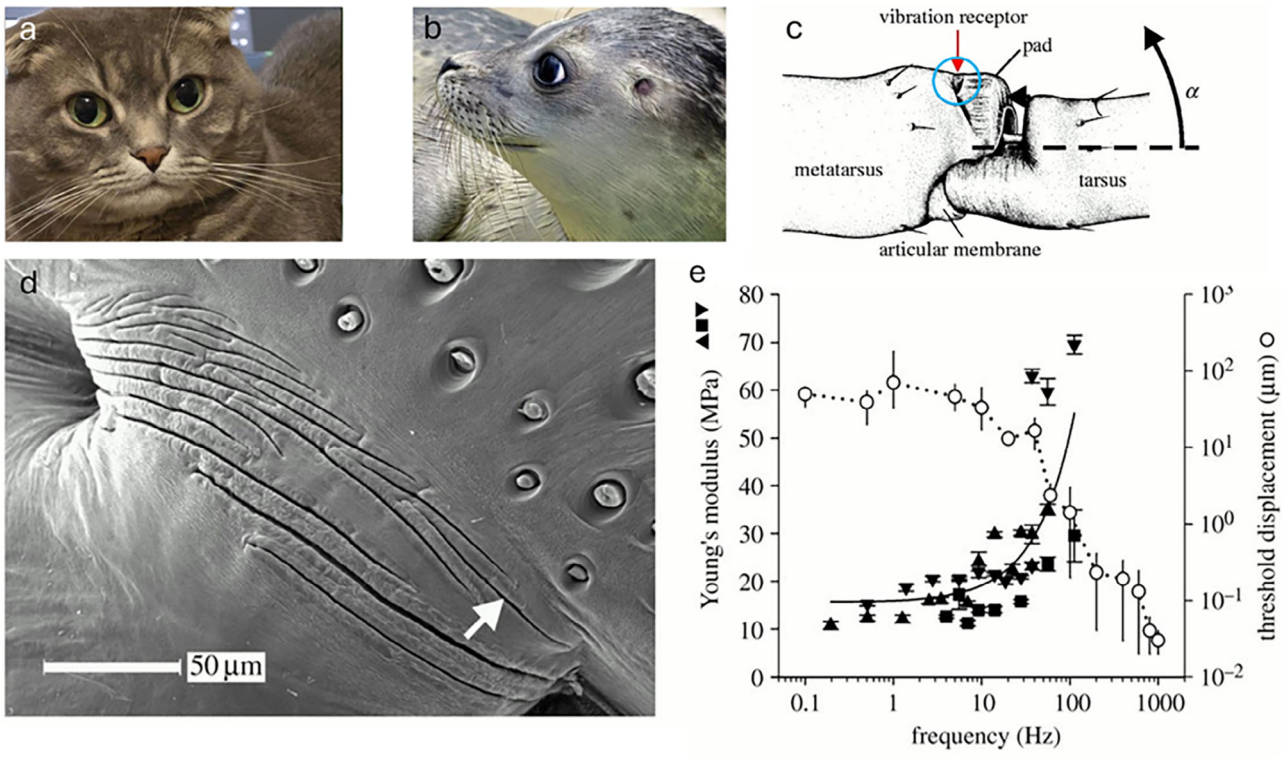

Figure 20. a,b) Biological design features of flexible tactile sensors. b) Adapted with permission.[490] Copyright 2022, MDPI. c) Deflection of tarsus by an angle α exceeding 25° leads to pressure on the pad in front of the vibration receptor. d) SEM micrograph of the metatarsal organ of *C. salei* circled in (c). Arrow indicates nanoslits of the lyriform structure. e) Frequency dependence of Young's modulus (filled symbols) and of sensory thresholds of the lyriform vibration sensor (open circles). c–e) Adapted with permission.[96] Copyright 2007, The Royal Society.

of small odorant molecules (0.5–5 nm in diameter) and prevents airborne particle entry, while simultaneously limiting the loss of inner lymph liquid.[464] Previous studies have also shown the nanostructure of these tubules allows for certain "wicking" mechanisms that promote unidirectional diffusion of odorant molecules towards the olfactory receptors and subsequently generate active potential in the olfactory neuron, thus enhancing sensitivity.[470] Figure 19j shows results from experiments conducted by Naters and Carlson demonstrating the ultra-low detection limit of one sensillum.[466]

5.1.2. Mechanical Sensing

Another sensory mechanism that many organisms utilize is mechanotransduction, in which specialized tactile sensors (or mechanosensors) detect diverse physical stimuli such as pressure,[471–473] vibration,[473,474] tension,[473,475] flow,[473,474] shear,[472,475,476] and sound[477,478] from their environment.[479,480] These mechanosensors convert external mechanical forces from their surroundings into electrical signals. At the molecular level, primary receptor proteins, including force-gated ion channels and mechanically responsive G protein-coupled receptors (GPCRs, with sizes ranging from 300 amino acids to 1100 amino acids, ≈<10 nm in diameter)[481] are responsible for sensing and converting physical forces into cellular signals.[482] In response to mechanical deformation, these mechanoreceptors undergo conformational changes that trigger the opening or closing of ion channels, resulting in rapid biochemical or electrical responses essential for reflexive behavior and information processing.[483,484] This touch-based information gathering is critical in generating neural responses to significantly small external vibrations, which hold a crucial role in survival and adaptation. Many organisms have developed various optimized tactile systems, from whiskers in mammals to slit sensilla in spiders, into highly deformable and hierarchically organized structures, which enhance the creature's fitness within complex environments.[407,474,480,485]

Mammalian vibrissae (**Figures 20**a,b) are a common example of highly specialized tactile sensors that have evolved to provide important mechanosensory information. Whiskers, as the more common name suggests, are hair-like sensors used by animals to "whisk" or oscillate, which enables organisms to effectively navigate and interact with their surroundings, detect prey, and avoid obstacles. Vibrissae, which are long and curved structures, are primarily composed of keratinous molecules that are organized into nanoscale intermediate filaments that are further assembled into macrofibrils, providing both strength and flexibility.[486] Unlike antennae found in arthropods, which contain sensors along the length of the shaft, mammalian vibrissae lack such local sensory elements. Instead, any mechanical movement or deformation experienced by a whisker is transmitted to its base, where it is anchored in a follicle densely packed in a collagen-rich environment with a diverse array of microscale mechanoreceptors

called the follicle-sinus complex (FSC).[487] These mechanoreceptors primarily consist of nerve endings, axon terminals of sensory neurons that innervate the vibrissal follicle, and Merkel cells, epithelial cells responsible for initiating mechanotransduction via the release of neurotransmitters, which then convert any mechanical signals, such as bending or vibration, into neural impulses.[485,488] The sensitivity of whiskers may be influenced by their tapering shape and intrinsic curvature,[485] stiffness gradients,[489] and the viscoelastic properties of keratin,[486] enabling precise detection of environmental textures and shapes. Additionally, functionally graded keratin in elephant whiskers, which transitions from a stiff root to a compliant tip, suggests a direct influence on the frequency, amplitude, and power of mechanical signals felt by mechanoreceptors in the follicle upon physical stimulation.[489] This stiffness gradient affects the number of short-term or dynamic contacts along the length of the whisker, leading to a large increase in vibrational amplitude under equivalent loading compared to homogeneous whiskers.[489] The collective behavior and arrangement of nanoscale alpha-keratin helices, which enable both elastic and viscous responses to stress,[486] allows the whisker to dynamically deform repeatedly producing continuous and precise mechanical sensing.

While biomimetic studies have examined flexible tactile sensing applications inspired by mammalian vibrissae,[406,408] there are still opportunities to further investigate the relationship between ultrastructural features in these biological systems and their use in mechanosensing. Certainly, recent studies[407,409,479] have made progress in addressing this knowledge gap in vibrissal structure-function relationships through advanced structural characterization. Adineh et al.[407] utilized PeakForce Quantitative Nanomechanical Property Mapping (PFQNM) via atomic force microscopy to identify a non-uniform modulus distribution in the whisker cross section. These results, coupled with similarly patterned gradients in chemical properties and finite element simulations, suggest that these heterogeneous distributions likely contribute to the remarkable sensitivity of these tactile sensors.[407] However, further extensive evaluation is required to delineate the underlying relationship between these properties and their functions.

In addition to vibrissae, nano- and micro-scale slits, or "crack" sensors offer alternative design features that show remarkable mechanotransduction capabilities. The large Central American wandering spider, *Cupiennius salei*, is able to detect minute vibrations using micro/nanoslits in their exoskeleton as well as through their hair-like sensilla, making it one of the most vibration-sensitive creatures in the world. Vibrational signals are involved in a myriad of aspects of a spider's life, including prey capture, predator detection, and mating.[474,491] The spider's main vibration-sensing organs are located near the tip of each of its metatarsus legs (Figures 20c,d). When surface vibration is present, the tarsus moves in an upward direction, as indicated by the arrows in Figure 20c, and pushes against the cuticular pad connecting the tarsus and the metatarsus. These pads, called lyriform sensing organs, which consist of nanoscale lamellae composed of chitin-protein fibrils arranged in a twisted plywood structure,[492] are viscoelastic and contain micro/nanoslits (Figure 20d) that result in higher compliance of the otherwise mechanically stiff exoskeleton of the spider.[474] The slits are directly connected to the nervous system of the spider that collects vibrational information.[97] With this type of sensing organs, spiders can detect minute cuticular strains as low as a few microepsilons (10^{-6}), which is equivalent to surface movement as small as 1 nm.[474] It is important to note that besides sensitivity, the lyriform slit sense organ also acts as a high-pass filter that can differentiate between background vibrations and actionable vibrational inputs for the spider (Figure 20e).[96]

5.1.3. Thermal Sensing

The ability to detect changes in the thermal signature of one's environment is vital for survival as it provides signals for a physical response, such as moving away from, or toward, regional fluctuations in temperature in order to gain growth advantages, avoid potential damage, etc.[55] Biological thermal sensing can be largely separated into two categories: i) direct temperature detection and ii) infrared (IR) detection.[379] These functionalities involve different mechanisms and apparati which can detect minute changes in ambient temperature and low-level IR signals.

Strategies to detect direct temperature changes usually involve neurons, the fundamental unit for sensing of somatosensory systems (responsible for the perception of external stimuli). A variety of ion channels, ranging from sub-nanometer to nanometer in diameter, are housed within the lipid bilayers of neurons. They are ubiquitous in virtually all organisms, as their function is essential for the reversible gated flow of ions triggered by external stimuli. For example, invertebrates utilize thermosensitive transient receptor potential ion channels (thermoTRPs) for temperature sensing, which are a major component of their peripheral nervous system.[379,493] The function of different ion channels in the TRP family varies depending on the chemistry of the primary afferents (i.e., nerve fibers), each being able to detect temperature changes in specific ranges. In general, nanoscale receptor proteins expressed in the cutaneous (skin) nerve endings undergo conformational (i.e., structural) changes in response to thermal stimuli, which trigger the on/off flow of cations (Na^+, Ca^{2+}, K^+).[411] This signal is then relayed to the spinal cord and sent to the brain for temperature detection.[494] These ion channels can either detect environmental temperature changes or monitor internal temperature and subsequently trigger cascading physiological responses to maintain homeostasis. The heat-activating mechanism of thermosensitive ion channels remains enigmatic. Proposed mechanisms include dynamic hydrogen-bond interactions and protein denaturation during temperature changes, leading to conformational changes of the receptor protein.[495,496] It is important to note that ion channels are utilized in the detection of other stimuli (i.e., mechanical force sensing (e.g., *Mimosa pudica*),[497] pressure sensing (e.g., *Escherichia coli*),[498] pH sensing (e.g., *Caenorhabditis elegans*),[499] etc.). The versatility of ion channels in stimulus detection and signal transduction is the basis of the complex neural networks and their infinite responsive actions we see in many organisms. Thus, further investigations of these strategies are paramount toward understanding mechanisms of detection and processing of signals, as well as computing the valid responses to external stimuli.[500,501]

Since heat is often transmitted as IR radiation, many organisms have developed excellent radiant heat sensors. Interestingly, organisms such as snakes utilize TRP channels with great IR

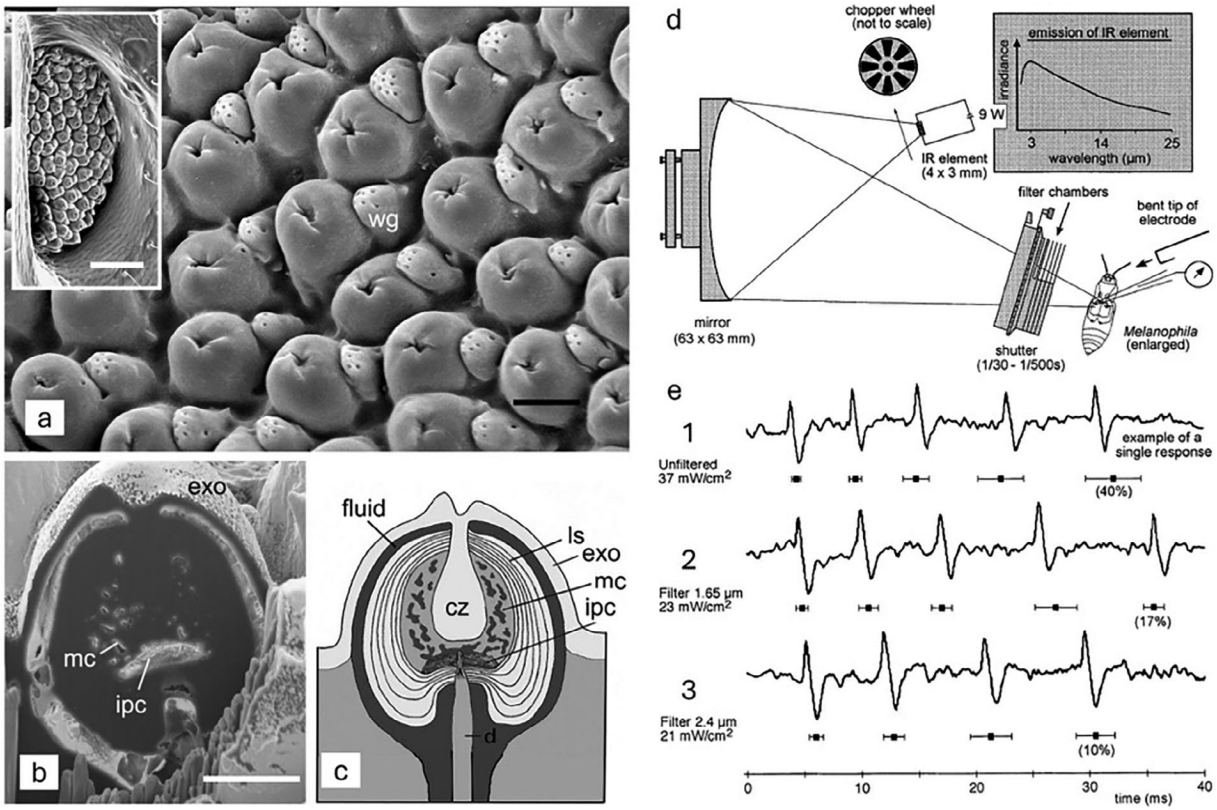

Figure 21. Infrared (IR) organ of *Melanophila acuminata*. a) Dome-shaped IR sensilla at the base of the organ (inset: whole organ). Each sensillum is accompanied by a smaller wax gland (wg) characterized by tiny pores. Bar: 15 µm (Inset 100 µm). b) Cross-section of single IR sensillum prepared by focused ion beam (FIB). Specimen was air-dried; therefore, only the cuticle is preserved. Microcavities (mc) of the intermediate layer and the inner pressure chamber (ipc) can be discerned inside the sphere. exo: exocuticular outer dome. Bar: 5 µm. c) Schematic drawing of a photomechanic IR sensillum covered by an outer dome of hard exocuticle (exo). The tip of the dendrite (d) is suspended by fine filaments inside the inner pressure chamber (ipc), which communicates with the fluid in the microcavities (mc) of the intermediate layer. Any increase in fluid pressure is transferred onto the dendritic membrane. (ls): lamellated exocuticular shell of the sphere. (a-c) Reproduced with permission.[93] Copyright 2015, MDPI. d) Experimental setup used for electrophysiological recordings. Inset: emission characteristic of the ORIEL IR element when supplied with 9W. Note that the maximum is at 3 µm (i.e., like that of a typical forest fire). e) Response of pit organ exposed to unfiltered IR stimulus (1), 1.65 µm long pass filter inserted into the camera shutter (2), and 2.4 µm longpass filter inserted into the camera shutter (3). d,e) Adapted with permission.[505] Copyright 1998, Springer.

adsorption properties (instead of photochemical transduction) for detecting radiant heat of warm-blooded animals at a distance of up to 1 m.[412] Additionally, fire beetles, *Melanophila acuminata* and *Merimna atrata,* require higher sensitivity to IR signals at much greater distances due to their reliance on burnt substrates (from forest fires) to grow and thrive.[55,410,502] The IR detection mechanism of *Melanophila acuminata* was first reported in 1997, which operates based on a photomechanical principle.[503] Within the pit organ of the fire beetle are 50–100 dome-shaped cuticular structures (15–20 µm in diameter) composed of layers of chitin fibers,[502] which houses IR sensilla (**Figures 21**a,b). At the top of each sensilla is a spherule containing an inner spongy structure that is filled with biological fluid and enclosed by a rigid exocuticle (Figure 21c).[504] Nanochannels in the chitinous exocuticle connect the spongy structure to a chamber outside of the shell to compensate for pressure fluctuations due to ambient temperature changes. The dendritic tip of a mechanosensitive neuron is anchored in the pressure chamber at the bottom of the inner spongy structure. When IR radiation illuminates the sensilla, the liquid in the inner spongy structure absorbs radiation energy and expands. Additionally, biological macromolecules, such as protein and chitin, rich in C—H, N—H, and O—H groups, which exhibit swinging frequencies in the range of 100 THz, can also absorb IR radiation in the range of 3 µm (corresponding to emission maximum of a forest fire),[505] and heat the liquid.[506] The increase in pressure caused by these reactions deforms the membrane of the dendritic tip (the only compliant component of this structure) with nanometer-scale displacement, which subsequently triggers the mechanosensory neuron.[55,502] Figures 21d,e demonstrates the sensitivity testing conducted by Schmitz et al., highlighting the fire beetle's ability to detect low-intensity IR signals.[505]

5.1.4. Magnetic Sensing

Some organisms have demonstrated the ability to sense and utilize magnetic fields for navigation. Prokaryotic microorganisms known as magnetotactic bacteria (**Figure 22**a)[507,508] synthesize approximately 20 magnetic nanoparticles with diameters of

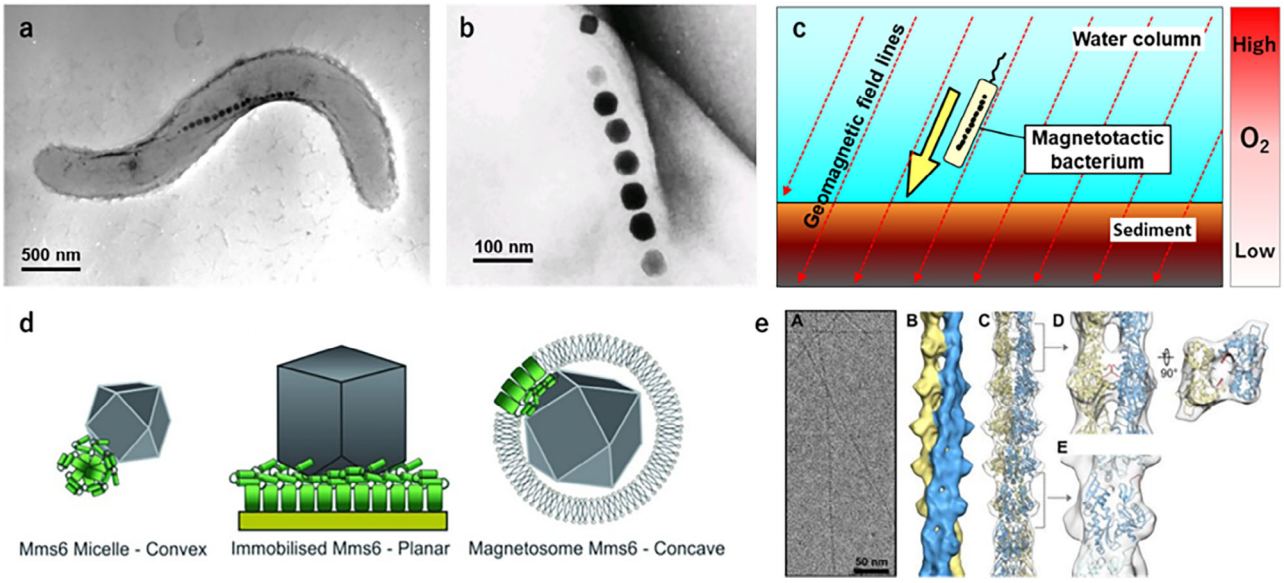

Figure 22. a) Transmission electron microscopy (TEM) micrographs of a magnetotactic bacterium and b) its magnetic particles. Adapted with permission.[508] Copyright 2008, RSP. c) Magnetic particles form a chain-like 1D structure within the bacterium and are postulated to function as biological compass needles that enable the bacterium to migrate along oxygen gradients in aquatic environments under the influence of the Earth's geomagnetic field lines. d) Formation of magnetic particles using various biomimetic surfaces with biomineralization protein Mms6. Reproduced with permission.[511] Copyright 2016, RSC. e) Cryo-EM reconstruction of MamK filaments. *A*, section of a micrograph of MamK filaments. *B*, three-dimensional reconstruction of the MamK filament. *C*, homology model of MamK fitted into the cryo-EM reconstruction. *Dashed brackets* indicate regions shown in greater detail in *D* and *E*. Reproduced with permission.[512] Copyright 2016, RSC.

approximately 40 nm within their cells (Figure 22b).[508] These particles form chain-like 1D structures within the cells, enabling the bacteria to orient themselves along Earth's geomagnetic field lines. The bacteria perform active oxygen sensing to reach the oxic-anoxic transition zone, which is typically located in the upper part of sediments.[509] The mechanisms controlling sizes and shapes of these 0D nanoparticles have been well elucidated in iron oxide nanoparticle formation. The size and morphology of these particles vary significantly between strains or cell types. Some morphologies, such as elongated or bullet-shaped particles, are unique to magnetotactic bacteria and cannot be reproduced through artificial chemical synthesis methods. Both 0D and 1D structure formations are regulated by magnetotactic bacteria-specific proteins encoded within their genomes.[508] The 0D structures—specifically the size and shape of individual particles—are regulated by multiple biomineralization proteins known as Mms proteins.[510](Figure 22d).[510] Furthermore, using Mms protein, various surface geometries have been successfully utilized for the fabrication of diverse magnetic materials[511] The 1D structures are formed by an acting-like filamentous protein called MamK, which controls the alignment of particles within the cells (Figure 22e).[512] Modifications of both 0D and 1D structures within the cells have been achieved by inducing or suppressing the expression of these proteins through genetic modifications.[513]

5.2. Biologically-inspired materials

Over the past few decades, researchers have looked to natural systems for inspiration for developing new sensors, seeking solutions for detecting different stimuli with high sensitivity and selectivity in complex natural environments. Studies of the male silk moth have resulted in new chemical sensors leveraging innovative synthesis techniques and practical applications of their bioinspired counterparts with similar hierarchical nanostructures. To date, gas-phase chemical sensors using semiconductor-, metal oxide-, nanofiber-, and chromatography-based platforms have been developed. From these, cantilever-based gas sensors utilizing moth antennae nanostructures have dramatically increased sensitivity.

5.2.1. Chemical Sensing

The concept of measuring bending or change in resonance frequency to detect adsorption was first proposed by Wilfinger et al. in 1968,[514,515] and implemented by Kolesar, who used micromechanical cantilevers for nerve agent detection.[516] With the proliferation and advancement of atomic force microscopy (AFM)[517] additional progress through the use of microcantilevers and sensitive instrumentation for capturing low-intensity signals.[515] Taking inspiration from the silk moth *Bombyx mori* antenna, Spitzer et al. fabricated micromechanical cantilever gas sensors that demonstrated practical detection of 2,4,6-trinitrotoluene (TNT, a component found in explosives) as low as 530 parts per trillion (ppt) with an estimated detection threshold below 1 ppt.[518] To reach this level of sensitivity, Spitzer et al. devised a two-step synthesis method to produce high surface area microcantilevers using physical vapor deposition (PVD) to form a 1μm metallic titanium layer onto a silicon microcantilever, followed by anodizing in a fluoride-containing electrolyte to form

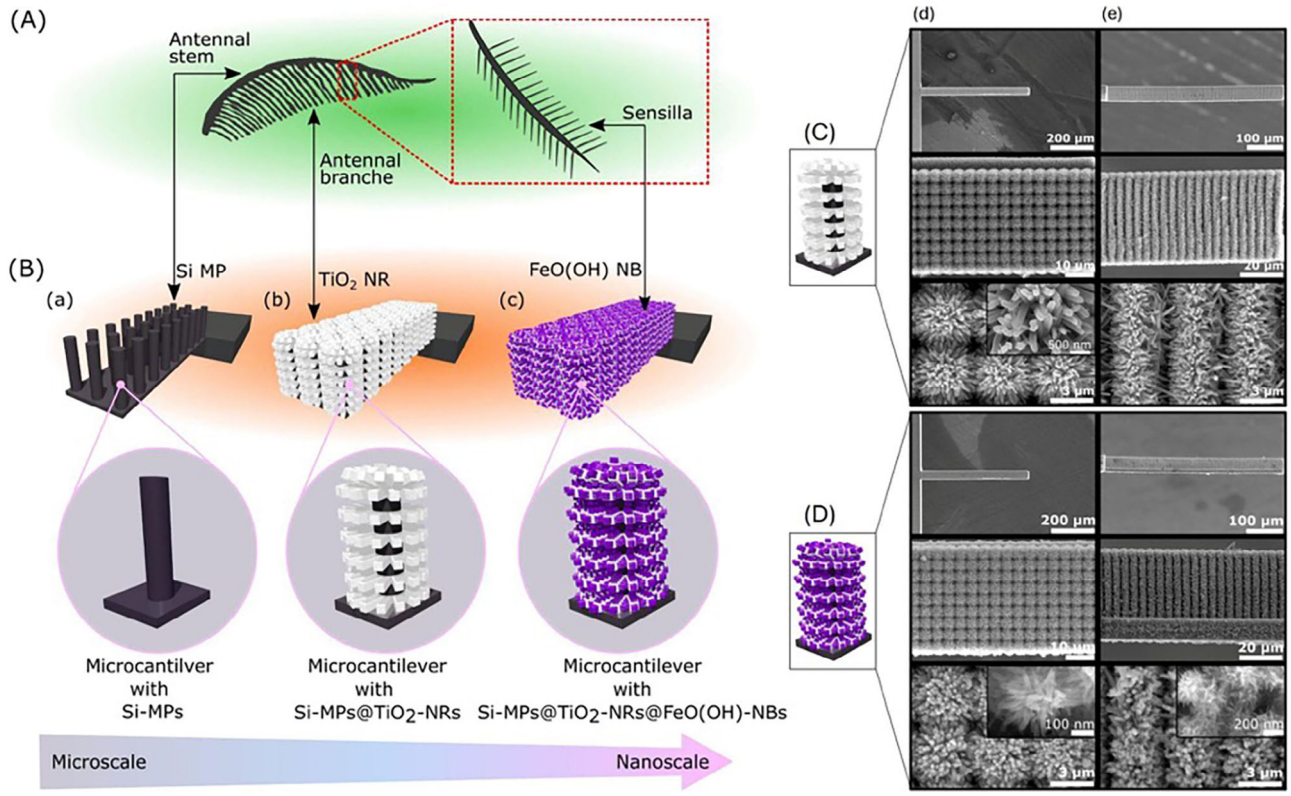

Figure 23. A) Schematic illustration of *Bombyx mori* antenna. B) Schematic demonstration of the multiscale 3D bioinspired hierarchical Si-MPs@TiO2-NRs@FeO(OH)-NBs core-shell superstructures on a microcantilever where a) a Si pillar corresponds to an antennal stem, b) TiO2 NRs on Si-MPs correspond to antennal branches, and c) FeO(OH) NBs on Si-MPs@TiO2-NRs are associated to sensilla. SEM images of a nanostructured microcantilever decorated with C) Si-MPs@TiO_2-NRs and with D) Si-MPs@TiO_2-NRs@FeO(OH)-NBs, with d) top views and e) side views. Adapted with permission.[95] Copyright 2022, Elsevier.

vertically oriented titania (TiO_2) nanotube arrays.[519] These nanotubes, which were 1700 ± 50 nm long and 100 ± 5 nm in diameter with a wall thickness of 20 ± 5 nm, are analogous to the sensilla found on moth antennal branches. The ability to fabricate with nanoscale precision and controlled orientation, a very high density of nanotubes (≈8×10^9 nanotubes cm^{-2}) was achieved, increasing the surface area of the cantilever by a factor of 80 and approximately two orders of magnitude greater number density compared to the silk moth *Bombyx mori* (600 to 900 sensilla per antennal branch). Thomas et al. fabricated a high-performance organophosphorus agent sensor that better mimics the hierarchical nanostructure of male silk moth antennae (**Figure 23**A).[95]

Starting with microcantilevers with silicon micropillar (MP) patterns on one side, TiO_2 nanorods (NR) were synthesized on the surfaces of MPs by first depositing a thin layer of Ti by PVD, followed by heat treatment to oxidize into TiO_2. A hydrothermal process was then employed to produce NR morphology (Figure 23B middle, and Figure 23C). Finally, goethite nanobranches (NBs), measuring 117 ± 18 nm in length and 19 ± 4 nm in diameter, were synthesized on the TiO_2 NR surfaces via a second hydrothermal process (Figure 23B, right, and Figure 23D). In this "highly vertical hierarchical and multiscale superstructure," the goethite NBs are analogous to the sensilla, wherein they are both the smallest functional unit of the sensor and the dominant adsorption sites of analyte molecules. The combined effect of increased surface area (factor of 490 compared to a microcantilever without nanostructure) and the facile binding of organophosphorus molecules to iron oxide surfaces promotes both mass and surface stress effects on the microcantilever, resulting in dramatic shifts in the resonance frequency under different exposure concentrations. Sensing experiments carried out against dimethyl methylphosphonate (DMMP), a common simulant of sarin gas, demonstrated detection limits as low as 3 ppb with a response time less than 70 s, demonstrating the sensor's ability to prevent death in humans (a lethal dose of Sarin equates to 10 min exposure at 64 ppb).[3,520]

In addition to enhancing the performance of microcantilever-based sensing technologies, researchers have also taken inspiration from the micromechanical and chemical mechanisms of insect olfaction. In the animal kingdom, volatile organic compounds (VOCs) are recognized by olfactory receptors as they are odorants that are crucial in survival. By comparison, the mechanisms involved in VOC recognition in insects are substantially simpler and require less components than those of mammalian olfaction.[521] Previous research has shown that various fruit flies in the genus *Drosophila* can detect VOCs with high sensitivity and selectivity.[522–524] A crucial component of insect olfaction is the secretion of odorant binding proteins (OBP), which, when combined with interesting nanostructures, facilitates the capture and diffusion of odorant molecules to the

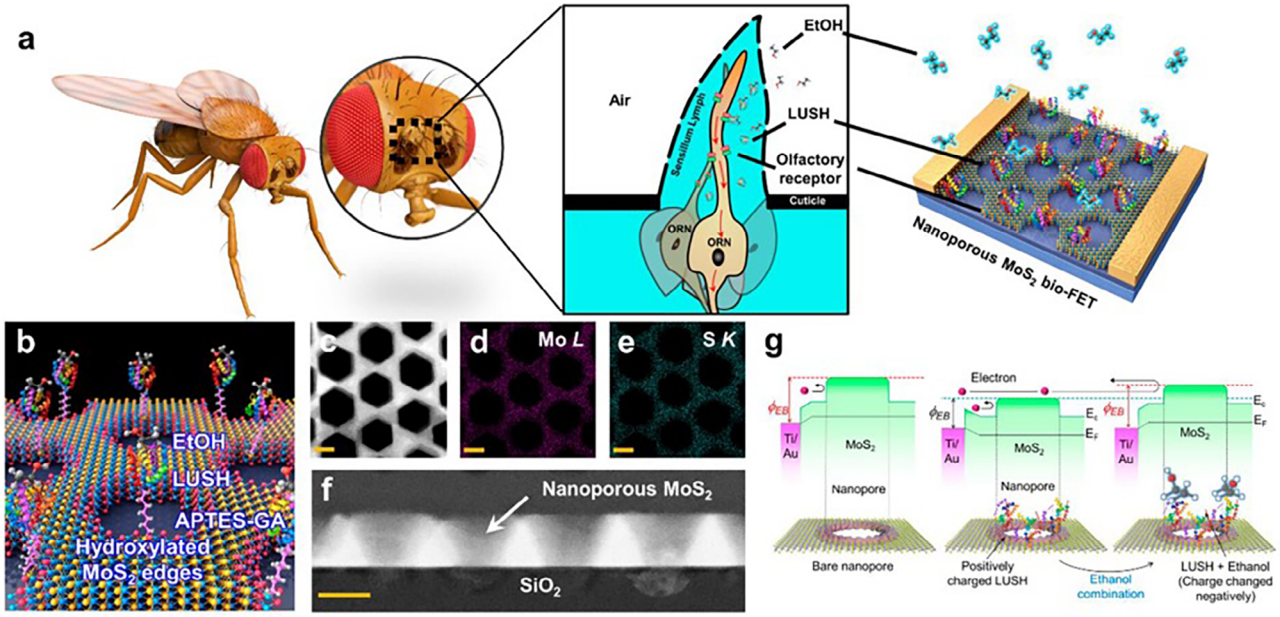

Figure 24. Hexagonal nanoporous MoS_2 FET-based EtOH sensor mimicking the *Drosophila* olfactory system. a) Schematic of *Drosophila* (left), close-up view of the head with antennae and maxillary palp (left inset), schematic of antenna containing olfactory organs (middle), hexagonal nanoporous MoS_2 bio-FET for detection of VOCs using LUSH (right). b) 3D representation of hexagonal nanoporous MoS_2 with selective edge functionalization. c) STEM micrograph of hexagonal nanoporous array (scale bar 20 nm); EDX elemental mapping of d) Mo L and e) S K peaks in hexagonal nanoporous MoS_2 (scale bar 20 nm). f) Cross-sectional STEM micrograph of throughout perforation of hexagonal nanoporous MoS_2 (scale bar 20 nm). g) Schematic images of energy barrier height corresponding to bare hexagonal nanopore (left), immobilized LUSH (middle), and EtOH coupled with LUSH (right) at the edges of the hexagonal nanopore. Reproduced with permission.[523] Copyright 2023, American Chemical Society.

olfactory receptors to trigger an electrical response (**Figure** 24a).[525] Shim et al. utilized similar designs to fabricate field-effect transistor (FET)-based gas sensors for volatile organic compound detection.[523] Inspired by the nanoporous sensilla and incorporation of OBP in fruit fly antenna, hexagonally nanoporous MoS_2 FET ethanol sensors were synthesized using a simple block copolymer lithography technique (Figures 24b-f). Block copolymer containing polystyrene and poly (methyl methacrylate) was applied on the MoS_2 nanosheets, which assemble to form a patterning mask. Subsequent dry etching with boron trichloride plasma and wet etching in diluted potassium ferricyanide of the MoS_2 nanosheets yields hexagonal nanopores with an approximate radius of 20 nm. Nanopores on the fruit fly antennas serve as pathways for odorant molecules to travel to the sensillum lymph space, where free-flowing odorant binding proteins and the olfactory receptors are housed. Similarly, the hexagonal nanopores of the MoS_2 FET serve both as the pathway and active sites of odorant binding. Sensitivity is further enhanced by immobilization of synthesized odor-binding protein LUSH on the edges and walls of the nanopores (Figure 24g), yielding an ultralow detection limit of 10^{-6} % ethanol that is critical for early detection of harmful VOCs in many industrial settings.

5.2.2. Mechanical Sensing

Studies of whisker structures in mammals and antennae in arthropods have informed the development of artificial tactile sensors capable of detecting minute pressure and vibrations, with applications in robotic skin, environmental monitoring, and minimally invasive surgical tools.[490] Natural systems can distinguish the diverse mechanical stimuli through several nanoscale-dependent mechanisms, including piezoresistive, piezocapacitive, piezoelectric, triboelectric, and iontronic responses.[408] For example, piezoelectricity is observed in biological materials like bone and certain connective tissues and has led to the development of bio-inspired flexible tactile sensors using materials like polyvinylidene fluoride (PVDF) and zinc oxide (ZnO) nanowires. Similarly, piezoresistive mechanisms rely on changes in electrical resistance due to mechanical deformation and are often achieved using carbon nanotube (CNT) composites embedded in stretchable polymers.[406,408] These diverse sensing modes enable multifunctional and multidirectional detection capabilities that are not only critical for the survival of organisms, but can be leveraged via bioinspiration using engineered nanomaterials that can be implemented into many applications.[406]

Bio-inspired tactile sensors (e.g., e-whiskers) inspired by the natural design and functioning of mammalian vibrissae have been developed by integrating high-aspect-ratio materials such as carbon nanotubes (CNTs) embedded in flexible polymers, simulating the natural counterpart's sensitivity and resilience. A key differentiation between natural vibrissae and bio-inspired E-whiskers is based on differences in the sensing mechanisms. While natural systems rely on follicular mechanoreceptors to relay stimuli, e-whiskers often use piezoresistive, capacitive, or even triboelectric mechanisms to translate mechanical interactions into readable signals.

For example, biomimetic e-whiskers made from carbon nanotubes (CNTs) combined with silver nanoparticles (AgNPs)

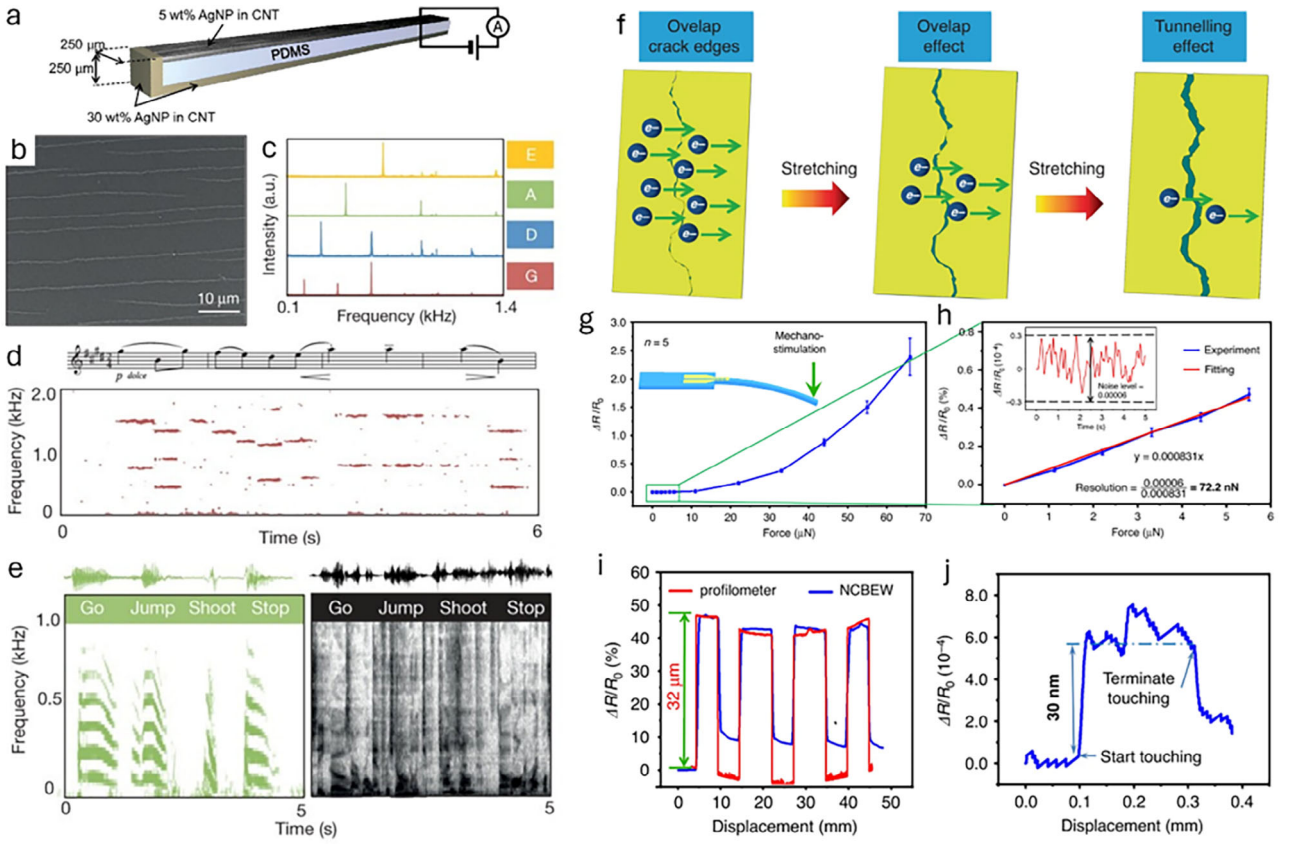

Figure 25. Electronic whiskers. a) Schematic showing the design of an e-whisker device with 5 and 30 wt.% AgNP composite lines patterned on the top and bottom surfaces of a PDMS fiber, respectively. Adapted with permission.[406] Copyright 2014, PNAS. b) SEM micrograph of nanoslits on the spider-inspired sensor. c) E (yellow), A (green), D (blue), and G (red) strings played open (with no finger stopping) produce different wavefunctions. Collected using a spider-inspired nanoscale crack sensor. d) The measured sound waves of music playing (Salut d'Amour; excerpt shown at top). e) Comparisons of the acoustic waveform and auditory spectrogram changes measured by electrical resistance using the nanoscale crack sensor (left-hand image) and a standing microphone (right-hand image) in a noisy (≈92 dB) environment. b–e) Adapted with permission.[97] Copyright 2014, Springer Nature. f) The resistance change of a nanocrack when the crack opens. g) The NCBEW mechanosensor responds to the applied force with a wide range from 0 to 67.5 μN. h) The linear relationship between the applied force and relative resistance changes within the range from 0 to 5.5 μN. Considering the noise level, the minimum resolution for force detection is as low as 72.2 nN. i) The scanning results of the NCBEW mechanosensor on the samples with a stage height of 32 μm. The blue line and red line indicate the data obtained by the NCBEW device and surface profilometer, respectively. j) The profiling results of a 30-nm-thick Au stripe on a glass substrate obtained from the NCBEW mechanosensor. Adapted with permission.[527] Copyright 2023, Springer Nature.

embedded in elastic polymers (**Figure 25**a) provide a highly flexible, yet responsive tactile sensor with tunable sensitivity.[406] Here, the CNT-AgNP films, fabricated by mixing CNT paste with AgNP ink, followed by patterning the composite onto a polydimethylsiloxane (PDMS) substrate and annealed, demonstrated significant pressure sensitivity and robustness through their conductive network. The synthesis involves Additional methods, as discussed by Sayegh et al.[490] include PDMS casting, screen printing, and various micro- and nano-fabrication techniques, such as photolithography and chemical vapor deposition (CVD), to achieve precise dimensions and enhance the mechanical properties of e-whiskers. These methods help to ensure that the artificial systems maintain the necessary flexibility and durability required for practical applications.

These e-whisker sensor systems have demonstrated utility for a wide range of industrial and robotic applications. Where traditional tactile sensors often rely on piezoresistive or capacitive mechanisms,[408] they lack the flexibility and rapid response required for more dynamic and complex environments. Conversely, bioinspired tactile sensors, such as the CNT-AgNP composite whiskers, exhibit a pressure sensitivity up to 8%/Pa—over ten times higher than conventional capacitive or piezoresistive sensors. This high sensitivity is attributed to the unique ultrastructure of the composite material, which allows for subtle changes in resistance in response to small deformations.[526] An et al. demonstrated a triboelectric nanogenerator (TENG)-based whisker system, which allows for self-powered tactile sensing. This system can detect forces as low as 1.129 μN and perform environmental mapping in low-visibility conditions. This high sensitivity is attributed to the unique nanostructural features of the composite material, which allow for subtle changes in resistance in response to small deformations.[526] Additionally, these TENG-based whiskers also provide alternative, self-powered, and sustainable robotic systems, with low energy consumption,

durability, and ease of integration for continuous operation.[406,490,526] Due to the effective modulation of electric resistance with mechanical deformation, these bio-inspired designs also result in heightened pressure sensitivity, far surpassing that of traditional tactile sensors.

Other mechanosensing strategies and mechanisms have been developed. Inspired by the aforementioned nanoslit lyriform structure of the spider tactile organ (Figure 25b), Kang et al. fabricated ultrasensitive mechanical sensors capable of detecting minute strains (gauge factor of over 2000 in the 0–2% strain range) and vibrations (detection amplitudes of ≈10 nm).[97] Fabrication of the ultrasensitive mechanical sensor involves deposition of a stiff, 20 nm-thick platinum (Pt) layer on a polyurethane acrylate (PUA) substrate, which mimics the viscoelastic properties of the spider tactile organ. Controlled nanoslits were then formed on the Pt layer by mechanically bending and subsequently cracking the Pt film, leading to a controlled crack density and directionality. Resistance across the Pt film is used as the signal for recognizing vibration and strain (i.e., as the Pt film bends, resistance would increase due to the discontinuity of the film). This affords a significant advantage whereby non-linear nanocracks in the Pt film result in continuous resistance variations due to gap-bridging steps along the zigzag edges of the cracks. Testing of the sensors involved direct pressure application, which was conducted by mounting the sensor on a violin or a human neck. These experiments demonstrated capabilities beyond recognizing simple strains, including voice recognition with much better recognizable patterns compared to a microphone as well as the potential for speech recognition (Figures 25c–e).

In addition, Zhang et al. fabricated a highly sensitive nanocrack-based electronic whisker (NCBEW) that combines the sensory mechanisms of whisker deflection and nanoslit compliance.[527] Sensing fibers were fabricated using thin strips of polydimethylsiloxane (PDMS) as cantilevers to mimic the flexibility of animal whiskers. A gold film sputtered on the PDMS cantilever was subsequently patterned using photolithography to define the placement of nanocracks, formed by bending the cantilever. Resistance across the Au film was used as a signal for the detection of mechanical forces. When the cantilever bends inwards such that the crack edges are forced into contact, resistance decreases because of the overlapping effect, wherein compressive forces from this bending motion close cracks, leading to a decrease in resistance (Figure 25f).[528] Interestingly, when the cantilever is stretched and the cracks open, the resistance experiences an instantaneous change in resistance proportional to the applied strain due to the tunneling effect of the metal–insulator (air)–metal arrangement (Figure 25f).[529] Their mechanosensor demonstrated a detection resolution of 72.2 nN, which was further improved by reducing the flexural rigidity of the sensing fiber (i.e., using softer materials or a thinner cantilever), such that a smaller flexural event induces a larger response in resistance (Figures 25g,h) response. Topographical investigations of smooth surfaces using the NCBEW showed comparable sensitivity and signal stability to commercial surface profilometers (Figure 25i). Its ability to recognize 30 nm-thick surface features demonstrates the ultrasensitivity of this design with potential applications in sensing minute forces, such as tactile recognition, air flow monitoring, gravitational field orientation, and fall detection (Figure 25j).

5.2.3. Thermal Sensing

Detection of temperature fluctuations and radiant heat is crucial across many fields, including medical diagnostics, industrial maintenance, environmental monitoring, and surveillance.[379,530–532] As previously mentioned, organismal sensing against various stimuli is achieved via ion channels within nerve cells. The conformational changes of these biological nanochannels induced by stimuli enable or prohibit the transport of species across biological membranes. This nanogating function for molecular transport is essential for the next generation of nanodevices. In addition, the tunable functions, flexibility in shape and size, ability to operate in complex environments, and superior robustness of biological ion channels are also desirable properties in bio-inspired artificial nanochannels.[499,533–538]

The thermogating mechanism of artificial temperature-sensitive nanochannels is currently being explored in numerous different ways. One of the first and most heavily explored methods is the use of thermosensitive polymers, specifically poly(*N*-isopropylacrylamide) (PNIPAM). Azzaroni's group was the first to demonstrate an artificial solid-state ion nanochannel by using PNIPAM to modify the surface of a polyimide (PI) conical nanopore.[533] PNIPAM, acting like molecular brushes, undergoes conformational changes at a lower critical solubility temperature (LCST), as such, when the temperature is raised above the LCST, PNIPAM brushes dehydrate into a collapsed state to increase in the effective cross-section of the nanopore, thereby increasing the flow of ions (**Figure 26**a, left). Conversely, when the temperature drops below the LCST, PNIPAM brushes swell and prevent ionic flow (Figure 26a, right).[533] Biological ion channels also possess ionic rectification properties, wherein the current is asymmetric under different potential bias, which is analogous to the *I*–*V* response of semiconductor diodes.[539] To engineer such properties, Jiang's group decorated gold-coated nanopores with PNIPAM and fabricated a temperature-responsive single-nanopore ionic rectifier.[540] At temperatures below LCST, the nanochannel is able to rectify ionic currents due to the surface charge retained by the anions adsorbed to the gold pore wall. At temperatures above LCST, the nanochannel exhibits ohmic ion transport behavior (Figure 26b). They later demonstrated the use of multi-polymer systems, synthesized through a layer-by-layer method, resulted in the continuous tunability of ion rectification at different temperatures (Figures 26c,d).[541]

Beyond direct temperature monitoring, IR detection also has potential applications in industrial monitoring, owing to its non-contact and non-invasive features. IR detection technologies were initially limited to military research, development, and use, until their declassification in 1992.[543] IR detection can be classified into two types based on its operation conditions: cooled IR detection and uncooled IR detection. Cooled IR detection mechanisms typically involve either photocurrent or photovoltaic technologies, both requiring cryogenic or thermal-electric cooling systems, which are bulky and expensive.[55] By comparison, uncooled IR detection is simpler, smaller, and less expensive,

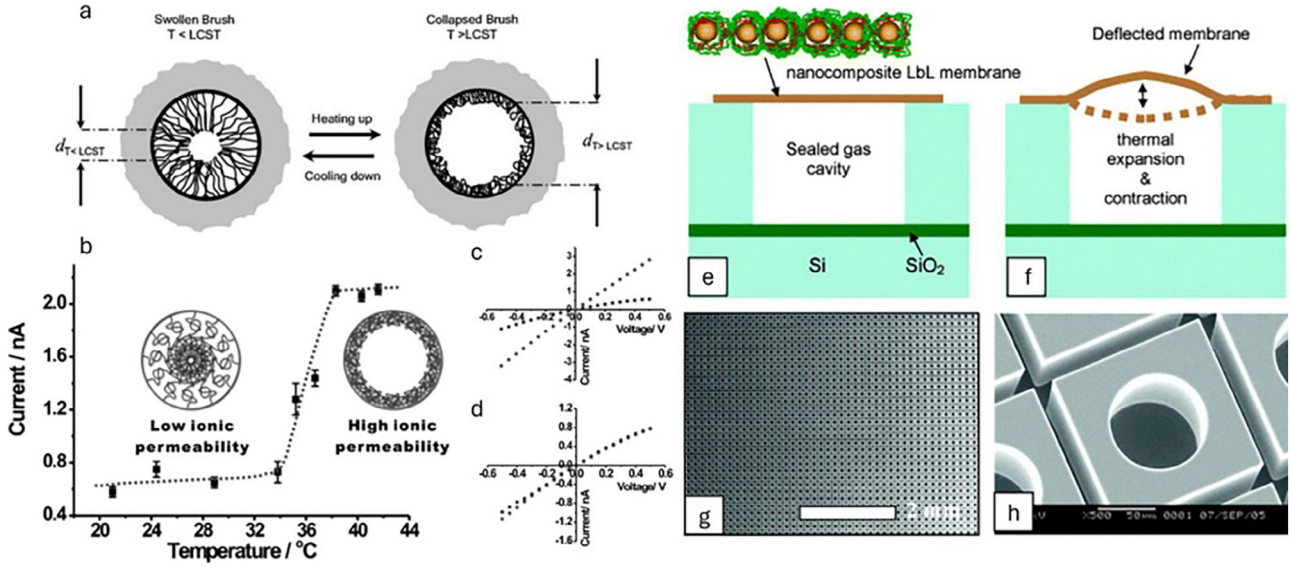

Figure 26. a) Cartoon describing the thermally driven nanoactuation of the PNIPAM brushes in the nanopore as demonstrated by Azzaroni's group. Reproduced with permission.[533] Copyright 2009, Wiley. b) Temperature dependence of the ionic current through the PNIPAM-modified single nanopore as demonstrated by Jiang's group. The inset cartoons illustrate the gate-like temperature-responsive change in effective pore size. c,d) *I–V* curves measured on single conical gold-coated nanopores with and without PNIPAM modification, respectively. b–d) Adapted with permission.[540] Copyright 2010, Wiley. e,f) Cartoon of a microcavity sealed with a freely suspended nanomembrane in the planar state at room temperature (e) and in deformed states (f). g) SEM micrograph of the silicon substrate with a uniform array of microcavities; and h) higher magnification SEM image showing the smooth edges of the microcavity and the trenches separating the individual cavities. Reproduced with permission.[542] Copyright 2006, American Chemical Society.

subsequently receiving significant attention from the United States Department of Defense, with major development grants awarded to industry partners (e.g., Honeywell and Raytheon).[543] Although these efforts were successful, uncooled IR technology still trails cooled IR technology in terms of sensitivity and spatial resolution.

As previously mentioned, biology has developed strategies to execute uncooled IR detection with great sensitivity and precision without complex and costly infrastructures, which prompted researchers to explore bio-inspired approaches. Tsukruk et al. developed an IR sensor that follows a similar thermal-pneumatic transduction mechanism of the aforementioned fire beetles.[542] Ultrathin nanocomposite membrane composed of a monolayer of gold nanoparticles and polymers (via layer-by-layer deposition)[544] was used to seal an array of microcavities in silicon substrates (Figures 26e–h). Changes in temperature and IR illumination resulted in the expansion or contraction of the air inside the microcavities, which deflects the membrane inward or outward. In addition, the lack of cross-talking between neighboring microcavities suggests the possibility of high-resolution IR microimaging with this device.

5.2.4. Magnetic Sensing

Based on investigations of magnetotactic bacteria described above, researchers have leveraged their magnetic properties for medical-based applications. Various functional molecules can be displayed on the magnetic particle surfaces, making them applicable for cell separation and immunoassay techniques based on bound/free separation.[508] Particle production has also been enhanced through the genetic modification of the genomes.[513] This synthetic biological approach will potentially enable the design and creation of novel organisms capable of producing functional 0D and 1D magnetic structures de novo.

6. Perspective and Opportunities

This review provides an overview of the implementation of nanoscale features of simple biogenic materials that have enabled the exceptional performance and survival of biological organisms. The advantages of exploring these systems, which have evolved over millennia, are many. We cannot only implement advanced materials that surpass the performance of the limited selection of biogenic materials, but we can also integrate them using biological blueprints that yield engineered structures that far outperform current engineering structures that have been developed for only a few hundred years. In addition to this, most biological structures that we have presented demonstrate multifunctionality, often providing, for example, mechanical stability as well as additional capabilities (e.g., thermal resistance, self-healing, self-sensing, etc.). This is often achieved by design tradeoffs, where biological systems may sacrifice some of one type of performance to enhance another (e.g., microtubules that cross lamellar in arthropods are mechanical defects but offer self-healing or even self-cooling). In addition, many biological systems, which are assembled under ambient conditions to form exquisite architectures with high fidelity, offer a wealth of information towards new synthesis and manufacturing pathways—including addressing sustainable processes as well as reducing

waste at the product end of life. With millions of species demonstrating exquisite functionality, there is a plethora of opportunities to investigate organismal material selection, formation pathways, multiscale architectures, and built-in multifunctionality—all of which offer valuable insights into novel synthetic strategies and design paradigms that will benefit our society and planet. Thus, the following section presents both challenges and opportunities for scientists and engineers that may leverage biological systems for new, environmentally friendly, advanced materials.

6.1. Challenges

6.1.1. Structural complexity

Materials selection governs the overall trajectory of the synthesis pathway for both biogenic and synthetic systems. In biological systems, material composition is largely governed by the availability of nutrients and fundamental building blocks in the environment, in conjunction with evolutionary constraints and selective pressures. For example, many marine organisms such as echinoderms,[545] mollusks,[546] corals,[547] crustaceans,[548] forams,[549] and coccolithophores[550] have used calcium carbonate mineral for their skeletal structures. Although inherently brittle, these organisms have compensated by producing sophisticated structures that resulted in exceptional performance.

Man-made materials, on the other hand, are produced from a nearly unlimited selection of materials, which presents issues, such as reliance on mining, transportation, and complex, often energy-intensive, fabrication processes, contributing negatively to the environment. Despite the arduous fabrication processes, these synthetic-based materials often fall short of specific performance characteristics found in natural systems. This is, in part, due to the lack of multiscale architectures exhibited in biological systems, which as described earlier, have established controlled synthesis and hierarchical assembly of nano- to micro-scaled building blocks.[20–33] The underlying driver behind this exquisite organization is the spatial and temporal regulation of organic formation and mineral assembly, which is required to achieve functional anisotropy and integration with ad hoc emerging properties commonly observed in natural systems.[36] Biological systems use specific molecular cues, such as those encoded in protein sequences, to direct the growth pathway with high fidelity.[551] In order to leverage biological processes, additional knowledge of these systems is required. There exist some critical gaps in our understanding of cellular processes for synthesis, transport, modification, assembly, and storage of biomaterials. The genes and their regulatory networks involved in these cellular processes, as well as the control of ion transportation through nanochannels, are largely unknown. Furthermore, sequence-specific functions, dynamics, conformation, and assembly behavior of proteins are largely unknown due to challenges in characterization and limitations of current simulation methods.[552–554]

In addition, the physical and chemical phenomena that help to control biosynthesis processes, especially those at the organic-mineral interface, are still relatively unexplored. Also, the 2D and 3D structures of proteins, whose conformational states often dictate kinetic pathways of syntheses, are unknown in complex media. Through a greater understanding of the role of these interfaces and molecular-scale architectures, new synthesis processes demonstrating greater control can be developed. Some challenges that still exist are the development of advanced characterization methodologies that provide real-time information of these processes and architectures. Development of new, ultrafast in situ techniques, such as in atomic force microscopy, transmission electron microscopy, and synchrotron X-ray, may reveal knowledge about dynamic processes, the role of these interfaces, etc., which will aid in the advancement of bio-inspired processes.

Many bio-inspired processes utilize functionalized organics to control the nucleation and growth of nanoscale materials. These are being explored, for example, via controlled nanoparticle growth,[555–557] use of insoluble crystalline polymers or self-assembled monolayers as templates for inorganic crystallization.[83,317,558] These bio-inspired synthesis processes typically involve the use of readily available high-purity organics (polymers, alkane thiols, etc.), which are less complex than their biological counterparts that are capable of controlling both nucleation, growth, and self-assembly that provides the multiscale architectures in biological structures. Although their synthesis (and yield, see the next section 6.1.2) is challenging, new methods are being identified to synthesize structurally complex polymers used as templates for mineralization. These novel techniques are discussed in greater detail in Section 6.2.2.

6.1.2. Scalability

Aside from the difficulty in synthesizing complex hierarchical nanostructures, the ability to produce these materials at scale remains a significant challenge. While biological systems can use environmentally friendly processes and ambient conditions to synthesize and assemble structures over a period of hours or even days, industrial processes[559,560] require much faster or capital-intensive processes, which are often costly,[561,562] environmentally unfriendly, or require significant time for optimization.[563] These time constraints present significant challenges toward the scalable manufacturing of highly controlled, architected nanomaterials. To realize the spatial resolution and precision needed for nanomaterial production at an economically beneficial time scale, fabrication processes usually involve complex instrumentation, stringent and harsh conditions, diverse (sometimes scarce) materials, etc.[564] These industrial processes can lead to inhomogeneous size distributions as well as defects or impurities that are deleterious to performance;[564,565] post-synthesis instability and agglomeration of nanomaterials;[565,566] challenges in quality control over large quantities, especially surface, and interfaces.[567] In contrast, bio-inspired fabrication approaches are being explored, offering potential for a high level of control while significantly reducing cost and complexity in nanomaterial production.[568,569]

6.2. Opportunities

6.2.1. Novel Techniques in Synthesis and Characterization

One of the primary drivers for the multi-scale formation of biological nanostructures is spatial and temporal control of assembly

of molecularly architected biological macromolecules (e.g., structural polysaccharides and functional proteins) with concurrent and kinetically controlled mineralization. One potential solution for synthetic processes is the utilization of peptidomimetics and proteomimetics to synthesize artificial sequence-defined polymers, which has attracted great interest in recent years. Through methods such as precise macromonomer polymerization[570] and iterative growth,[571,572] researchers have demonstrated the ability to fabricate synthetic analogs of biological polymers.[573,574] Replicating tertiary protein topology is also possible through manipulation of intramolecular cross-linking and partial or complete alterations of the backbone composition.[575] Furthermore, previous research demonstrates how these artificial sequence-defined polymers can be used to control the mineralization of inorganic materials,[576–578] which opens up an entirely new field of inorganic synthesis with greater control over the free energy landscape of nucleation and growth.

To accelerate the development of synthetic analogs of biological macromolecules, researchers have benefited from using modeling and simulation to facilitate various stages of bio-inspired syntheses. Accurate protein visualization has become more achievable with novel computational methods like AlphaFold, helping researchers study the exquisite adaptability, complexity, and utility of biological templates.[579]

Data science-driven approaches also provide insight for the development of bio-inspired materials by correlating experimentally gathered data with computational predictions.[78] Simulations based on density functional theory (DFT) can predict atomic-level interactions, while reactive molecular dynamics (MD) and coarse-grained (CG) simulations extend this knowledge to larger spatial and temporal scales.[580–582] DFT calculations can predict mechanical properties like strength and stiffness at the atomic level. MD simulations can highlight interphase behavior,[179,180] design polymer sequences,[583] determine binding mode[584] and growth rate,[577] and assess mechanical properties of nanostructures.[78,84] Coarse-grained simulations further scale these insights, shedding light on larger structural features such as assembly interdigitation in polymer-grafted nanoparticles.[585] At the macroscale, finite element methods (FEM) and peridynamics models can simulate fracture mechanisms and energy dissipation in composite materials.[586–589] As these hierarchical strategies enable researchers to explore material properties for optimizing design, machine learning (ML) and materials informatics can further accelerate material innovation when coupled with the aforementioned predictive modeling techniques.[590] In a similar vein, machine learning has also been utilized for process optimization of nanomaterial synthesis,[591] allowing researchers to fine-tune instrument parameters efficiently.[592] By leveraging data science to study biology's resource-efficient and multifunctional design strategies, we can uncover sustainable approaches that not only reduce environmental impact but also enhance material performance—ultimately meeting the modern demand for multifunctionality.[593,594]

Advanced characterization methods are also crucial in revealing details of multiscale architectures as well as validating and testing the bio-inspired materials. Significant effort has been invested in improving the characterization of biological and synthetic nanomaterials, including the use of advanced tip-based spectro-microscopy techniques,[595,596] mass spectrometry,[597,598] and cryo-electron microscopy.[599] Visualization of nanomaterials typically involves electron microscopy, wherein topography is investigated via scanning electron microscopy (SEM)[600] or tip-based microscopy,[601] while crystallinity and internal structure are investigated via transmission electron microscopy (TEM).[602] Due to the need to investigate complex local composition of biological and bio-inspired nanomaterials, novel spectro-microscopy has been developed to push the spatial resolution and detection limit of elemental/chemical characterization. These typically involve the combined use of microscopy techniques capable of atomic resolution and spectroscopy techniques that can be focused on nanoscale features, allowing both visualization of nanomaterials and elemental/chemical mapping of small samples. Starting from elemental composition, high-resolution scanning transmission electron microscopy (HRSTEM) coupled with energy dispersive X-ray spectroscopy (EDX) or electron energy loss spectroscopy (EELS) is often utilized and has achieved atomic resolution.[603] While spectroscopy-coupled HRSTEM is relatively commonplace in most research environments, nanometer-resolved chemical investigations have been challenging due to the processes involved in signal-generating mechanisms from complex molecules. Nevertheless, emerging techniques, such as atomic force microscopy-based infrared spectroscopy (AFM-IR) and tip-enhanced Raman spectroscopy (TERS), demonstrate investigation of local chemistry with spatial resolution far below conventional optical diffraction limits.[604,605] Lab-scale utilization of AFM-IR showcased consistent nanoscopic chemical mapping of specific vibrational modes for different classes of materials, including minerals, polymers, and biological samples.[604] New techniques and apparati are also being developed to investigate nanomechanical properties,[606] surface characteristics,[607] and material properties in situ.[608] While AFM-IR excels in the characterization of complex heterogeneous samples, TERS is capable of achieving atomically resolved chemical investigation. Most notably, researchers have been able to resolve structural and chemical heterogeneities of a molecule at the single-bond limit.[609] Furthermore, protein sequencing with lateral resolution better than 2 nm has been realized to probe secondary structures, allowing researchers to investigate the structural complexities of biological macromolecules and their function.[595] Clearly, this ever-evolving field of nanomaterial characterization will play a crucial role in advancing the understanding of synthesis-structure and structure-function relationships in biological and bio-inspired materials.

6.2.2. Additive Manufacturing

Rapid advancements in additive manufacturing (AM) have been made within the past decade and provide significant potential as a high-throughput method for fabricating bio-inspired structures.[610–612] This is, in part, due to advantages such as printing complex organic forms, cost effectiveness, speed, and material compatibility.[613]

Montroni et al. demonstrated direct ink write printing of chitin-based gel fibers with control over molecular orientation by inducing different extrusion conditions (pressure, needle diameter, needle geometry).[272] AM of bio-inspired nanoscale

features is not commonplace, but there is still success in the direct synthesis of biological nano-motifs through methods such as two-photon polymerization.[225,614] In addition, field-assisted AM has been used to form hierarchical structures, and post-processing (mineralization) of printed structures offers potential to print composites with multiscale structures.[615–618]

There is also a significant opportunity to fabricate hierarchical, multiscale heterogeneous structures that can leverage developments in polymer science and engineering. Here, inks that are used in printing can incorporate block co-polymers (BCP) or even engineered biological macromolecules that incorporate functional domains that can bind to, and induce nucleation of selected inorganic nanocomponents, while other domains can be selected to control folding into specific architected designs. In fact, researchers have identified self-assembly as an ideal candidate for nanomaterial production scale-up while maintaining control of the resulting nanostructures[619,620] with enhanced chemical and structural complexities[621] that can self-assemble into higher order structures have demonstrated utility in the controlled growth of inorganic nanomaterials,[622] and have deservedly received great research interest in the 21st century.[623] These polymer templates provide tunability of the nucleated materials, wherein the structure and chemistry of the designed block copolymer and the solution in which the polymer is dissolved can be manipulated to control assembly.[624,625] Many morphologies have been obtained and identified through BCP self-assembly, including micelles, rods, lamellae, vesicles, and hexagonally packed hollow hoops.[626] These can act as stand-alone functional units with engineering applications, such as energy storage,[627,628] photonics,[629] and drug delivery,[630] but when utilized as templates for inorganic growth, results in exquisite nanostructures that would be nearly impossible to fabricate with conventional top-down processes.[631] Furthermore, significant advances in self-assembly have been made with DNA,[632–634] RNA,[635,636] and proteins.[637,638] Proteins, for example, demonstrate highly tunable secondary structures formed to generate expressed functional groups to afford controlled nucleation of mineral components and can thus be leveraged to form nanoarchitected structures. These types of templated growth techniques are inherently similar to biological material growth, wherein biological macromolecules impart structural complexity on the resulting biominerals. Thus, integration of these self-assembled and templating macromolecules offers new opportunities for achieving multi-scale architectures that replicate biological designs.

6.2.3. Multifunctionality

The exploration of multifunctionality in bio-inspired nanomaterials represents the next frontier, unlocking the capacity to perform complex, integrated functionalities seen in biological systems. While significant research has yielded bio-inspired monofunctional materials (i.e., structural, optical, thermal, and sensing), researchers investigating mechanically robust biological structures that integrate additional functionality often involve non-trivial trade-offs. For example, tubules and channels are often found in mechanically robust biological systems, such as insect cuticles,[36] crustacean exoskeletons,[639] and bones,[640] providing pathways for nutrient transport during regeneration and healing processes. However, tubules and channels are defects that weaken the overall structure. Through evolution, such compromises to achieve multiple functionalities are demonstrated in many organisms.[641,642]

In another example, the aforementioned Saharan silver ant (*Cataglyphis bombycina*) demonstrates thermal-optical functionalities through triangular-shaped nanohairs that simultaneously enhance reflectivity in the visible and near-infrared spectrum while increasing thermal emissivity in the mid-infrared range.[373,643,644] Similarly, the butterfly wing scales of Morpho butterflies exhibit nanoscale chitin architectures that produce structural coloration while facilitating thermal regulation.[322,324,342] Multifunctionality in nature is not limited to thermal-optical systems, but extends across various domains, including structural, sensory, and biochemical interactions. This inherent characteristic of biological materials to respond adaptively to a wide array of environmental challenges offers an ideal blueprint for the development of synthetic materials. While some organisms have been studied, significant opportunities exist via the exploration of the many multifunctional biological systems.

Addressing the barriers to synthesizing multifunctional nanostructures requires tackling further interconnected challenges, including scalability, advanced characterization, and the integration of current knowledge across length and timescales. These challenges hinge on achieving at least the level of complexity and integration found in natural systems and their subsequent design. Many challenges lie in front of researchers striving to truly embrace biological inspiration to attain the same level of fidelity and performance of biogenic materials. However, this also means there are many exciting opportunities for growth. With multidisciplinary efforts, which can combine the use of biology with materials science, chemistry, mechanics, and additive manufacturing, coupled with advanced characterization, multiscale modeling, and machine learning, we can more deeply understand synthesis and assembly pathways in biological systems and translate these to produce the next generation of high-performance and even sustainable engineered materials.

Acknowledgements

Air Force Office of Scientific Research, FA9550-20-1-0292 (D.K.); Air Force Office of Scientific Research, FA9550-23-1-0647 (D.K.); Air Force Office of Scientific Research, FA9550-15-1-0009 (D.K.); Air Force Office of Scientific Research, FA9550-23-1-0209 (D.K.); Army Research Office, W911NF-20-1-0201; the Institute of Global Innovation Research (GIR) at TUAT (D.K., A.A.).

Conflict of Interest

The authors declare no conflict of interest

Keywords

biological materials, bio-inspired materials, nanostructures, structure-function relationships

Received: May 16, 2025
Revised: August 4, 2025
Published online: September 22, 2025

[1] H. C. J. Godfray, J. R. Beddington, I. R. Crute, L. Haddad, D. Lawrence, J. F. Muir, J. Pretty, S. Robinson, S. M. Thomas, C. Toulmin, *Science* **2010**, *327*, 812.
[2] M. L. Brusseau, *Environmental and Pollution Science*, Elsevier Science & Technology, San Diego, **2019**.
[3] S. R. Ede, H. Yu, C. H. Sung, D. Kisailus, *Small Methods* **2024**, *8*, 2301227.
[4] F. Pacheco-Torgal, J. A. Labrincha, *Int. J. Sustain. Eng.* **2014**, *7*, 235.
[5] R. Repetto, T. Holmes, *Popul. Dev. Rev.* **1983**, *9*, 609.
[6] K. B. Boamah, J. Du, A. J. Boamah, K. Appiah, *Environ. Sci. Pollut. Res.* **2018**, *25*, 5862.
[7] Worldwide Nanomaterials Industry to 2029 - Emerging Applications in the Electronics Industry are Driving Growth - ResearchAndMarkets.com, https://www.businesswire.com/news/home/20210514005289/en/Worldwide-Nanomaterials-Industry-to-2029-Emerging-Applications-in-the-Electronics-Industry-are-Driving-Growth-ResearchAndMarkets.com (accesssed: August 2025).
[8] Nanotechnology Market, FORTUNE Business Insights **2025**, https://www.fortunebusinessinsights.com/nanotechnology-market-108466 (accessed: April 2025).
[9] W. Wang, G. Yang, H. Cui, J. Meng, S. Wang, L. Jiang, *Adv. Healthcare Mater.* **2017**, *6*, 1700003.
[10] S. Mitragotri, D. G. Anderson, X. Chen, E. K. Chow, D. Ho, A. V. Kabanov, J. M. Karp, K. Kataoka, C. A. Mirkin, S. H. Petrosko, J. Shi, M. M. Stevens, S. Sun, S. Teoh, S. S. Venkatraman, Y. Xia, S. Wang, Z. Gu, C. Xu, *ACS Nano* **2015**, *9*, 6644.
[11] M. C. Roco, *J. Nanoparticle Res.* **2011**, *13*, 427.
[12] H.-B. Yao, H.-Y. Fang, X.-H. Wang, S.-H. Yu, *Chem. Soc. Rev.* **2011**, *40*, 3764.
[13] J. Wang, Q. Cheng, Z. Tang, *Chem. Soc. Rev.* **2012**, *41*, 1111.
[14] J. J. De Yoreo, in *Bio-Inspired Nanotechnology* (Eds.: M. R. Knecht, T. R. Walsh), Springer New York, New York, NY **2014**, pp. 291-314.
[15] N. Abid, A. M. Khan, S. Shujait, K. Chaudhary, M. Ikram, M. Imran, J. Haider, M. Khan, Q. Khan, M. Maqbool, *Adv. Colloid Interface Sci.* **2022**, *300*, 102597.
[16] C. Crook, J. Bauer, A. Guell Izard, C. Santos De Oliveira, J. Martins De Souza E Silva, J. B. Berger, L. Valdevit, *Nat. Commun.* **2020**, *11*, 1579.
[17] J. C. Weaver, Q. Wang, A. Miserez, A. Tantuccio, R. Stromberg, K. N. Bozhilov, P. Maxwell, R. Nay, S. T. Heier, E. DiMasi, D. Kisailus, *Mater. Today* **2010**, *13*, 42.
[18] J. Yan, T. Zhou, X. Yang, Z. Zhang, L. Li, Z. Zou, Z. Fu, Q. Cheng, *Angew. Chem., Int. Ed.* **2024**, *63*, 202405228.
[19] W. Huang, N. A. Yaraghi, W. Yang, A. Velazquez-Olivera, Z. Li, R. O. Ritchie, D. Kisailus, S. M. Stover, J. McKittrick, *Acta Biomater.* **2019**, *90*, 267.
[20] L. Addadi, S. Weiner, *Proc. Natl. Acad. Sci. USA* **1985**, *82*, 4110.
[21] L. Addadi, S. Weiner, *Angew. Chem. Int. Ed.* **1992**, *31*, 153.
[22] J. Aizenberg, J. Hanson, T. F. Koetzle, S. Weiner, L. Addadi, *J. Am. Chem. Soc.* **1997**, *119*, 881.
[23] A. M. Belcher, X. H. Wu, R. J. Christensen, P. K. Hansma, G. D. Stucky, D. E. Morse, *Nature* **1996**, *381*, 56.
[24] G. Falini, S. Albeck, S. Weiner, L. Addadi, *Science* **1996**, *271*, 67.
[25] A. George, B. Sabsay, P. A. Simonian, A. Veis, *J. Biol. Chem.* **1993**, *268*, 12624.
[26] B. R. Heywood, S. Mann, *Adv. Mater.* **1994**, *6*, 9.
[27] G. K. Hunter, H. A. Goldberg, *Proc. Natl. Acad. Sci. USA* **1993**, *90*, 8562.
[28] G. K. Hunter, H. A. Goldberg, *Biochem. J.* **1994**, *302*, 175.
[29] N. Kröger, R. Deutzmann, C. Bergsdorf, M. Sumper, *Proc. Natl. Acad. Sci. USA* **2000**, *97*, 14133.
[30] Y. Levi, S. Albeck, A. Brack, S. Weiner, L. Addadi, *Chem.-Eur. J.* **1998**, *4*, 389.
[31] H. Miyamoto, T. Miyashita, M. Okushima, S. Nakano, T. Morita, A. Matsushiro, *Proc. Natl. Acad. Sci. USA* **1996**, *93*, 9657.
[32] C. A. Orme, A. Noy, A. Wierzbicki, M. T. McBride, M. Grantham, H. H. Teng, P. M. Dove, J. J. DeYoreo, *Nature* **2001**, *411*, 775.
[33] Y. Politi, T. Arad, E. Klein, S. Weiner, L. Addadi, *Science* **2004**, *306*, 1161.
[34] M. Nemoto, K. Okada, H. Akamine, Y. Odagaki, Y. Narahara, K. Okoshi, K. Obuse, D. Kisailus, H. Moriya, A. Satoh, **2024**.
[35] W. Huang, D. Restrepo, J.-Y. Jung, F. Y. Su, Z. Liu, R. O. Ritchie, J. McKittrick, P. Zavattieri, D. Kisailus, *Adv. Mater.* **2019**, *31*, 1901561.
[36] W. Huang, D. Montroni, T. Wang, S. Murata, A. Arakaki, M. Nemoto, D. Kisailus, *Acc. Chem. Res.* **2022**, *55*, 1360.
[37] M. Nemoto, D. Ren, S. Herrera, S. Pan, T. Tamura, K. Inagaki, D. Kisailus, *Sci. Rep.* **2019**, *9*, 856.
[38] Q. Wang, M. Nemoto, D. Li, J. C. Weaver, B. Weden, J. Stegemeier, K. N. Bozhilov, L. R. Wood, G. W. Milliron, C. S. Kim, E. DiMasi, D. Kisailus, *Adv. Funct. Mater.* **2013**, *23*, 2908.
[39] N. A. Yaraghi, D. Kisailus, *Annu. Rev. Phys. Chem.* **2018**, *69*, 23.
[40] M. Nemoto, Q. Wang, D. Li, S. Pan, T. Matsunaga, D. Kisailus, *Proteomics* **2012**, *12*, 2890.
[41] J. C. Weaver, J. Aizenberg, G. E. Fantner, D. Kisailus, A. Woesz, P. Allen, K. Fields, M. J. Porter, F. W. Zok, P. K. Hansma, P. Fratzl, D. E. Morse, *J. Struct. Biol.* **2007**, *158*, 93.
[42] L. A. Estroff, *Chem. Rev.* **2008**, *108*, 4329.
[43] S. Murata, J. Rivera, M. Y. Noh, N. Hiyoshi, W. Yang, D. Y. Parkinson, H. S. Barnard, Y. Arakane, D. Kisailus, A. Arakaki, *Acta Biomater.* **2022**, *140*, 467.
[44] D. Kisailus, M. Nemoto, *Biol. Magn. Mater. Appl.* **2018**, 53.
[45] P. U. P. A. Gilbert, K. D. Bergmann, N. Boekelheide, S. Tambutté, T. Mass, F. Marin, J. F. Adkins, J. Erez, B. Gilbert, V. Knutson, M. Cantine, J. O. Hernández, A. H. Knoll, *Sci. Adv.* **2022**, *8*, abl9653.
[46] H. Ehrlich, E. Bailey, M. Wysokowski, T. Jesionowski, *Biomimetics* **2021**, *6*, 46.
[47] H. A. Lowenstam, S. Weiner, *On Biomineralization*, Oxford University Press, New York **1989**.
[48] G. Campli, O. Volovych, K. Kim, W. P. Veldsman, H. B. Drage, I. Sheizaf, S. Lynch, A. D. Chipman, A. C. Daley, M. Robinson-Rechavi, R. M. Waterhouse, *Biol. Rev.* **2024**, *99*, 2338.
[49] A. Arnold, E. Dennison, C. S. Kovacs, M. Mannstadt, R. Rizzoli, M. L. Brandi, B. Clarke, R. V. Thakker, *Nat. Rev. Endocrinol.* **2021**, *17*, 261.
[50] S. Weiner, L. Addadi, *Annu. Rev. Mater. Res.* **2011**, *41*, 21.
[51] N. Vidavsky, J. A. M. R. Kunitake, L. A. Estroff, *Adv. Healthcare Mater.* **2021**, *10*, 2001271.
[52] K. Kahil, S. Weiner, L. Addadi, A. Gal, *J. Am. Chem. Soc.* **2021**, *143*, 21100.
[53] K. Qin, Z. Zheng, J. Wang, H. Pan, R. Tang, *Giant* **2024**, *19*, 100317.
[54] U. G. K. Wegst, H. Bai, E. Saiz, A. P. Tomsia, R. O. Ritchie, *Nat. Mater.* **2015**, *14*, 23.
[55] P. Tao, W. Shang, C. Song, Q. Shen, F. Zhang, Z. Luo, N. Yi, D. Zhang, T. Deng, *Adv. Mater.* **2015**, *27*, 428.
[56] Q. Zhao, Y. Wang, H. Cui, X. Du, *J. Mater. Chem. C* **2019**, *7*, 6493.
[57] M. E. McConney, K. D. Anderson, L. L. Brott, R. R. Naik, V. V. Tsukruk, *Adv. Funct. Mater.* **2009**, *19*, 2527.
[58] H. Fan, J. P. Gong, *Adv. Mater.* **2021**, *33*, 2102983.
[59] Y. Zhang, Z. Liu, Y. Xu, J. Li, S. Q. Shi, J. Li, Q. Gao, *Chem. Eng. J.* **2021**, *426*, 130852.
[60] Y. Wang, E. J. Jeon, J. Lee, H. Hwang, S. Cho, H. Lee, *Adv. Mater.* **2020**, *32*, 2002118.
[61] J. C. Cremaldi, B. Bhushan, *Beilstein J. Nanotechnol.* **2018**, *9*, 907.
[62] E. D'Elia, S. Eslava, M. Miranda, T. K. Georgiou, E. Saiz, *Sci. Rep.* **2016**, *6*, 25059.
[63] H. Wang, Y. Yang, L. Guo, *Adv. Energy Mater.* **2017**, *7*, 1601709.
[64] M. Li, C. Li, B. R. K. Blackman, E. Saiz, *Matter* **2021**, *4*, 3400.

[65] J. Mei, T. Liao, H. Peng, Z. Sun, *Small Methods* **2022**, *6*, 2101076.
[66] A. H. Proppe, Y. C. Li, A. Aspuru-Guzik, C. P. Berlinguette, C. J. Chang, R. Cogdell, A. G. Doyle, J. Flick, N. M. Gabor, R. Van Grondelle, S. Hammes-Schiffer, S. A. Jaffer, S. O. Kelley, M. Leclerc, K. Leo, T. E. Mallouk, P. Narang, G. S. Schlau-Cohen, G. D. Scholes, A. Vojvodic, V. W.-W. Yam, J. Y. Yang, E. H. Sargent, *Nat. Rev. Mater.* **2020**, *5*, 828.
[67] V. Artero, *Nat. Energy* **2017**, *2*.
[68] J. A. Finbloom, C. Huynh, X. Huang, T. A. Desai, *Nat. Rev. Bioeng.* **2023**, *1*, 139.
[69] J. Ju, Y. Zheng, L. Jiang, *Acc. Chem. Res.* **2014**, *47*, 2342.
[70] Y. Cui, D. Li, H. Bai, *Ind. Eng. Chem. Res.* **2017**, *56*, 4887.
[71] Q. Tong, N. Qiu, J. Ji, L. Ye, G. Zhai, *Expert Opin. Drug Deliv.* **2020**, *17*, 1269.
[72] M. Monti, S. Rasmussen, *Artif. Life* **2017**, *23*, 552.
[73] B. Su, Y. Tian, L. Jiang, *J. Am. Chem. Soc.* **2016**, *138*, 1727.
[74] Y. Si, Z. Dong, L. Jiang, *ACS Cent. Sci.* **2018**, *4*, 1102.
[75] T. Sun, L. Feng, X. Gao, L. Jiang, *Acc. Chem. Res.* **2005**, *38*, 644.
[76] X. Liu, S. Wang, *Chem. Soc. Rev.* **2014**, *43*, 2385.
[77] T. Xu, L.-P. Xu, X. Zhang, S. Wang, *Chem. Soc. Rev.* **2019**, *48*, 3153.
[78] D. Nepal, S. Kang, K. M. Adstedt, K. Kanhaiya, M. R. Bockstaller, L. C. Brinson, M. J. Buehler, P. V. Coveney, K. Dayal, J. A. El-Awady, L. C. Henderson, D. L. Kaplan, S. Keten, N. A. Kotov, G. C. Schatz, S. Vignolini, F. Vollrath, Y. Wang, B. I. Yakobson, V. V. Tsukruk, H. Heinz, *Nat. Mater.* **2023**, *22*, 18.
[79] N. H. Cho, A. Guerrero-Martínez, J. Ma, S. Bals, N. A. Kotov, L. M. Liz-Marzán, K. T. Nam, *Nat. Rev. Bioeng.* **2023**, *1*, 88.
[80] J. Du, D. Katti, H. Heinz, *JOM* **2021**, *73*, 1673.
[81] J. Du, D. Katti, H. Heinz, *JOM* **2021**, *73*, 2332.
[82] G. Zan, Q. Wu, *Adv. Mater.* **2016**, *28*, 2099.
[83] W. Wang, S. Wang, *Lab Chip* **2022**, *22*, 1042.
[84] W. Huang, M. Shishehbor, N. Guarín-Zapata, N. D. Kirchhofer, J. Li, L. Cruz, T. Wang, S. Bhowmick, D. Stauffer, P. Manimunda, K. N. Bozhilov, R. Caldwell, P. Zavattieri, D. Kisailus, *Nat. Mater.* **2020**, *19*, 1236.
[85] X. Zhang, W. Huang, J. Yu, C. Zhao, Y. Si, *Adv. Funct. Mater.* **2025**, *35*, 2416857.
[86] K. S. Katti, D. R. Katti, *Mater. Sci. Eng. C* **2006**, *26*, 1317.
[87] L. P. Biró, K. Kertész, E. Horváth, G. I. Márk, G. Molnár, Z. Vértesy, J.-F. Tsai, A. Kun, Z.s. Bálint, J. P. Vigneron, *J. R. Soc. Interface* **2010**, *7*, 887.
[88] X. Chen, C. Wang, E. Baker, C. Sun, *Sci. Rep.* **2015**, *5*, 11977.
[89] J. Sun, X. Wang, J. Wu, C. Jiang, J. Shen, M. A. Cooper, X. Zheng, Y. Liu, Z. Yang, D. Wu, *Sci. Rep.* **2018**, *8*, 5438.
[90] X. Xiao, G. Wu, L. Liu, K. Dong, Y. Gu, *Mater. Today Proc.* **2019**, *16*, 1380.
[91] K. Lin, S. Chen, Y. Zeng, T. C. Ho, Y. Zhu, X. Wang, F. Liu, B. Huang, C. Y.-H. Chao, Z. Wang, C. Y. Tso, *Science* **2023**, *382*, 691.
[92] Y. Ke, Q. Zhang, T. Wang, S. Wang, N. Li, G. Lin, X. Liu, Z. Dai, J. Yan, J. Yin, S. Magdassi, D. Zhao, Y. Long, *Nano Energy* **2020**, *73*, 104785.
[93] H. Bousack, T. Kahl, A. Schmitz, H. Schmitz, *Micromachines* **2015**, *6*, 718.
[94] T. Sakurai, *Front. Physiol.* **2014**, *5*, 125
[95] G. Thomas, V. Keller, D. Spitzer, *Appl. Mater. Today* **2022**, *29*, 101667.
[96] M. E. McConney, C. F. Schaber, M. D. Julian, F. G. Barth, V. V. Tsukruk, *J. R. Soc. Interface* **2007**, *4*, 1135.
[97] D. Kang, P. V. Pikhitsa, Y. W. Choi, C. Lee, S. S. Shin, L. Piao, B. Park, K.-Y. Suh, T. Kim, M. Choi, *Nature* **2014**, *516*, 222.
[98] Y. Liu, D. Luo, T. Wang, *Small* **2016**, *12*, 4611.
[99] A. Rodriguez-Palomo, M. Østergaard, H. Birkedal, *Adv. Funct. Mater.* **2024**, *34*, 2307026.
[100] J. Sun, B. Bhushan, *RSC Adv.* **2012**, *2*, 7617.
[101] L. Li, J. C. Weaver, C. Ortiz, *Nat. Commun.* **2015**, *6*, 6216.
[102] E. D. Yilmaz, G. A. Schneider, M. V. Swain, *Philos. Trans. R. Soc. Math. Phys. Eng. Sci.* **2015**, *373*, 20140130.
[103] F.-Z. Cui, J. Ge, *J. Tissue Eng. Regener. Med.* **2007**, *1*, 185.
[104] M. A. Meyers, J. McKittrick, P.-Y. Chen, *Science* **2013**, *339*, 773.
[105] P.-Y. Chen, J. McKittrick, M. A. Meyers, *Prog. Mater. Sci.* **2012**, *57*, 1492.
[106] P.-Y. Chen, A. Y. M. Lin, Y.-S. Lin, Y. Seki, A. G. Stokes, J. Peyras, E. A. Olevsky, M. A. Meyers, J. McKittrick, *J. Mech. Behav. Biomed. Mater.* **2008**, *1*, 208.
[107] P. Fratzl, R. Weinkamer, *Prog. Mater. Sci.* **2007**, *52*, 1263.
[108] J. Pelleg, *Mechanical Properties of Ceramics*, Springer International Publishing, Cham, **2014**.
[109] B. Tang, S. Niu, J. Yang, C. Shao, M. Wang, J. Ni, X. Zhang, X. Yang, *Biomimetics* **2022**, *7*, 120.
[110] P. Fratzl, H. S. Gupta, F. D. Fischer, O. Kolednik, *Adv. Mater.* **2007**, *19*, 2657.
[111] M. Y. He, A. G. Evans, J. W. Hutchinson, *Int. J. Solids Struct.* **1994**, *31*, 3443.
[112] V. Perricone, E. Sarmiento, A. Nguyen, N. C. Hughes, D. Kisailus, *Commun. Mater.* **2024**, *5*, 227.
[113] H. Ming-Yuan, J. W. Hutchinson, *Int. J. Solids Struct.* **1989**, *25*, 1053.
[114] O. Kolednik, J. Predan, F. D. Fischer, P. Fratzl, *Adv. Funct. Mater.* **2011**, *21*, 3634.
[115] Y. Al-Douri, in *Nanomaterials: Basics to Applications* (Ed.: Y. Al-Douri), Springer Nature, Singapore, **2022**, pp. 1–22.
[116] J. J. De Yoreo, P. U. P. A. Gilbert, N. A. J. M. Sommerdijk, R. L. Penn, S. Whitelam, D. Joester, H. Zhang, J. D. Rimer, A. Navrotsky, J. F. Banfield, A. F. Wallace, F. M. Michel, F. C. Meldrum, H. Cölfen, P. M. Dove, *Science* **2015**, *349*, aaa6760.
[117] S. N. Patek, R. L. Caldwell, *J. Exp. Biol.* **2005**, *208*, 3655.
[118] R. L. Caldwell, H. Dingle, *Naturwissenschaften* **1975**, *62*, 214.
[119] J.-H. Lee, L. Wang, M. C. Boyce, E. L. Thomas, *Nano Lett.* **2012**, *12*, 4392.
[120] R. M. Cywar, N. A. Rorrer, C. B. Hoyt, G. T. Beckham, E. Y.-X. Chen, *Nat. Rev. Mater.* **2022**, *7*, 83.
[121] M. Pääkkö, M. Ankerfors, H. Kosonen, A. Nykänen, S. Ahola, M. Österberg, J. Ruokolainen, J. Laine, P. T. Larsson, O. Ikkala, T. Lindström, *Biomacromolecules* **2007**, *8*, 1934.
[122] W. Yang, V. R. Sherman, B. Gludovatz, E. Schaible, P. Stewart, R. O. Ritchie, M. A. Meyers, *Nat. Commun.* **2015**, *6*, 6649.
[123] W. Huang, A. Zaheri, J.-Y. Jung, H. D. Espinosa, J. Mckittrick, *Acta Biomater.* **2017**, *64*, 1.
[124] W. Huang, A. Zaheri, W. Yang, D. Kisailus, R. O. Ritchie, H. Espinosa, J. McKittrick, *Adv. Funct. Mater.* **2019**, *29*, 1901077.
[125] B. Thomas, M. C. Raj, A. K. B, R. M. H, J. Joy, A. Moores, G. L. Drisko, C. Sanchez, *Chem. Rev.* **2018**, *118*, 11575.
[126] D. Trache, A. F. Tarchoun, M. Derradji, T. S. Hamidon, N. Masruchin, N. Brosse, M. H. Hussin, *Front. Chem.* **2020**, *8*, 392.
[127] X. Yang, L. A. Berglund, *Adv. Mater.* **2021**, *33*, 2001118.
[128] F. Barthelat, Z. Yin, M. J. Buehler, *Nat. Rev. Mater.* **2016**, *1*, 16007.
[129] K. Jin, Z. Qin, M. J. Buehler, *J. Mech. Behav. Biomed. Mater.* **2015**, *42*, 198.
[130] R. L. Reis, S. Weiner, *Learning from Nature How to Design New Implantable Biomaterials: From Biomineralization Fundamentals to Biomimetic Materials and Processing Routes: Proceedings of the NATO Advanced Study Institute, Held in Alvor, Algarve, Portugal, 13-24 October 2003*, Springer Science & Business Media, Cham **2004**.
[131] Y. Nishiyama, P. Langan, H. Chanzy, *J. Am. Chem. Soc.* **2002**, *124*, 9074.
[132] R. J. Moon, A. Martini, J. Nairn, J. Simonsen, J. Youngblood, *Chem. Soc. Rev.* **2011**, *40*, 3941.
[133] W. Huang, D. Restrepo, J. Jung, F. Y. Su, Z. Liu, R. O. Ritchie, J. McKittrick, P. Zavattieri, D. Kisailus, *Adv. Mater.* **2019**, *31*, 1901561.

[134] S. Ghasemi, P. Rahimzadeh-Bajgiran, M. Tajvidi, S. M. Shaler, *Cellulose* **2020**, *27*, 677.
[135] L. M. Mariani, G. S. Vankayalapati, J. M. Considine, K. T. Turner, in *Mechanics of Biological Systems and Materials & Micro- and Nanomechanics*, Vol. *4*, (Ed.: M. E. Grady), Springer International Publishing, Cham **2020**, pp. 25-28.
[136] D. Raabe, P. Romano, C. Sachs, H. Fabritius, A. Al-Sawalmih, S.-B. Yi, G. Servos, H. G. Hartwig, *Mater. Sci. Eng. A* **2006**, *421*, 143.
[137] L. K. Grunenfelder, S. Herrera, D. Kisailus, *Small* **2014**, *10*, 3207.
[138] H. Merzendorfer, L. Zimoch, *J. Exp. Biol.* **2003**, *206*, 4393.
[139] D. Montroni, F. Sparla, S. Fermani, G. Falini, *Acta Biomater.* **2021**, *120*, 81.
[140] B. Moussian, in *Targeting Chitin-Containing Organisms* (Eds.: Q. Yang, T. Fukamizo), Springer Singapore, Singapore **2019**, pp. 5–18.
[141] M. Y. Noh, S. Muthukrishnan, K. J. Kramer, Y. Arakane, *Insect Biochem. Mol. Biol.* **2017**, *91*, 21.
[142] J. F. V. Vincent, U. G. K. Wegst, *Arthropod Struct. Dev.* **2004**, *33*, 187.
[143] Q. Meng, Q. Zhang, X. Shi, *J. Am. Ceram. Soc.* **2025**, *108*, 20465.
[144] B. Pokroy, E. Zolotoyabko, *J. Mater. Chem.* **2003**, *13*, 682.
[145] S. Younis, Y. Kauffmann, B. Pokroy, E. Zolotoyabko, *J. Struct. Biol.* **2012**, *180*, 539.
[146] C. Salinas, D. Kisailus, *JOM* **2013**, *65*, 473.
[147] C. L. Salinas, E. E. de Obaldia, C. Jeong, J. Hernandez, P. Zavattieri, D. Kisailus, *J. Mech. Behav. Biomed. Mater.* **2017**, *76*, 58.
[148] Y. A. Shin, S. Yin, X. Li, S. Lee, S. Moon, J. Jeong, M. Kwon, S. J. Yoo, Y.-M. Kim, T. Zhang, H. Gao, S. H. Oh, *Nat. Commun.* **2016**, *7*, 10772.
[149] S. Kamat, H. Kessler, R. Ballarini, M. Nassirou, A. H. Heuer, *Acta Mater.* **2004**, *52*, 2395.
[150] S. Kamat, X. Su, R. Ballarini, A. H. Heuer, *Nature* **2000**, *405*, 1036.
[151] I. Almagro, J. H. E. Cartwright, A. G. Checa, E. Macías-Sánchez, C. I. Sainz-Díaz, *Acta Biomater.* **2021**, *120*, 12.
[152] L. T. Kuhn-Spearing, H. Kessler, E. Chateau, R. Ballarini, A. H. Heuer, S. M. Spearing, *J. Mater. Sci.* **1996**, *31*, 6583.
[153] F. Barthelat, H. Tang, P. D. Zavattieri, C.-M. Li, H. D. Espinosa, *J. Mech. Phys. Solids* **2007**, *55*, 306.
[154] L. Brooker, J. Shaw, in *Advanced Topics in Biomineralization* (Ed.: J. Seto), InTech, London, UK **2012**.
[155] L. K. Grunenfelder, E. E. De Obaldia, Q. Wang, D. Li, B. Weden, C. Salinas, R. Wuhrer, P. Zavattieri, D. Kisailus, *Adv. Funct. Mater.* **2014**, *24*, 6093.
[156] E. E. de Obaldia, C. Jeong, L. K. Grunenfelder, D. Kisailus, P. Zavattieri, *J. Mech. Behav. Biomed. Mater.* **2015**, *48*, 70.
[157] E. E. de Obaldia, S. Herrera, L. K. Grunenfelder, D. Kisailus, P. Zavattieri, *J. Mech. Phys. Solids* **2016**, *96*, 511.
[158] J. A. Shaw, D. J. Macey, L. R. Brooker, P. L. Clode, *Biol. Bull.* **2010**, *218*, 132.
[159] D. Montroni, E. Sarmiento, R. Zhao, P. S. Dasika, J. M. Connolly, R. Wuhrer, Y. Zhang, M. Zhernenkov, T. Wang, B. P. Ramirez-Santana, L. Sheppard, O. H. Avila-Poveda, A. Arakaki, M. Nemoto, P. Zavattieri, D. Kisailus, *Adv. Funct. Mater.* **2024**, *34*, 2401658.
[160] T. Wang, W. Huang, C. H. Pham, S. Murata, S. Herrera, N. D. Kirchhofer, B. Arkook, D. Stekovic, M. E. Itkis, N. Goldman, L. Zepeda-Ruiz, G. Freychet, M. Zhernenkov, M. Nemoto, A. Arakaki, D. Kisailus, *Small Struct.* **2022**, *3*, 2100202.
[161] M. Saunders, C. Kong, J. A. Shaw, D. J. Macey, P. L. Clode, *J. Struct. Biol.* **2009**, *167*, 55.
[162] J. D. Curry, *Proc. R. Soc. Lond. B Biol. Sci.* **1977**, *196*, 443.
[163] X. Li, W.-C. Chang, Y. J. Chao, R. Wang, M. Chang, *Nano Lett.* **2004**, *4*, 613.
[164] F. Barthelat, C.-M. Li, C. Comi, H. D. Espinosa, *J. Mater. Res.* **2006**, *21*, 1977.
[165] F. Barthelat, D. Zhu, *J. Mater. Res.* **2011**, *26*, 1203.
[166] Z. Huang, H. Li, Z. Pan, Q. Wei, Y. J. Chao, X. Li, *Sci. Rep.* **2011**, *1*, 148.
[167] S. Weiner, W. Traub, *Philos. Trans. R. Soc. Lond. B Biol. Sci.* **1997**, *304*, 425.
[168] Y. Levi-Kalisman, G. Falini, L. Addadi, S. Weiner, *J. Struct. Biol.* **2001**, *135*, 8.
[169] F. Nudelman, *Semin. Cell Dev. Biol.* **2015**, *46*, 2.
[170] A. G. Checa, J. H. E. Cartwright, M.-G. Willinger, *J. Struct. Biol.* **2011**, *176*, 330.
[171] X. Li, Z.-H. Xu, R. Wang, *Nano Lett.* **2006**, *6*, 2301.
[172] C. Ortiz, M. C. Boyce, *Science* **2008**, *319*, 1053.
[173] R. Z. Wang, Z. Suo, A. G. Evans, N. Yao, I. A. Aksay, *J. Mater. Res.* **2001**, *16*, 2485.
[174] H. D. Espinosa, J. E. Rim, F. Barthelat, M. J. Buehler, *Prog. Mater. Sci.* **2009**, *54*, 1059.
[175] S. Nikolov, M. Petrov, L. Lymperakis, M. Friák, C. Sachs, H. Fabritius, D. Raabe, J. Neugebauer, *Adv. Mater.* **2010**, *22*, 519.
[176] J. C. Weaver, G. W. Milliron, A. Miserez, K. Evans-Lutterodt, S. Herrera, I. Gallana, W. J. Mershon, B. Swanson, P. Zavattieri, E. DiMasi, D. Kisailus, *Science* **2012**, *336*, 1275.
[177] J. Rivera, M. S. Hosseini, D. Restrepo, S. Murata, D. Vasile, D. Y. Parkinson, H. S. Barnard, A. Arakaki, P. Zavattieri, D. Kisailus, *Nature* **2020**, *586*, 543.
[178] S. Amini, M. Tadayon, S. Idapalapati, A. Miserez, *Nat. Mater.* **2015**, *14*, 943.
[179] N. Suksangpanya, N. A. Yaraghi, D. Kisailus, P. Zavattieri, *J. Mech. Behav. Biomed. Mater.* **2017**, *76*, 38.
[180] N. Suksangpanya, N. A. Yaraghi, R. B. Pipes, D. Kisailus, P. Zavattieri, *Int. J. Solids Struct.* **2018**, *150*, 83.
[181] D. Raabe, A. Al-Sawalmih, S. B. Yi, H. Fabritius, *Acta Biomater.* **2007**, *3*, 882.
[182] B. Moussian, in *Targeting Chitin-Containing Organisms* (Eds.: Q. Yang, T. Fukamizo), Springer, Singapore **2019**, pp. 5–18.
[183] N. A. Yaraghi, N. Guarín-Zapata, L. K. Grunenfelder, E. Hintsala, S. Bhowmick, J. M. Hiller, M. Betts, E. L. Principe, J.-Y. Jung, L. Sheppard, R. Wuhrer, J. McKittrick, P. D. Zavattieri, D. Kisailus, *Adv. Mater.* **2016**, *28*, 6835.
[184] B. Zhang, X. Peng, Z. Mu, S. Niu, Z. Han, L. Ren, *Adv. Funct. Mater.* **2024**, *34*, 2311666.
[185] B. Zhang, J. Yang, Y. Li, J. Zhang, S. Niu, Z. Han, L. Ren, *Int. J. Mech. Sci.* **2023**, *244*, 108073.
[186] N. A. Yaraghi, N. Guarín-Zapata, L. K. Grunenfelder, E. Hintsala, S. Bhowmick, J. M. Hiller, M. Betts, E. L. Principe, J. Jung, L. Sheppard, R. Wuhrer, J. McKittrick, P. D. Zavattieri, D. Kisailus, *Adv. Mater.* **2016**, *28*, 6835.
[187] L. K. Grunenfelder, G. Milliron, S. Herrera, I. Gallana, N. Yaraghi, N. Hughes, K. Evans-Lutterodt, P. Zavattieri, D. Kisailus, *Adv. Mater.* **2018**, *30*, 1705295.
[188] B. Chen, X. Peng, C. Cai, H. Niu, X. Wu, *Mater. Sci. Eng. A* **2006**, *423*, 237.
[189] A. Mendoza-Galván, L. F. del Río, K. Järrendahl, H. Arwin, *Sci. Rep.* **2018**, *8*, 6456.
[190] I. Kellersztein, S. R. Cohen, B. Bar-On, H. D. Wagner, *Acta Biomater.* **2019**, *94*, 565.
[191] I. Greenfeld, I. Kellersztein, H. D. Wagner, *Nat. Commun.* **2020**, *11*, 224.
[192] I. Kellersztein, I. Greenfeld, H. D. Wagner, *Bioinspir. Biomim.* **2021**, *16*, 026013.
[193] D. Raabe, C. Sachs, P. Romano, *Acta Mater.* **2005**, *53*, 4281.
[194] H.-O. Fabritius, C. Sachs, P. R. Triguero, D. Raabe, *Adv. Mater.* **2009**, *21*, 391.
[195] J. G. Kunkel, M. Rosa, A. N. Bahadur, *Fish. Res.* **2017**, *186*, 372.
[196] P. Rawat, D. Zhu, M. Z. Rahman, F. Barthelat, *Acta Biomater.* **2021**, *121*, 41.

[197] S. Yin, R. Yang, Y. Huang, W. Guo, D. Chen, W. Zhang, M. Ren, Y. Zhou, J. Xu, *Compos. Sci. Technol.* **2021**, *205*, 108650.
[198] W. Yang, V. R. Sherman, B. Gludovatz, M. Mackey, E. A. Zimmermann, E. H. Chang, E. Schaible, Z. Qin, M. J. Buehler, R. O. Ritchie, M. A. Meyers, *Acta Biomater.* **2014**, *10*, 3599.
[199] V. R. Sherman, H. Quan, W. Yang, R. O. Ritchie, M. A. Meyers, *J. Mech. Behav. Biomed. Mater.* **2017**, *73*, 1.
[200] E. A. Zimmermann, B. Gludovatz, E. Schaible, N. K. N. Dave, W. Yang, M. A. Meyers, R. O. Ritchie, *Nat. Commun.* **2013**, *4*, 2634.
[201] J. P. Grierson, A. C. Neville, *Tissue Cell* **1981**, *13*, 819.
[202] T. van de Kamp, H. Greven, *Entomol. Heute* **2010**, *22*, 191.
[203] H. Quan, W. Yang, E. Schaible, R. O. Ritchie, M. A. Meyers, *Adv. Funct. Mater.* **2018**, *28*, 1804237.
[204] C. E. Hamm, R. Merkel, O. Springer, P. Jurkojc, C. Maier, K. Prechtel, V. Smetacek, *Nature* **2003**, *421*, 841.
[205] J. Aizenberg, J. C. Weaver, M. S. Thanawala, V. C. Sundar, D. E. Morse, P. Fratzl, *Science* **2005**, *309*, 275.
[206] K. Sato, N. Ozaki, K. Nakanishi, Y. Sugahara, Y. Oaki, C. Salinas, S. Herrera, D. Kisailus, H. Imai, *RSC Adv.* **2017**, *7*, 13065.
[207] J. D. Wehr, R. G. Sheath, J. P. Kociolek, *Freshwater Algae of North America: Ecology and Classification*, Elsevier, Cham **2015**.
[208] W. Fu, Y. Shu, Z. Yi, Y. Su, Y. Pan, F. Zhang, S. Brynjolfsson, *Sustain. Horiz.* **2022**, *2*, 100015.
[209] Z. H. Aitken, S. Luo, S. N. Reynolds, C. Thaulow, J. R. Greer, *Proc. Natl. Acad. Sci. USA* **2016**, *113*, 2017.
[210] M. Hildebrand, E. York, J. I. Kelz, A. K. Davis, L. G. Frigeri, D. P. Allison, M. J. Doktycz, *J. Mater. Res.* **2006**, *21*, 2689.
[211] M. Pančić, R. R. Torres, R. Almeda, T. Kiørboe, *Proc. R. Soc. B Biol. Sci.* **2019**, *286*, 20190184.
[212] L. Friedrichs, M. Hörnig, L. Schulze, A. Bertram, S. Jansen, C. Hamm, *Mar. Ecol. Prog. Ser.* **2013**, *481*, 41.
[213] S. W. Fowler, N. S. Fisher, *Deep Sea Res. Part Oceanogr. Res. Pap.* **1983**, *30*, 963.
[214] M. Hildebrand, *Chem. Rev.* **2008**, *108*, 4855.
[215] K. Thamatrakoln, M. Hildebrand, *Plant Physiol.* **2008**, *146*, 1397.
[216] F. Noll, M. Sumper, N. Hampp, *Nano Lett.* **2002**, *2*, 91.
[217] M. Sumper, E. Brunner, *Adv. Funct. Mater.* **2006**, *16*, 17.
[218] A.-M. M. Schmid, D. Schulz, *Protoplasma* **1979**, *100*, 267.
[219] E. G. Vrieling, W. W. C. Gieskes, T. P. M. Beelen, *J. Phycol.* **1999**, *35*, 548.
[220] C. Heintze, P. Formanek, D. Pohl, J. Hauptstein, B. Rellinghaus, N. Kröger, *BMC Mater.* **2020**, *2*, 11.
[221] S. Luo, J. R. Greer, *Adv. Eng. Mater.* **2018**, *20*, 1800301.
[222] M. B. Dickerson, K. H. Sandhage, R. R. Naik, *Chem. Rev.* **2008**, *108*, 4935.
[223] M. Sumper, S. Lorenz, E. Brunner, *Angew. Chem., Int. Ed.* **2003**, *42*, 5192.
[224] M. Sumper, *Science* **2002**, *295*, 2430.
[225] L. R. Meza, A. J. Zelhofer, N. Clarke, A. J. Mateos, D. M. Kochmann, J. R. Greer, *Proc. Natl. Acad. Sci. USA* **2015**, *112*, 11502.
[226] A. Witkowski, M. Ashworth, C. Li, I. Sagna, D. Yatte, E. Górecka, A. O. R. Franco, W.-H. Kusber, G. Klein, H. Lange-Bertalot, P. Dąbek, E. C. Theriot, S. R. Manning, *Protist* **2020**, *171*, 125713.
[227] M. C. Fernandes, J. Aizenberg, J. C. Weaver, K. Bertoldi, *Nat. Mater.* **2021**, *20*, 237.
[228] H. Chen, Z. Jia, L. Li, *J. Mech. Behav. Biomed. Mater.* **2022**, *135*, 105448.
[229] J. N. Cha, K. Shimizu, Y. Zhou, S. C. Christiansen, B. F. Chmelka, G. D. Stucky, D. E. Morse, *Proc. Natl. Acad. Sci. USA* **1999**, *96*, 361.
[230] S. Morankar, A. S. S. Singaravelu, S. Niverty, Y. Mistry, C. A. Penick, D. Bhate, N. Chawla, *Int. J. Solids Struct.* **2022**, *253*, 111622.
[231] Z. Vangelatos, M. E. Yildizdag, C. P. Grigoropoulos, *Extreme Mech. Lett.* **2023**, *61*, 102013.
[232] D. Ciprari, K. Jacob, R. Tannenbaum, *Macromolecules* **2006**, *39*, 6565.
[233] J. Huang, J. Zhou, M. Liu, *JACS Au* **2022**, *2*, 280.
[234] N. Raoux, A. Benelfellah, N. AÏT Hocine, *Polym. Adv. Technol.* **2024**, *35*, 6620.
[235] J. Karger-Kocsis, H. Mahmood, A. Pegoretti, *Prog. Mater. Sci.* **2015**, *73*, 1.
[236] T. Hao, W. Huang, N. Guarín-Zapata, D. Lublin, Y. Chen, H. Yu, L. Shyamsunder, P. Zavattieri, D. Kisailus, *Adv. Funct. Mater.* **2025**, *35*, 2417291.
[237] C. J. R. Verbeek, *J. Thermoplast. Compos. Mater.* **2007**, *20*, 137.
[238] E. Senses, P. Akcora, *Macromolecules* **2013**, *46*, 1868.
[239] A. K. Naskar, J. K. Keum, R. G. Boeman, *Nat. Nanotechnol.* **2016**, *11*, 1026.
[240] G. C. Pradhan, S. Dash, S. K. Swain, *Carbohydr. Polym.* **2015**, *134*, 60.
[241] L. Paglia, C. Mapelli, V. Genova, M. P. Bracciale, F. Marra, C. Bartuli, I. Fratoddi, G. Pulci, *Polym. Compos.* **2022**, *43*, 7345.
[242] W. K. Darkwah, A. B. Appiagyei, J. B. Puplampu, *ACS Omega* **2023**, *8*, 34215.
[243] T. Hanemann, D. V. Szabó, *Materials* **2010**, *3*, 3468.
[244] S. Mousavian, H. Ebadi-Dehaghani, D. Ashouri, H. Sadeghipour, F. Jabbari, *J. Polym. Res.* **2012**, *19*, 9991.
[245] M.-H. Chan, C.-H. Li, Y.-C. Chang, M. Hsiao, *Pharmaceutics* **2022**, *14*, 2584.
[246] G. Alva, Y. Lin, G. Fang, *Mater. Chem. Phys.* **2018**, *205*, 401.
[247] O. Rac-Rumijowska, H. Teterycz, *Materials* **2023**, *16*, 3085.
[248] S. Ippili, J.-S. Jung, A. M. Thomas, V.-H. Vuong, J.-M. Lee, M. S. Sha, K. K. Sadasivuni, V. Jella, S.-G. Yoon, *Polymers* **2023**, *15*, 3791.
[249] A. C. Pinho, A. P. Piedade, *Polymers* **2020**, *12*, 2469.
[250] A. M. M. Essa, M. K. Khallaf, *BMC Microbiol.* **2016**, *16*, 144.
[251] Ľ. Hodásová, A. G. Morena, T. Tzanov, G. Fargas, L. Llanes, C. Alemán, E. Armelin, *ACS Appl. Bio Mater.* **2022**, *5*, 4803.
[252] R. Halabian, K. Moridi, M. Korani, M. Ghollasi, *Int. J. Mol. Cell. Med.* **2019**, *8*, 24.
[253] A. Bagchi, S. R. K. Meka, B. N. Rao, K. Chatterjee, *Nanotechnology* **2014**, *25*, 485101.
[254] H. Liu, T. J. Webster, *Int. J. Nanomed.* **2010**, *5*, 299.
[255] D. J. Brannum, E. J. Price, D. Villamil, S. Kozawa, M. Brannum, C. Berry, R. Semco, G. E. Wnek, *ACS Appl. Polym. Mater.* **2015**, *1*, 2015
[256] Y. Wang, B. Liu, R. Chen, Y. Wang, Z. Han, C. Wang, L. Weng, *Materials* **2023**, *16*, 4759.
[257] A. Nassar, M. Younis, M. Ismail, E. Nassar, *Polymers* **2022**, *14*, 333.
[258] J. Abenojar, Y. Ballesteros, M. Bahrami, M. A. Martínez, J. C. del Real, *Polymers* **2024**, *16*, 878.
[259] E. Omanović-Mikličanin, A. Badnjević, A. Kazlagić, M. Hajlovac, *Health Technol.* **2020**, *10*, 51.
[260] C. C. Lechner, C. F. W. Becker, *Mar. Drugs* **2015**, *13*, 5297.
[261] A. K. Wallace, N. Chanut, C. A. Voigt, *Adv. Funct. Mater.* **2020**, *30*, 2000849.
[262] T. Li, C. Chen, A. H. Brozena, J. Y. Zhu, L. Xu, C. Driemeier, J. Dai, O. J. Rojas, A. Isogai, L. Wågberg, L. Hu, *Nature* **2021**, *590*, 47.
[263] S. Maher, T. Kumeria, M. S. Aw, D. Losic, *Adv. Healthcare Mater.* **2018**, *7*, 1800552.
[264] N. Shadjou, M. Hasanzadeh, *Mater. Sci. Eng. C* **2015**, *55*, 401.
[265] N. Kröger, R. Deutzmann, M. Sumper, *Science* **1999**, *286*, 1129.
[266] L. Senior, M. P. Crump, C. Williams, P. J. Booth, S. Mann, A. W. Perriman, P. Curnow, *J. Mater. Chem. B* **2015**, *3*, 2607.
[267] Y. K. Jo, B.-H. Choi, C. S. Kim, H. J. Cha, *Adv. Mater.* **2017**, *29*, 1704906.
[268] S. Wang, F. Jiang, X. Xu, Y. Kuang, K. Fu, E. Hitz, L. Hu, *Adv. Mater.* **2017**, *29*, 1702498.
[269] Z. Li, C. Chen, R. Mi, W. Gan, J. Dai, M. Jiao, H. Xie, Y. Yao, S. Xiao, L. Hu, *Adv. Mater.* **2020**, *32*, 1906308.
[270] L. Cera, G. M. Gonzalez, Q. Liu, S. Choi, C. O. Chantre, J. Lee, R. Gabardi, M. C. Choi, K. Shin, K. K. Parker, *Nat. Mater.* **2021**, *20*, 242.

[271] L. Stegbauer, P. J. M. Smeets, R. Free, S. G. Wallace, M. C. Hersam, E. E. Alp, D. Joester, *Proc. Natl. Acad. Sci. USA* **2021**, *118*, 2020160118.
[272] D. Montroni, T. Kobayashi, T. Hao, D. Lublin, T. Yoshino, D. Kisailus, *J. Funct. Biomater.* **2022**, *13*, 83.
[273] A. Mucaria, D. Giuri, C. Tomasini, G. Falini, D. Montroni, *Mar. Drugs* **2024**, *22*, 164.
[274] D. Montroni, M. Palanca, K. Morellato, S. Fermani, L. Cristofolini, G. Falini, *Carbohydr. Polym.* **2021**, *251*, 116984.
[275] R. Jayakumar, D. Menon, K. Manzoor, S. V. Nair, H. Tamura, *Carbohydr. Polym.* **2010**, *82*, 227.
[276] J. Lv, X. Lv, M. Ma, D.-H. Oh, Z. Jiang, X. Fu, *Carbohydr. Polym.* **2023**, *299*, 120142.
[277] A. Dev, J. C. Mohan, V. Sreeja, H. Tamura, G. R. Patzke, F. Hussain, S. Weyeneth, S. V. Nair, R. Jayakumar, *Carbohydr. Polym.* **2010**, *79*, 1073.
[278] H. Itoi, G. Saeki, T. Usami, S. Takagi, H. Suzuki, T. Ishii, H. Iwata, Y. Ohzawa, *ACS Sustain. Resour. Manag.* **2024**, *1*, 743.
[279] G. Karambelas, S. Santhanam, Z. N. Wing, *Ceram. Int.* **2013**, *39*, 1315.
[280] L. Chen, R. Ballarini, H. Kahn, A. H. Heuer, *J. Mater. Res.* **2007**, *22*, 124.
[281] G. X. Gu, M. Takaffoli, M. J. Buehler, *Adv. Mater.* **2017**, *29*, 1700060.
[282] L. N. Quan, J. Kang, C.-Z. Ning, P. Yang, *Chem. Rev.* **2019**, *119*, 9153.
[283] W. Liu, S. W. Lee, D. Lin, F. Shi, S. Wang, A. D. Sendek, Y. Cui, *Nat. Energy* **2017**, *2*, 1.
[284] J.-W. Liu, H.-W. Liang, S.-H. Yu, *Chem. Rev.* **2012**, *112*, 4770.
[285] G. Zhou, L. Xu, G. Hu, L. Mai, Y. Cui, *Chem. Rev.* **2019**, *119*, 11042.
[286] S.-C. Zhang, H.-L. Gao, L. Zhang, Y.-B. Zhu, Y.-D. Wu, J.-W. Liu, L.-B. Mao, M. Feng, L. Dong, Z. Pan, X.-S. Meng, Y. Lu, S.-H. Yu, *Precis. Chem.* **2024**, *2*, 634.
[287] M. Cheng, M. Liu, L. Chang, Q. Liu, C. Wang, L. Hu, Z. Zhang, W. Ding, L. Chen, S. Guo, Z. Qi, P. Pan, J. Chen, *Sci. Total Environ.* **2023**, *870*, 161950.
[288] J. Wang, Q. Cheng, L. Lin, L. Jiang, *ACS Nano* **2014**, *8*, 2739.
[289] F. Shahzad, M. Alhabeb, C. B. Hatter, B. Anasori, S. M. Hong, C. M. Koo, Y. Gogotsi, *Science* **2016**, *353*, 1137.
[290] A. Finnemore, P. Cunha, T. Shean, S. Vignolini, S. Guldin, M. Oyen, U. Steiner, *Nat. Commun.* **2012**, *3*, 966.
[291] L. Su, H. Wang, S. Jia, S. Dai, M. Niu, J. Ren, X. Lu, Z. Cai, D. Lu, M. Li, L. Xu, S.-W. Guo, L. Zhuang, K. Peng, *ACS Nano* **2021**, *15*, 18354.
[292] L. Li, Y. Zhou, Y. Gao, X. Feng, F. Zhang, W. Li, B. Zhu, Z. Tian, P. Fan, M. Zhong, H. Niu, S. Zhao, X. Wei, J. Zhu, H. Wu, *Nat. Commun.* **2023**, *14*, 5410.
[293] J. Xue, R. Han, Y. Li, J. Zhang, J. Liu, Y. Yang, *J. Mater. Sci.* **2023**, *58*, 14255.
[294] F. Wang, L. Dou, J. Dai, Y. Li, L. Huang, Y. Si, J. Yu, B. Ding, *Angew. Chem.* **2020**, *132*, 8362.
[295] L. Dou, X. Zhang, X. Cheng, Z. Ma, X. Wang, Y. Si, J. Yu, B. Ding, *ACS Appl. Mater. Interfaces* **2019**, *11*, 29056.
[296] M. Zhang, Y. Wang, Y. Zhang, J. Song, Y. Si, J. Yan, C. Ma, Y.-T. Liu, J. Yu, B. Ding, *Angew. Chem., Int. Ed.* **2020**, *59*, 23252.
[297] X. Zhang, X. Cheng, Y. Si, J. Yu, B. Ding, *ACS Nano* **2022**, *16*, 5487.
[298] H. Wang, L. Cheng, J. Yu, Y. Si, B. Ding, *Nat. Commun.* **2024**, *15*, 336.
[299] X. Cheng, Y.-T. Liu, Y. Si, J. Yu, B. Ding, *Nat. Commun.* **2022**, *13*, 2637.
[300] X. Xu, Q. Zhang, M. Hao, Y. Hu, Z. Lin, L. Peng, T. Wang, X. Ren, C. Wang, Z. Zhao, C. Wan, H. Fei, L. Wang, J. Zhu, H. Sun, W. Chen, T. Du, B. Deng, G. J. Cheng, I. Shakir, C. Dames, T. S. Fisher, X. Zhang, H. Li, Y. Huang, X. Duan, *Science* **2019**, *363*, 723.
[301] Z. Zhu, Y. Liu, Y. Qin, F. Gu, L. Zhuang, H. Yu, Y. Chu, *Nat. Commun.* **2025**, *16*, 4587.
[302] Z. Wang, Q. Luo, Q. Li, G. Sun, *Int. J. Mech. Sci.* **2022**, *219*, 107064.
[303] J. L. Liu, L. Mencattelli, J. Zhi, P. Y. Chua, T.-E. Tay, V. B. C. Tan, *Polymers* **2022**, *14*, 475.
[304] L. K. Grunenfelder, N. Suksangpanya, C. Salinas, G. Milliron, N. Yaraghi, S. Herrera, K. Evans-Lutterodt, S. R. Nutt, P. Zavattieri, D. Kisailus, *Acta Biomater.* **2014**, *10*, 3997.
[305] M. R. Abir, T. E. Tay, H. P. Lee, *Compos. Part Appl. Sci. Manuf.* **2019**, *123*, 59.
[306] J. Rivera, N. A. Yaraghi, W. Huang, D. Gray, D. Kisailus, *J. Mater. Res. Technol.* **2020**, *9*, 14619.
[307] H. Ning, C. Monroe, S. Gibbons, B. Gaskey, P. Flater, *Int. Mater. Rev.* **2024**, *69*, 181.
[308] B. Wetzel, P. Rosso, F. Haupert, K. Friedrich, *Eng. Fract. Mech.* **2006**, *73*, 2375.
[309] Helicoid Industries Inc. signs license agreement with Sports Maska Inc. for new sporting goods products-JEC, **n.d**.
[310] Y. Yang, Z. Chen, X. Song, Z. Zhang, J. Zhang, K. K. Shung, Q. Zhou, Y. Chen, *Adv. Mater.* **2017**, *29*, 1605750.
[311] R. Chen, J. Liu, C. Yang, D. A. Weitz, H. He, D. Li, D. Chen, K. Liu, H. Bai, *ACS Appl. Mater. Interfaces* **2019**, *11*, 23616.
[312] S.-M. Chen, H.-L. Gao, Y.-B. Zhu, H.-B. Yao, L.-B. Mao, Q.-Y. Song, J. Xia, Z. Pan, Z. He, H.-A. Wu, S.-H. Yu, *Natl. Sci. Rev.* **2018**, *5*, 703.
[313] A. Sharma, N. K. Shukla, M.-O. Belarbi, M. Abbas, A. Garg, L. Li, J. Bhutto, A. Bhatia, *Thin-Walled Struct* **2023**, *192*, 111146.
[314] D. Ginzburg, F. Pinto, O. Iervolino, M. Meo, *Compos. Struct.* **2017**, *161*, 187.
[315] J. L. Liu, H. P. Lee, V. B. C. Tan, *Compos. Sci. Technol.* **2018**, *165*, 282.
[316] P. Cui, J. Chen, K. Fu, J. Deng, T. Sun, K. Chen, P. Yin, *ACS Appl. Mater. Interfaces* **2024**, *16*, 53022.
[317] S. Matsumura, S. Kajiyama, T. Nishimura, T. Kato, *Small* **2015**, *11*, 5127.
[318] Y. Habibi, L. A. Lucia, O. J. Rojas, *Chem. Rev.* **2010**, *110*, 3479.
[319] B. Wang, A. Walther, *ACS Nano* **2015**, *9*, 10637.
[320] B. Cantaert, D. Kuo, S. Matsumura, T. Nishimura, T. Sakamoto, T. Kato, *ChemPlusChem* **2017**, *82*, 107.
[321] S. Johnsen, *The Optics of Life: A Biologist's Guide to Light in Nature*, Princeton University Press, Princeton, NJ **2012**.
[322] P. Vukusic, *Curr. Biol.* **2006**, *16*, R621.
[323] G. Britton, *The Biochemistry of Natural Pigments*, Cambridge University Press, New York, **1983**.
[324] S. Kinoshita, S. Yoshioka, J. Miyazaki, *Rep. Prog. Phys.* **2008**, *71*, 076401.
[325] I. C. Cuthill, W. L. Allen, K. Arbuckle, B. Caspers, G. Chaplin, M. E. Hauber, G. E. Hill, N. G. Jablonski, C. D. Jiggins, A. Kelber, J. Mappes, J. Marshall, R. Merrill, D. Osorio, R. Prum, N. W. Roberts, A. Roulin, H. M. Rowland, T. N. Sherratt, J. Skelhorn, M. P. Speed, M. Stevens, M. C. Stoddard, D. Stuart-Fox, L. Talas, E. Tibbetts, T. Caro, *Science* **2017**, *357*, aan0221.
[326] T. Caro, *BioScience* **2005**, *55*, 125.
[327] V. Perricone, C. Santulli, F. Rendina, C. Langella, *Biomimetics* **2021**, *6*, 56.
[328] A. R. Parker, *J. Opt. Pure Appl. Opt.* **2000**, *2*, R15.
[329] G. Donati, *Nat. Photonics* **2016**, *10*, 753.
[330] M. Jacobs, M. Lopez-Garcia, O.-P. Phrathep, T. Lawson, R. Oulton, H. M. Whitney, *Nat. Plants* **2016**, *2*, 16162.
[331] S. Tadepalli, J. M. Slocik, M. K. Gupta, R. R. Naik, S. Singamaneni, *Chem. Rev.* **2017**, *117*, 12705.
[332] S. A. Wainwright, W. D. Biggs, J. D. Currey, J. M. Gosline, *Mechanical Design in Organisms*, Princeton University Press, Princeton, NJ **2020**.
[333] P. Aerts, *Integr. Comp. Biol.* **2013**, *53*, 1015.
[334] J. Sun, B. Bhushan, J. Tong, *RSC Adv.* **2013**, *3*, 14862.
[335] M. D. Shawkey, N. I. Morehouse, P. Vukusic, *J. R. Soc. Interface* **2009**, *6*, S221.
[336] P. Vukusic, J. R. Sambles, C. R. Lawrence, R. J. Wootton, *Proc. R. Soc. Lond. B Biol. Sci.* **1999**, *266*, 1403.
[337] A. Yoshida, M. Motoyama, A. Kosaku, K. Miyamoto, *Zoolog. Sci.* **1997**, *14*, 737.

[338] S. Kinoshita, S. Yoshioka, K. Kawagoe, *Proc. R. Soc. Lond. B Biol. Sci.* **2002**, *269*, 1417.
[339] M. Giraldo, J. Sosa, D. Stavenga, *Biol. Lett.* **2021**, *17*, 20210190.
[340] C. H. Greenewalt, W. Brandt, D. D. Friel, *J. Opt. Soc. Am.* **1960**, *50*, 1005.
[341] J. Sun, W. Wu, L. Tian, W. Li, F. Zhang, Y. Wang, *Sci. Rep.* **2021**, *11*, 808.
[342] E. De Tommasi, *J. Spectrosc.* **2016**, *2016*, 1.
[343] L. De Stefano, P. Maddalena, L. Moretti, I. Rea, I. Rendina, E. De Tommasi, V. Mocella, M. De Stefano, *Superlattices Microstruct.* **2009**, *46*, 84.
[344] M. A. Ferrara, P. Dardano, L. De Stefano, I. Rea, G. Coppola, I. Rendina, R. Congestri, A. Antonucci, M. De Stefano, E. De Tommasi, *PLoS One* **2014**, *9*, 103750.
[345] L. De Stefano, I. Rea, I. Rendina, M. De Stefano, L. Moretti, *Opt. Express* **2007**, *15*, 18082.
[346] M. P. Ashworth, D. W. Lam, M. Lopez-Garcia, S. R. Manning, J. W. Goessling, *Sci. Rep.* **2025**, *15*, 6290.
[347] Z. W. Han, Z. Wang, X. M. Feng, B. Li, Z. Z. Mu, J. Q. Zhang, S. C. Niu, L. Q. Ren, *Biosurface Biotribology* **2016**, *2*, 137.
[348] C. G. Bernhard, W. H. Miller, *Acta Physiol. Scand.* **1962**, *56*, 385.
[349] P. B. Clapham, M. C. Hutley, *Nature* **1973**, *244*, 281.
[350] A. R. Parker, H. E. Townley, *Nat. Nanotechnol.* **2007**, *2*, 347.
[351] A. Blagodatski, A. Sergeev, M. Kryuchkov, Y. Lopatina, V. L. Katanaev, *Proc. Natl. Acad. Sci. USA* **2015**, *112*, 10750.
[352] V. Perricone, T. Grun, P. Raia, C. Langella, *Biomimetics* **2022**, *7*, 89.
[353] A. R. Parker, *Proc. R. Soc. Lond. B Biol. Sci.* **1998**, *265*, 967.
[354] J. P. Vigneron, M. Rassart, C. Vandenbem, V. Lousse, O. Deparis, L. P. Biró, D. Dedouaire, A. Cornet, P. Defrance, *Phys. Rev. E* **2006**, *73*, 041905.
[355] A. Saito, Y. Miyamura, Y. Ishikawa, J. Murase, M. Akai-Kasaya, Y. Kuwahara, in *Advanced Fabrication Technologies for Micro/Nano Optics and Photonics II, Proceedings Volume 7205* (Eds.: T. J. Suleski, W. V. Schoenfeld, J. J. Wang), SPIE, San Jose, CA, **2009**, p. 720506.
[356] K. Watanabe, T. Hoshino, K. Kanda, Y. Haruyama, S. Matsui, *Jpn. J. Appl. Phys.* **2005**, *44*, L48.
[357] H. Butt, A. K. Yetisen, D. Mistry, S. A. Khan, M. U. Hassan, S. H. Yun, *Adv. Opt. Mater.* **2016**, *4*, 497.
[358] M. D. Ryan, R. M. Pearson, T. R. Tuladhar, A. Hess, L. Whitson, US20220259447A1 **2022**.
[359] O. Poncelet, G. Tallier, P. Simonis, A. Cornet, L. A. Francis, *Bioinspir. Biomim.* **2015**, *10*, 026004.
[360] R. Dewan, M. Marinkovic, R. Noriega, S. Phadke, A. Salleo, D. Knipp, *Opt. Express* **2009**, *17*, 23058.
[361] K. Aydin, V. E. Ferry, R. M. Briggs, H. A. Atwater, *Nat. Commun.* **2011**, *2*, 517.
[362] Z. Huang, X. Shi, G. Wang, P. Leukkunen, M. Huttula, W. Cao, *Sol. Energy* **2020**, *204*, 738.
[363] J. Huang, X. Wang, Z. L. Wang, *Nano Lett.* **2006**, *6*, 2325.
[364] B. Dai, L. Zhang, C. Zhao, H. Bachman, R. Becker, J. Mai, Z. Jiao, W. Li, L. Zheng, X. Wan, T. J. Huang, S. Zhuang, D. Zhang, *Nat. Commun.* **2021**, *12*, 6458.
[365] S. Dou, H. Xu, J. Zhao, K. Zhang, N. Li, Y. Lin, L. Pan, Y. Li, *Adv. Mater.* **2021**, *33*, 2000697.
[366] Z. Han, Z. Jiao, S. Niu, L. Ren, *Prog. Mater. Sci.* **2019**, *103*, 1.
[367] V. Singh, S. K. Chakarvarti, *Am. J. Bioeng. Biotechnol.* **2016**.
[368] W. Zhang, J. Gu, Q. Liu, H. Su, T. Fan, D. Zhang, *Phys. Chem. Chem. Phys.* **2014**, *16*, 19767.
[369] Z. Han, Z. Wang, B. Li, X. Feng, Z. Jiao, J. Zhang, J. Zhao, S. Niu, L. Ren, *ACS Appl. Mater. Interfaces* **2019**, *11*, 17019.
[370] R. A. Potyrailo, H. Ghiradella, A. Vertiatchikh, K. Dovidenko, J. R. Cournoyer, E. Olson, *Nat. Photonics* **2007**, *1*, 123.
[371] K. H. Sandhage, M. B. Dickerson, P. M. Huseman, M. A. Caranna, J. D. Clifton, T. A. Bull, T. J. Heibel, W. R. Overton, M. E. A. Schoenwaelder, *Adv. Mater.* **2002**, *14*, 429.
[372] S. B. Juhl, E. P. Chan, Y.-H. Ha, M. Maldovan, J. Brunton, V. Ward, T. Dokland, J. Kalmakoff, B. Farmer, E. L. Thomas, R. A. Vaia, *Adv. Funct. Mater.* **2006**, *16*, 1086.
[373] N. N. Shi, C.-C. Tsai, F. Camino, G. D. Bernard, N. Yu, R. Wehner, *Science* **2015**, *349*, 298.
[374] X. Ling, M. I. Osotsi, W. Zhang, Y. Wu, Q. Jin, D. Zhang, *J. Bionic Eng.* **2023**, *20*, 873.
[375] Y. Cui, H. Gong, Y. Wang, D. Li, H. Bai, *Adv. Mater.* **2018**, *30*, 1706807.
[376] H. Zhang, K. C. S. Ly, X. Liu, Z. Chen, M. Yan, Z. Wu, X. Wang, Y. Zheng, H. Zhou, T. Fan, *Proc. Natl. Acad. Sci. USA* **2020**, *117*, 14657.
[377] S. Fan, *Joule* **2017**, *1*, 264.
[378] Q. Zhang, S. Wang, X. Wang, Y. Jiang, J. Li, W. Xu, B. Zhu, J. Zhu, *Small Methods* **2022**, *6*, 2101379.
[379] S. An, B. Shi, M. Jiang, B. Fu, C. Song, P. Tao, W. Shang, T. Deng, *Chem. Rev.* **2023**, *123*, 7081.
[380] M. Wu, Z. Shao, N. Zhao, R. Zhang, G. Yuan, L. Tian, Z. Zhang, W. Gao, H. Bai, *Science* **2023**, *382*, 1379.
[381] S. Metwally, **n.d**.
[382] A. August, A. Kneer, A. Reiter, M. Wirtz, J. Sarsour, T. Stegmaier, S. Barbe, G. T. Gresser, B. Nestler, *Energy* **2019**, *168*, 1017.
[383] X. Yue, M. He, T. Zhang, D. Yang, F. Qiu, *ACS Appl. Mater. Interfaces* **2020**, *12*, 12285.
[384] R. Wehner, A. C. Marsh, S. Wehner, *Nature* **1992**, *357*, 586.
[385] C. Lou, S. An, R. Yang, H. Zhu, Q. Shen, M. Jiang, B. Fu, P. Tao, C. Song, T. Deng, W. Shang, *APL Photonics* **2021**, *6*, 036101.
[386] J. McPhetres, *Biol. Open* **2024**, *13*, bio060205.
[387] M. A. Hasan, S. Rashmi, A. C. M. Esther, P. Y. Bhavanisankar, B. N. Sherikar, N. Sridhara, A. Dey, *J. Mater. Eng. Perform.* **2018**, *27*, 1265.
[388] J. Teyssier, S. V. Saenko, D. Van Der Marel, M. C. Milinkovitch, *Nat. Commun.* **2015**, *6*, 6368.
[389] M. Li, X. Dai, W. Gao, H. Bai, *Acc. Mater. Res.* **2022**, *3*, 1173.
[390] S. E. Naleway, M. M. Porter, J. McKittrick, M. A. Meyers, *Adv. Mater.* **2015**, *27*, 5455.
[391] C. Chen, X. Zhao, Y. Chen, X. Wang, Z. Chen, H. Li, K. Wang, X. Zheng, H. Liu, *Adv. Funct. Mater.* **2021**, *31*, 2104784.
[392] M. C. Vu, P. J. Park, S.-R. Bae, S. Y. Kim, Y.-M. Kang, W. K. Choi, M. A. Islam, J. C. Won, M. Park, S.-R. Kim, *J. Mater. Chem. A* **2021**, *9*, 8527.
[393] Z. Qin, H. Sun, Y. Tang, S. Yin, L. Yang, M. Xu, Z. Liu, *ACS Appl. Mater. Interfaces* **2021**, *13*, 19467.
[394] X. Zhang, W. Hai, J. Pan, Y. Zhang, X. Chen, Z. Li, W. Huang, J. Jiang, S. Bi, H. Shao, N. Chen, G. Shao, *Appl. Mater. Today* **2025**, *43*, 102663.
[395] W. Wu, S. Lin, M. Wei, J. Huang, H. Xu, Y. Lu, W. Song, *Sol. Energy Mater. Sol. Cells* **2020**, *210*, 110512.
[396] E. M. Leung, M. C. Escobar, G. T. Stiubianu, S. R. Jim, A. L. Vyatskikh, Z. Feng, N. Garner, P. Patel, K. L. Naughton, M. Follador, E. Karshalev, M. D. Trexler, A. A. Gorodetsky, *Nat. Commun.* **2019**, *10*, 1947.
[397] M. A. Badshah, E. M. Leung, P. Liu, A. A. Strzelecka, A. A. Gorodetsky, *Nat. Sustain.* **2022**, *5*, 434.
[398] T. J. Wardill, P. T. Gonzalez-Bellido, R. J. Crook, R. T. Hanlon, *Proc. R. Soc. B Biol. Sci.* **2012**, *279*, 4243.
[399] M. Izumi, A. M. Sweeney, D. DeMartini, J. C. Weaver, M. L. Powers, A. Tao, T. V. Silvas, R. M. Kramer, W. J. Crookes-Goodson, L. M. Mäthger, R. R. Naik, R. T. Hanlon, D. E. Morse, *J. R. Soc. Interface* **2009**, *7*, 549.
[400] G. Hancke, B. Silva, G. Hancke, Jr., *Sensors* **2012**, *13*, 393.
[401] A. Chen, S. Chatterjee, *Chem. Soc. Rev.* **2013**, *42*, 5425.
[402] Y. H. Jung, B. Park, J. U. Kim, T. Kim, *Adv. Mater.* **2019**, *31*, 1803637.

[403] F. G. Barth, J. A. C. Humphrey, (Eds.: T. W. Secomb), *Sensors and Sensing in Biology and Engineering*, Springer, Wien, New York, **2003**.
[404] J. Zhang, W. B. Walker, G. Wang, in *Progress in Molecular Biology and Translational Science*, Elsevier, Cham **2015**, pp. 109-128.
[405] V. Richter, A. Rist, G. Kislinger, M. Laumann, A. Schoofs, A. Miroschnikow, M. Pankratz, A. Cardona, A. S. Thum, *eLife* **2025**, *12*, RP91155.
[406] K. Takei, Z. Yu, M. Zheng, H. Ota, T. Takahashi, A. Javey, *Proc. Natl. Acad. Sci. USA* **2014**, *111*, 1703.
[407] V. R. Adineh, B. Liu, R. Rajan, W. Yan, J. Fu, *Acta Biomater.* **2015**, *21*, 132.
[408] V. Amoli, S. Y. Kim, J. S. Kim, H. Choi, J. Koo, D. H. Kim, *J. Mater. Chem. C* **2019**, *7*, 14816.
[409] Q. Kan, R. Rajan, J. Fu, G. Kang, W. Yan, *Mater. Res. Bull.* **2013**, *48*, 5026.
[410] H. Schmitz, A. Schmitz, H. Bleckmann, *Naturwissenschaften* **2000**, *87*, 542.
[411] E. O. Gracheva, S. N. Bagriantsev, *Curr. Opin. Neurobiol.* **2015**, *34*, 67.
[412] E. O. Gracheva, N. T. Ingolia, Y. M. Kelly, J. F. Cordero-Morales, G. Hollopeter, A. T. Chesler, E. E. Sánchez, J. C. Perez, J. S. Weissman, D. Julius, *Nature* **2010**, *464*, 1006.
[413] J. T. Kennis, M.-L. Groot, *Curr. Opin. Struct. Biol.* **2007**, *17*, 623.
[414] S.-H. Liu, C.-K. Hu, J.-L. Lu, X. Lu, C.-X. Lu, J. Yao, X.-C. Chen, L. Jiang, *ACS Nano* **2024**, *18*, 9053.
[415] L. Wang, Y. Zhang, Y. Chen, L. Jiang, *Adv. Funct. Mater.* **2024**, *34*, 2401411.
[416] A. S. Mildvan, *Proteins Struct. Funct. Genet.* **1997**, *29*, 401.
[417] M. Benhar, M. T. Forrester, J. S. Stamler, *Nat. Rev. Mol. Cell Biol.* **2009**, *10*, 721.
[418] K. Goodwin, C. Viboud, L. Simonsen, *Vaccine* **2006**, *24*, 1159.
[419] H. Cosenza, H. Köhler, *Proc. Natl. Acad. Sci. USA* **1972**, *69*, 2701.
[420] N. Post, D. Eddy, C. Huntley, M. C. I. Van Schalkwyk, M. Shrotri, D. Leeman, S. Rigby, S. V. Williams, W. H. Bermingham, P. Kellam, J. Maher, A. M. Shields, G. Amirthalingam, S. J. Peacock, S. A. Ismail, *PLoS One* **2020**, *15*, 0244126.
[421] E. S. Hodgson, J. Y. Lettvin, K. D. Roeder, *Science* **1955**, *122*, 417.
[422] R. J. Schepers, M. Ringkamp, *Neurosci. Biobehav. Rev.* **2010**, *34*, 177.
[423] D. D. McKemy, W. M. Neuhausser, D. Julius, *Nature* **2002**, *416*, 52.
[424] P. G. Gillespie, R. G. Walker, *Nature* **2001**, *413*, 194.
[425] P. S. Stayton, T. Shimoboji, C. Long, A. Chilkoti, G. Ghen, J. M. Harris, A. S. Hoffman, *Nature* **1995**, *378*, 472.
[426] N. Du, F. Ye, J. Sun, K. Liu, *ChemBioChem* **2022**, *23*, 202100416.
[427] G. Schreiber, A. E. Keating, *Curr. Opin. Struct. Biol.* **2011**, *21*, 50.
[428] J. Wess, *Pharmacol. Ther.* **1998**, *80*, 231.
[429] T. Kenakin, *J. Pharmacol. Exp. Ther.* **2011**, *336*, 296.
[430] D. K. Stone, *Am. J. Med.* **1998**, *105*, 244.
[431] D. M. Rosenbaum, S. G. F. Rasmussen, B. K. Kobilka, *Nature* **2009**, *459*, 356.
[432] B. Nilius, G. Owsianik, *Genome Biol.* **2011**, *12*, 218.
[433] L. M. Luttrell, *Mol. Biotechnol.* **2008**, *39*, 239.
[434] D. R. McMillan, K. M. Kayes-Wandover, J. A. Richardson, P. C. White, *J. Biol. Chem.* **2002**, *277*, 785.
[435] D. R. McMillan, P. C. White, in *Adhesion-GPCRs: Structure to Function* (Eds.: S. Yona, M. Stacey), Springer US, Boston, MA **2010**, pp. 76-86.
[436] P. E. Schavemaker, A. J. Boersma, B. Poolman, *Front. Mol. Biosci.* **2018**, *5*, 93.
[437] B. Lemos, *Mol. Biol. Evol.* **2005**, *22*, 1345.
[438] Y. Xu, H. Wang, R. Nussinov, B. Ma, *Proteomics* **2013**, *13*, 1339.
[439] W. S. Hlavacek, R. G. Posner, A. S. Perelson, *Biophys. J.* **1999**, *76*, 3031.
[440] Z. Yan, L. Guo, L. Hu, J. Wang, *Bioinformatics* **2013**, *29*, 1127.
[441] T. Tan, D. Frenkel, V. Gupta, M. W. Deem, *Phys. Stat. Mech. Its Appl.* **2005**, *350*, 52.
[442] A. Steinbrecht, *Novartis Found. Symp.* **2007**.
[443] D. Wang, J. Zhang, G. Ma, Y. Fang, L. Liu, J. Wang, T. Sun, C. Zhang, X. Meng, K. Wang, Z. Han, S. Niu, L. Ren, *ACS Nano* **2021**, *15*, 19629.
[444] L. Liu, S. Niu, J. Zhang, Z. Mu, J. Li, B. Li, X. Meng, C. Zhang, Y. Wang, T. Hou, Z. Han, S. Yang, L. Ren, *Adv. Mater.* **2022**, *34*, 2200823.
[445] M. Mizunami, F. Yokohari, M. Takahata, *Zoolog. Sci.* **2004**, *21*, 1141.
[446] K.-E. Kaissling, in *Biologically Inspired Signal Processing for Chemical Sensing* (Eds.: A. Gutiérrez, S. Marco), Springer Berlin Heidelberg, Berlin, Heidelberg, **2009**, pp. 45-52.
[447] R. A. Steinbrecht, B. A. Stankiewicz, *J. Insect Physiol.* **1999**, *45*, 785.
[448] T. A. Keil, C. Steiner, *Tissue Cell* **1991**, *23*, 821.
[449] R. A. Steinbrecht, W. Gnatzy, *Cell Tissue Res.* **1984**, *235*, 25.
[450] R. A. Steinbrecht, *Z. Für Morphol. Tiere* **1970**, *68*, 93.
[451] M. A. R. Koehl, *Chem. Senses* **2006**, *31*, 93.
[452] S. Kanaujia, K. E. Kaissling, *J. Insect Physiol.* **1985**, *31*, 71.
[453] K.-E. Kaissling, *Chem. Senses* **2001**, *26*, 125.
[454] T. Hunger, R. A. Steinbrecht, *Tissue Cell* **1998**, *30*, 14.
[455] B. H. Sandler, L. Nikonova, W. S. Leal, J. Clardy, *Chem. Biol.* **2000**, *7*, 143.
[456] W. S. Leal, *Annu. Rev. Entomol.* **2013**, *58*, 373.
[457] R. G. Vogt, L. M. Riddiford, *Nature* **1981**, *293*, 161.
[458] P. Pelosi, J.-J. Zhou, L. P. Ban, M. Calvello, *Cell. Mol. Life Sci.* **2006**, *63*, 1658.
[459] Y. Shiota, T. Sakurai, T. Daimon, H. Mitsuno, T. Fujii, S. Matsuyama, H. Sezutsu, Y. Ishikawa, R. Kanzaki, *Sci. Rep.* **2018**, *8*, 13529.
[460] R. Maida, M. Mameli, B. Müller, J. Krieger, R. A. Steinbrecht, *J. Neurocytol.* **2005**, *34*, 149.
[461] E. JACQUIN-JOLY, C. MERLIN, *J. Chem. Ecol.* **2004**, *30*, 2359.
[462] T. Sakurai, H. Mitsuno, S. S. Haupt, K. Uchino, F. Yokohari, T. Nishioka, I. Kobayashi, H. Sezutsu, T. Tamura, R. Kanzaki, *PLoS Genet.* **2011**, *7*, 1002115.
[463] T. Nakagawa, T. Sakurai, T. Nishioka, K. Touhara, *Science* **2005**, *307*, 1638.
[464] T. Ando, S. Sekine, S. Inagaki, K. Misaki, L. Badel, H. Moriya, M. M. Sami, Y. Itakura, T. Chihara, H. Kazama, S. Yonemura, S. Hayashi, *Curr. Biol.* **2019**, *29*, 1512.
[465] S. R. Shanbhag, B. Müller, R. A. Steinbrecht, *Int. J. Insect Morphol. Embryol.* **1999**, *28*, 377.
[466] W. van der Goes van Naters, J. R. Carlson, *Curr. Biol.* **2007**, *17*, 606.
[467] A. Couto, M. Alenius, B. J. Dickson, *Curr. Biol.* **2005**, *15*, 1535.
[468] E. A. Hallem, J. R. Carlson, *Trends Genet.* **2004**, *20*, 453.
[469] R. F. Stocker, *Cell Tissue Res.* **1994**, *275*, 3.
[470] R. A. Steinbrecht, *Int. J. Insect Morphol. Embryol.* **1997**, *26*, 229.
[471] X. Qiu, J. Liu, B. Zhou, X. Zhang, *Adv. Funct. Mater.* **2023**, *33*, 2300321.
[472] Z. Nie, J. W. Kwak, M. Han, J. A. Rogers, *Adv. Mater.* **2024**, *36*, 2205609.
[473] Q. Xin, J. Zhang, Z. Han, H. Zhao, T. Hou, Y. Liu, S. Niu, Q. Han, Z. Mu, B. Li, Z. Wang, L. Ren, *Adv. Mater. Technol.* **2023**, *8*, 2200756.
[474] P. Fratzl, F. G. Barth, *Nature* **2009**, *462*, 442.
[475] V. P. Hytönen, B. Wehrle-Haller, *Exp. Cell Res.* **2016**, *343*, 35.
[476] K. M. Gray, K. M. Stroka, *Semin. Cell Dev. Biol.* **2017**, *71*, 106.
[477] H. C. De Melo, *Planta* **2023**, *257*, 55.
[478] M. L. Demey, R. C. Mishra, D. Van Der Straeten, *Trends Plant Sci.* **2023**, *28*, 825.
[479] B. L. Boublil, C. A. Diebold, C. F. Moss, *Sensors* **2021**, *21*, 6375.
[480] Q. Wang, C. Fan, Y. Gui, L. Zhang, J. Zhang, L. Sun, K. Wang, Z. Han, *Adv. Mater. Technol.* **2021**, *6*, 2100352.
[481] S. Moro, F. Deflorian, G. Spalluto, G. Pastorin, B. Cacciari, S.-K. Kim, K. A. Jacobson, *Chem. Commun.* **2003**, 2949.
[482] C. Wilde, J. Mitgau, T. Schý, T. Schöneberg, I. Liebscher, *Am. J. Physiol.-Cell Physiol.* **2022**, *322*, C1047.
[483] V. Joshi, P. R. Strege, G. Farrugia, A. Beyder, *Am. J. Physiol.-Gastrointest. Liver Physiol.* **2021**, *320*, G897.

[484] C. D. Cox, N. Bavi, B. Martinac, *Cell Rep.* **2019**, *29*, 1.
[485] Y. Luo, M. J. Z. Hartmann, *PLoS One* **2023**, *18*, 0269210.
[486] W. Zhang, Y. Fan, in *Fibrous Proteins* (Ed.: S. Ling), Springer US, New York, NY, **2021**, pp. 41-53.
[487] S. Tonomura, S. Ebara, K. Bagdasarian, D. Uta, E. Ahissar, I. Meir, I. Lampl, D. Kuroda, T. Furuta, H. Furue, K. Kumamoto, *Proc. Jpn. Acad. Ser. B* **2015**, *91*, 560.
[488] T. Furuta, N. E. Bush, A. E.-T. Yang, S. Ebara, N. Miyazaki, K. Murata, D. Hirai, K. Shibata, M. J. Z. Hartmann, *Curr. Biol.* **2020**, *30*, 815.
[489] A. K. Schulz, L. V. Kaufmann, L. T. Smith, D. S. Philip, H. David, J. Lazovic, M. Brecht, G. Richter, K. J. Kuchenbecker, *Cornell University* **2025**.
[490] M.-A. Sayegh, H. Daraghma, S. Mekid, S. Bashmal, *Sensors* **2022**, *22*, 2705.
[491] F. G. Barth, in *Comparative Hearing: Insects* (Eds.: R. R. Hoy, A. N. Popper, R. R. Fay), Springer New York, New York, NY **1998**, pp. 228-278.
[492] M. Erko, O. Younes-Metzler, A. Rack, P. Zaslansky, S. L. Young, G. Milliron, M. Chyasnavichyus, F. G. Barth, P. Fratzl, V. Tsukruk, I. Zlotnikov, Y. Politi, *J. R. Soc. Interface* **2015**, *12*, 20141111.
[493] R. Wang, Y. Sun, F. Zhang, M. Song, D. Tian, H. Li, *Angew. Chem., Int. Ed.* **2017**, *56*, 5294.
[494] K. Talavera, B. Nilius, T. Voets, *Trends Neurosci.* **2008**, *31*, 287.
[495] H. Wen, W. Zheng, *Biophys. J.* **2018**, *114*, 40.
[496] G. Fernández-Ballester, A. Fernández-Carvajal, A. Ferrer-Montiel, *Int. J. Mol. Sci.* **2023**, *24*, 743.
[497] D. Tran, H. Petitjean, Y. Chebli, A. Geitmann, R. Sharif-Naeini, *Plant Physiol.* **2021**, *187*, 1704.
[498] B. Martinac, M. Buechner, A. H. Delcour, J. Adler, C. Kung, *Proc. Natl. Acad. Sci. USA* **1987**, *84*, 2297.
[499] J. Jasti, H. Furukawa, E. B. Gonzales, E. Gouaux, *Nature* **2007**, *449*, 316.
[500] R. Li, X. Fan, Z. Liu, J. Zhai, *Adv. Mater.* **2017**, *29*, 1702983.
[501] C. Zhao, H. Wang, H. Zhang, *Mater. Chem. Front.* **2021**, *5*, 4059.
[502] A. Schmitz, A. Sehrbrock, H. Schmitz, *Arthropod Struct. Dev.* **2007**, *36*, 291.
[503] H. Schmitz, H. Bleckmann, M. Mürtz, *Nature* **1997**, *386*, 773.
[504] J. Yao, Y. Yao, T. Liu, *Mater. Des.* **2023**, *230*, 111968.
[505] H. Schmitz, H. Bleckmann, *J. Comp. Physiol.* **1998**, *182*, 647.
[506] D. Klocke, A. Schmitz, H. Soltner, H. Bousack, H. Schmitz, *Beilstein J. Nanotechnol.* **2011**, *2*, 186.
[507] R. Blakemore, *Science* **1975**, *190*, 377.
[508] A. Arakaki, H. Nakazawa, M. Nemoto, T. Mori, T. Matsunaga, *J. R. Soc. Interface* **2008**, *5*, 977.
[509] M. Marmol, E. Gachon, D. Faivre, *Rev. Mod. Phys.* **2024**, *96*, 021001.
[510] A. Arakaki, A. Yamagishi, A. Fukuyo, M. Tanaka, T. Matsunaga, *Mol. Microbiol.* **2014**, *93*, 554.
[511] S. M. Bird, A. E. Rawlings, J. M. Galloway, S. S. Staniland, *RSC Adv.* **2016**, *6*, 7356.
[512] S. M. Bird, A. E. Rawlings, J. M. Galloway, S. S. Staniland, *RSC Advances* **2016**, *6*, 7356.
[513] A. Arakaki, M. Goto, M. Maruyama, T. Yoda, M. Tanaka, A. Yamagishi, Y. Yoshikuni, T. Matsunaga, *Biotechnol. J.* **2020**, *15*, 2000278.
[514] R. J. Wilfinger, P. H. Bardell, D. S. Chhabra, *IBM J. Res. Dev.* **1968**, *12*, 113.
[515] H. P. Lang, in *Solid State Gas Sensors* (Eds.: E. Comini, G. Faglia, G. Sberveglieri), Springer US, Boston, MA **2009**, p. 1-24.
[516] E. S. Kolesar, **n.d**.
[517] G. Binnig, C. F. Quate, C.h. Gerber, *Phys. Rev. Lett.* **1986**, *56*, 930.
[518] D. Spitzer, T. Cottineau, N. Piazzon, S. Josset, F. Schnell, S. N. Pronkin, E. R. Savinova, V. Keller, *Angew. Chem., Int. Ed.* **2012**, *51*, 5334.
[519] V. Zwilling, M. Aucouturier, E. Darque-Ceretti, *Electrochim. Acta* **1999**, *45*, 921.
[520] H. Aldahhak, P. Powroźnik, P. Pander, W. Jakubik, F. B. Dias, W. G. Schmidt, U. Gerstmann, M. Krzywiecki, *J. Phys. Chem. C* **2020**, *124*, 6090.
[521] K. Zboray, A. V. Toth, T. D. Miskolczi, K. Pesti, E. Casanova, E. Kreidl, A. Mike, Á. Szenes, L. Sági, P. Lukacs, *Sci. Rep.* **2023**, *13*, 21757.
[522] R. Wasserkort, T. Koller, *J. Appl. Toxicol.* **1997**, *17*, 119.
[523] J. Shim, A. Sen, K. Park, H. Park, A. Bala, H. Choi, M. Park, J. Y. Kwon, S. Kim, *ACS Nano* **2023**, *17*, 21719.
[524] O. Leitch, C. Lennard, K. Paul Kirkbride, A. Anderson, *Anal. Bioanal. Chem.* **2018**, *410*, 7739.
[525] L. B. Vosshall, *Curr. Opin. Neurobiol.* **2000**, *10*, 498.
[526] J. An, P. Chen, Z. Wang, A. Berbille, H. Pang, Y. Jiang, T. Jiang, Z. L. Wang, *Adv. Mater.* **2021**, *33*, 2101891.
[527] C. Zhang, M. Wu, M. Li, L. Che, Z. Tan, D. Guo, Z. Kang, S. Cao, S. Zhang, Y. Sui, J. Sun, L. Wang, J. Liu, *Microsyst. Nanoeng.* **2023**, *9*, 87.
[528] C. Wang, J. Zhao, C. Ma, J. Sun, L. Tian, X. Li, F. Li, X. Han, C. Liu, C. Shen, L. Dong, J. Yang, C. Pan, *Nano Energy* **2017**, *34*, 578.
[529] T. Yang, X. Li, X. Jiang, S. Lin, J. Lao, J. Shi, Z. Zhen, Z. Li, H. Zhu, *Mater. Horiz.* **2016**, *3*, 248.
[530] I. Fernández-Cuevas, J. C. Bouzas Marins, J. Arnáiz Lastras, P. M. Gómez Carmona, S. Piñonosa Cano, M. Á. García-Concepción, M. Sillero-Quintana, *Infrared Phys. Technol.* **2015**, *71*, 28.
[531] R. Usamentiaga, P. Venegas, J. Guerediaga, L. Vega, J. Molleda, F. Bulnes, *Sensors* **2014**, *14*, 12305.
[532] B. Stefanov, A. P. Teixeira, M. Mansouri, A. Bertschi, K. Krawczyk, G. C. Hamri, S. Xue, M. Fussenegger, *Adv. Sci.* **2021**, *8*, 2101813.
[533] B. Yameen, M. Ali, R. Neumann, W. Ensinger, W. Knoll, O. Azzaroni, *Small* **2009**, *5*, 1287.
[534] M. Liu, H. Zhang, K. Li, L. Heng, S. Wang, Y. Tian, L. Jiang, *Adv. Funct. Mater.* **2015**, *25*, 421.
[535] Y. Shang, Y. Zhang, P. Li, J. Lai, X.-Y. Kong, W. Liu, K. Xiao, G. Xie, Y. Tian, L. Wen, L. Jiang, *Chem. Commun.* **2015**, *51*, 5979.
[536] H. Zhang, X. Hou, L. Zeng, F. Yang, L. Li, D. Yan, Y. Tian, L. Jiang, *J. Am. Chem. Soc.* **2013**, *135*, 16102.
[537] X. Hou, W. Guo, L. Jiang, *Chem. Soc. Rev.* **2011**, *40*, 2385.
[538] C. Wang, D. Wang, W. Miao, L. Shi, S. Wang, Y. Tian, L. Jiang, *ACS Nano* **2020**, *14*, 12614.
[539] M. Trivedi, N. Nirmalkar, *Sci. Rep.* **2022**, *12*, 2547.
[540] W. Guo, H. Xia, F. Xia, X. Hou, L. Cao, L. Wang, J. Xue, G. Zhang, Y. Song, D. Zhu, Y. Wang, L. Jiang, *ChemPhysChem* **2010**, *11*, 859.
[541] Y. Wu, G. Yang, M. Lin, X. Kong, L. Mi, S. Liu, G. Chen, Y. Tian, L. Jiang, *Angew. Chem.* **2019**, *131*, 12611.
[542] C. Jiang, M. E. McConney, S. Singamaneni, E. Merrick, Y. Chen, J. Zhao, L. Zhang, V. V. Tsukruk, *Chem. Mater.* **2006**, *18*, 2632.
[543] R. Bogue, *Sens. Rev.* **2007**, *27*, 278.
[544] C. Jiang, S. Markutsya, Y. Pikus, V. V. Tsukruk, *Nat. Mater.* **2004**, *3*, 721.
[545] C. E. Killian, F. H. Wilt, *Chem. Rev.* **2008**, *108*, 4463.
[546] M. Suzuki, H. Nagasawa, *Can. J. Zool.* **2013**, *91*, 349.
[547] T. Mass, A. J. Giuffre, C.-Y. Sun, C. A. Stifler, M. J. Frazier, M. Neder, N. Tamura, C. V. Stan, M. A. Marcus, P. U. P. A. Gilbert, *Proc. Natl. Acad. Sci. USA* **2017**, *114*, E7670.
[548] G. Luquet, *ZooKeys* **2012**, *176*, 103.
[549] R. S. Keir, *Geochim. Cosmochim. Acta* **1980**, *44*, 241.
[550] E. Marañón, W. M. Balch, P. Cermeño, N. González, C. Sobrino, A. Fernández, M. Huete-Ortega, D. C. López-Sandoval, M. Delgado, M. Estrada, M. Álvarez, E. Fernández-Guallart, C. Pelejero, *Limnol. Oceanogr.* **2016**, *61*, 1345.
[551] T. Wu, Y. Yang, Y. Cao, Y. Song, L.-P. Xu, X. Zhang, S. Wang, *ACS Appl. Mater. Interfaces* **2018**, *10*, 42050.

[552] J. Roca-Martinez, T. Lazar, J. Gavalda-Garcia, D. Bickel, R. Pancsa, B. Dixit, K. Tzavella, P. Ramasamy, M. Sanchez-Fornaris, I. Grau, W. F. Vranken, *Front. Mol. Biosci.* **2022**, *9*, 959956.
[553] L. Restrepo-Pérez, C. Joo, C. Dekker, *Nat. Nanotechnol.* **2018**, *13*, 786.
[554] K. A. Brown, J. A. Melby, D. S. Roberts, Y. Ge, *Expert Rev. Proteomics* **2020**, *17*, 719.
[555] H. Cölfen, in *Methods in Enzymology*, Elsevier, Cham **2013**, pp. 277-304.
[556] W. Chen, J. Meng, S. Wang, *ACS Nano* **2025**, *19*, 7546.
[557] W. Hou, L. Lancaster, D. Li, A. Bowlus, K. Bozhilov, D. Kisailus, *Bioinspired Biomim. Nanobiomater.* **2014**, *3*, 10.
[558] J. Aizenberg, *Adv. Mater.* **2004**, *16*, 1295.
[559] J. A. Liddle, G. M. Gallatin, *ACS Nano* **2016**, *10*, 2995.
[560] A. Santos, M. J. Deen, L. F. Marsal, *Nanotechnology* **2015**, *26*, 042001.
[561] C. A. Charitidis, P. Georgiou, M. A. Koklioti, A.-F. Trompeta, V. Markakis, *Manuf. Rev. 2014 1*, 11.
[562] S. M. Stavis, J. A. Fagan, M. Stopa, J. A. Liddle, A. C. S. Appl, *Nano Mater* **2018**, *1*, 4358.
[563] Srinivas Institute of Management Studies, P. S. Aithal, S. Aithal, *Int. J. Eng. Manuf.* **2016**, *6*, 15.
[564] M. Mabrouk, D. B. Das, Z. A. Salem, H. H. Beherei, *Molecules* **2021**, *26*, 1077.
[565] N. Baig, I. Kammakakam, W. Falath, *Mater. Adv* **2021**, *2*, 1821.
[566] V. Sebastian, M. Arruebo, *J. Santamaria, Small* **2014**, *10*, 835.
[567] D. R. Baer, M. H. Engelhard, G. E. Johnson, J. Laskin, J. Lai, K. Mueller, P. Munusamy, S. Thevuthasan, H. Wang, N. Washton, A. Elder, B. L. Baisch, A. Karakoti, S. V. N. T. Kuchibhatla, D. Moon, *J. Vac. Sci. Technol. Vac. Surf. Films* **2013**, *31*, 50820.
[568] Y. Pan, W. J. Paschoalino, A. Szuchmacher Blum, J. Mauzeroll, *ChemSusChem* **2021**, *14*, 758.
[569] J. Huang, L. Lin, D. Sun, H. Chen, D. Yang, Q. Li, *Chem. Soc. Rev.* **2015**, *44*, 6330.
[570] O. Berger, C. Battistella, Y. Chen, J. Oktawiec, Z. E. Siwicka, D. Tullman-Ercek, M. Wang, N. C. Gianneschi, *J. Am. Chem. Soc.* **2022**, *144*, 4383.
[571] S. Binauld, D. Damiron, L. A. Connal, C. J. Hawker, E. Drockenmuller, *Macromol. Rapid Commun.* **2011**, *32*, 147.
[572] Y. Jiang, M. R. Golder, H. V.-T. Nguyen, Y. Wang, M. Zhong, J. C. Barnes, D. J. C. Ehrlich, J. A. Johnson, *J. Am. Chem. Soc.* **2016**, *138*, 9369.
[573] A. J. DeStefano, R. A. Segalman, E. C. Davidson, *JACS Au* **2021**, *1*, 1556.
[574] M. Zhang, Y. Chen, C. Wu, R. Zheng, Y. Xia, E. G. Saccuzzo, T. K. H. Trinh, E. A. Q. Mondarte, E. Nakouzi, B. Rad, B. A. Legg, W. J. Shaw, J. Tao, J. J. De Yoreo, C.-L. Chen, *Proc. Natl. Acad. Sci. USA* **2024**, *121*, 2412358121.
[575] W. S. Horne, T. N. Grossmann, *Nat. Chem.* **2020**, *12*, 331.
[576] W. Yang, Q. Yin, C.-L. Chen, *Chem. Mater.* **2021**, *33*, 3047.
[577] C.-L. Chen, J. Qi, R. N. Zuckermann, J. J. DeYoreo, *J. Am. Chem. Soc.* **2011**, *133*, 5214.
[578] J.-F. Lutz, M. Ouchi, D. R. Liu, M. Sawamoto, *Science* **2013**, *341*, 1238149.
[579] J. Jumper, R. Evans, A. Pritzel, T. Green, M. Figurnov, O. Ronneberger, K. Tunyasuvunakool, R. Bates, A. Žídek, A. Potapenko, A. Bridgland, C. Meyer, S. A. A. Kohl, A. J. Ballard, A. Cowie, B. Romera-Paredes, S. Nikolov, R. Jain, J. Adler, T. Back, S. Petersen, D. Reiman, E. Clancy, M. Zielinski, M. Steinegger, M. Pacholska, T. Berghammer, S. Bodenstein, D. Silver, O. Vinyals, et al., *Nature* **2021**, *596*, 583.
[580] J. Lu, M. Luo, B. I. Yakobson, *Carbon* **2018**, *128*, 231.
[581] H. Heinz, T.-J. Lin, R. Kishore Mishra, F. S. Emami, *Langmuir* **2013**, *29*, 1754.
[582] M. Praprotnik, L. D. Site, K. Kremer, *Annu. Rev. Phys. Chem.* **2008**, *59*, 545.
[583] K. Torkelson, N. Y. Naser, X. Qi, Z. Li, W. Yang, K. Pushpavanam, C.-L. Chen, F. Baneyx, J. Pfaendtner, *Chem. Mater.* **2024**, *36*, 786.
[584] F. M. Paulussen, G. K. Schouten, C. Moertl, J. Verheul, I. Hoekstra, G. M. Koningstein, G. H. Hutchins, A. Alkir, R. A. Luirink, D. P. Geerke, P. Van Ulsen, T. Den Blaauwen, J. Luirink, T. N. Grossmann, *J. Am. Chem. Soc.* **2022**, *144*, 15303.
[585] N. K. Hansoge, T. Huang, R. Sinko, W. Xia, W. Chen, S. Keten, *ACS Nano* **2018**, *12*, 7946.
[586] A. Gooneie, S. Schuschnigg, C. Holzer, *Polymers* **2017**, *9*, 16.
[587] Y. D. Ha, F. Bobaru, *Int. J. Fract.* **2010**, *162*, 229.
[588] B. Wang, S. Oterkus, E. Oterkus, *Contin. Mech. Thermodyn.* **2023**, *35*, 705.
[589] N. Guarín-Zapata, J. Gómez, D. Kisailus, P. D. Zavattieri, *J. Mech. Phys. Solids* **2019**, *131*, 344.
[590] G. X. Gu, C.-T. Chen, D. J. Richmond, M. J. Buehler, *Mater. Horiz* **2018**, *5*, 939.
[591] G. X. Gu, C.-T. Chen, M. J. Buehler, *Extreme Mech. Lett.* **2018**, *18*, 19.
[592] M. Nayak, A. S. S. Narayana, In *Edge Intell.*, Wiley, Hoboken, NJ, **2025**, pp. 307–325.
[593] M. Yang, N. A. Kotov, *Nat. Rev. Mater.* **2024**, *10*, 382.
[594] M. Cha, E. S. T. Emre, X. Xiao, J.-Y. Kim, P. Bogdan, J. S. VanEpps, A. Violi, N. A. Kotov, *Nat. Comput. Sci.* **2022**, *2*, 243.
[595] T. Deckert-Gaudig, E. Kämmer, V. Deckert, *J. Biophotonics* **2012**, *5*, 215.
[596] S. Bonhommeau, S. Lecomte, *ChemPhysChem* **2018**, *19*, 8.
[597] A. Calderaro, C. Chezzi, *Microorganisms* **2024**, *12*, 322.
[598] C. Dixit, K. Lata Dixit, C. Kumar Dixit, P. K. Pandey, S. A. Siddiqui, *Int. J. Mod. Achiev. Sci. Eng. Technol.* **2024**, *2*, 36.
[599] R. Fernandez-Leiro, S. H. W. Scheres, *Nature* **2016**, *537*, 339.
[600] In *Handb. Mater. Charact.*, Springer International Publishing, Cham, **2018**, pp. 113.
[601] A. Rao, M. Schoenenberger, E. Gnecco, T. Glatzel, E. Meyer, D. Brändlin, L. Scandella, *J. Phys. Conf. Ser.* **2007**, *61*, 971.
[602] J. Mast, E. Verleysen, V.-D. Hodoroaba, R. Kaegi, In *Charact. Nanoparticles*, Elsevier, Amsterdam, Netherlands, **2020**, pp. 29–48.
[603] Z. Lyu, L. Yao, W. Chen, F. C. Kalutantirige, Q. Chen, *Chem. Rev.* **2023**, *123*, 4051.
[604] A. Dazzi, C. B. Prater, *Chem. Rev.* **2017**, *117*, 5146.
[605] P. Verma, *Chem. Rev.* **2017**, *117*, 6447.
[606] B. R. Neugirg, S. R. Koebley, H. C. Schniepp, A. Fery, *Nanoscale* **2016**, *8*, 8414.
[607] J. Mathurin, A. Deniset-Besseau, D. Bazin, E. Dartois, M. Wagner, A. Dazzi, *J. Appl. Phys.* **2022**, *131*, 010901.
[608] L. Wang, H. Wang, X. G. Xu, *Chem. Soc. Rev.* **2022**, *51*, 5268.
[609] J. Xu, X. Zhu, S. Tan, Y. Zhang, B. Li, Y. Tian, H. Shan, X. Cui, A. Zhao, Z. Dong, J. Yang, Y. Luo, B. Wang, J. G. Hou, *Science* **2021**, *371*, 818.
[610] N. M. Larson, J. Mueller, A. Chortos, Z. S. Davidson, D. R. Clarke, J. A. Lewis, *Nature* **2023**, *613*, 682.
[611] R. L. Truby, J. A. Lewis, *Nature* **2016**, *540*, 371.
[612] J. A. Lewis, J. E. Smay, J. Stuecker, J. Cesarano, *J. Am. Ceram. Soc.* **2006**, *89*, 3599.
[613] A. Velasco-Hogan, J. Xu, M. A. Meyers, *Adv. Mater.* **2018**, *30*, 1800940.
[614] J. Bauer, A. Guell Izard, Y. Zhang, T. Baldacchini, L. Valdevit, *Adv. Mater. Technol.* **2019**, *4*, 1900146.
[615] J. Ye, X. Zhou, Z. Huang, X. Zhang, W. Huang, B. Wu, H. Zhou, *Int. J. Extreme Manuf.* **2025**, *7*, 022011.
[616] C. Tan, R. Li, J. Su, D. Du, Y. Du, B. Attard, Y. Chew, H. Zhang, E. J. Lavernia, Y. Fautrelle, J. Teng, A. Dong, *Int. J. Mach. Tools Manuf.* **2023**, *189*, 104032.
[617] P. Niksiar, F. Y. Su, M. B. Frank, T. A. Ogden, S. E. Naleway, M. A. Meyers, J. McKittrick, M. M. Porter, *Ceramics* **2019**, *2*, 208.

[618] W. Liu, S. Shen, J. Meng, J. Xiao, H. Li, H. Du, Q. Yin, C. Tan, *Int. J. Extreme Manuf.* **2025**, *7*, 045008.
[619] N. J. W. Penfold, J. Yeow, C. Boyer, S. P. Armes, *ACS Macro Lett.* **2019**, *8*, 1029.
[620] C. E. Boott, J. Gwyther, R. L. Harniman, D. W. Hayward, I. Manners, *Nat. Chem.* **2017**, *9*, 785.
[621] C. Luo, A. K. K. Kyaw, L. A. Perez, S. Patel, M. Wang, B. Grimm, G. C. Bazan, E. J. Kramer, A. J. Heeger, *Nano Lett.* **2014**, *14*, 2764.
[622] P. F. W. Simon, R. Ulrich, H. W. Spiess, U. Wiesner, *Chem. Mater.* **2001**, *13*, 3464.
[623] H.-A. Klok, S. Lecommandoux, *Adv. Mater.* **2001**, *13*, 1217.
[624] N. A. Lynd, A. J. Meuler, M. A. Hillmyer, *Prog. Polym. Sci.* **2008**, *33*, 875.
[625] J. K. Kim, S. Y. Yang, Y. Lee, Y. Kim, *Prog. Polym. Sci.* **2010**, *35*, 1325.
[626] Y. Mai, A. Eisenberg, *Chem. Soc. Rev.* **2012**, *41*, 5969.
[627] J. G. Werner, Y. Li, U. Wiesner, *Small Sci.* **2023**, *3*, 2300074.
[628] L. Xu, Y. Li, T. Cai, J. Zhang, L. He, R. Cai, C. Zhu, H. Shi, Z. Chu, X. Shen, *Macromol. Res.* **2024**, *32*, 453.
[629] M. Stefik, S. Guldin, S. Vignolini, U. Wiesner, U. Steiner, *Chem. Soc. Rev.* **2015**, *44*, 5076.
[630] K. Kuperkar, D. Patel, L. I. Atanase, P. Bahadur, *Polymers* **2022**, *14*, 4702.
[631] N. Yan, X. Liu, J. Zhu, Y. Zhu, W. Jiang, *ACS Nano* **2019**, *13*, 6638.
[632] A. N. Sokolov, F. L. Yap, N. Liu, K. Kim, L. Ci, O. B. Johnson, H. Wang, M. Vosgueritchian, A. L. Koh, J. Chen, J. Park, Z. Bao, *Nat. Commun.* **2013**, *4*.
[633] Y. He, T. Ye, M. Su, C. Zhang, A. E. Ribbe, W. Jiang, C. Mao, *Nature* **2008**, *452*, 198.
[634] L. Nguyen, M. Döblinger, T. Liedl, A. Heuer-Jungemann, *Angew. Chem., Int. Ed.* **2019**, *58*, 912.
[635] K. A. Afonin, E. Bindewald, A. J. Yaghoubian, N. Voss, E. Jacovetty, B. A. Shapiro, L. Jaeger, *Nat. Nanotechnol.* **2010**, *5*, 676.
[636] K. E. Shopsowitz, Y. H. Roh, Z. J. Deng, S. W. Morton, P. T. Hammond, *Small* **2014**, *10*, 1623.
[637] N. P. King, W. Sheffler, M. R. Sawaya, B. S. Vollmar, J. P. Sumida, I. André, T. Gonen, T. O. Yeates, D. Baker, *Science* **2012**, *336*, 1171.
[638] Y. Hsia, J. B. Bale, S. Gonen, D. Shi, W. Sheffler, K. K. Fong, U. Nattermann, C. Xu, P.-S. Huang, R. Ravichandran, S. Yi, T. N. Davis, T. Gonen, N. P. King, D. Baker, *Nature* **2016**, *535*, 136.
[639] P.-Y. Chen, A. Y.-M. Lin, J. McKittrick, M. A. Meyers, *Acta Biomater.* **2008**, *4*, 587.
[640] N. Petrov, S. R. Pollack, *Biorheol. Off. J. Int. Soc. Biorheol.* **2003**, *40*, 347.
[641] T. Garland, C. J. Downs, A. R. Ives, *Physiol. Biochem. Zool.* **2022**, *95*, 82.
[642] Z. Jia, M. C. Fernandes, Z. Deng, T. Yang, Q. Zhang, A. Lethbridge, J. Yin, J.-H. Lee, L. Han, J. C. Weaver, K. Bertoldi, J. Aizenberg, M. Kolle, P. Vukusic, L. Li, *Proc. Natl. Acad. Sci. USA* **2021**, *118*, 2101017118.
[643] N. D. S. Araujo, R. Perez, Q. Willot, M. Defrance, S. Aron, *Ecol. Evol.* **2023**, *13*, 10438.
[644] H. Heatwole, S. Harrington, *J. Arid Environ.* **1989**, *16*, 69.

Chao Hsuan (Joseph) Sung obtained his Bachelor of materials science and engineering from the University of California, Irvine in 2022. He is currently a Ph.D. student at the University of California, Irvine working with Professor David Kisailus. His current research focuses on cyanobacteria-assisted metal extraction, mineral dissolution and recrystallization, as well as mesocrystalline assembly of iron oxides.

David Kisailus is a Professor in the Department of Materials Science and Engineering and Director of the Materials and Manufacturing Technologies Program at the University of California, Irvine. Professor Kisailus, a Kavli Fellow of the National Academy of Sciences and Member of UNESCO Chair in Materials and Technologies for Energy Conversion, Saving and Storage (MATECSS), received his Ph.D. in Materials Science from the University of California at Santa Barbara (2002), M.S. from the University of Florida in Materials Science and B.S. in Chemical Engineering from Drexel University. Prof. Kisailus was a post-doctoral researcher in the Institute for Collaborative Biotechnologies, University of California at Santa Barbara. Following this, he was a Research Scientist at HRL Laboratories and then joined as faculty at the University of California. Professor Kisailus is currently the PI of the Biomimetics and Nanostructured Materials Group which focuses on investigating synthesis-structure-property relationships in biological materials and their translation to bio-inspired materials, including developing solution-based processes to synthesize nanoscale materials for energy and environmental-based applications.